Design and Characterization of a Transceiver Telescope for Quantum Communications with Satellites

by

Kimia Mohammadi

A thesis
presented to the University of Waterloo
in fulfillment of the
thesis requirement for the degree of
Master of Science
in
Physics (Quantum Information)

Waterloo, Ontario, Canada, 2021

Author's Declaration

This thesis consists of material all of which I authored or co-authored: see Statement of Contributions included in the thesis. This is a true copy of the thesis, including any required final revisions, as accepted by my examiners.

I understand that my thesis may be made electronically available to the public.

Statement of Contributions

This thesis contains work done in collaboration with others but to which I made the major contribution. The contributions are listed below.

Chapter 1: Kimia Mohammadi wrote the Introduction chapter.

Chapter 2: Kimia Mohammadi conducted a literature review on atmospheric turbulence and calculated the parameters based on QEYSSat requirements.
Kimia Mohammadi performed the link analysis of an uplink to determine the telescope aperture size.

Chapter 3: Kimia Mohammadi designed the lens via Zemax software and determined its surface specifications.
Hyperion Optics assisted with refining the lens design and fabricated the lens.
Youn Seok Lee assisted with power throughput measurements. Kimia Mohammadi plotted and analysed the data.
Kimia Mohammadi simulates the configuration of the optical elements of the telescope via Zemax software.
Jean-Philippe Bourgoin and Katanya Kuntz developed MATLAB code to simulate a far-field beam in presence of atmospheric turbulence and it was modified by Kimia Mohammadi to model the impacts of the aberrations induced by the optical elements as well as the turbulence.

Chapter 4: Kimia Mohammadi designed the telescope via Solidworks software.
Harmen Vander Heide and Andrew Dube provided design consultations and manufactured the mechanical parts at University of Waterloo science machine shop.
The mechanical parts were anodized by Waterloo Electroplating and Metal Finishing Incorporation.
Kimia Mohammadi carried out the purchase of the commercial components.
Kimia Mohammadi and Youn Seok Lee assembled the telescope.

Chapter 5: **Star test:**Thomas Jennewein conceived the idea.
Kimia Mohammadi designed and implemented experimental apparatus.
Youn Seok Lee and Paul Godin helped with the measurements.
Kimia Mohammadi analysed the experimental data.

Wavefront measurement: The wavefront characterization setup was designed by Youn Seok Lee and Thomas Jennewein. Youn Seok Lee carried out the design analysis.
Kimia Mohammadi and Youn Seok Lee implemented the measurement apparatus.
Kimia Mohammadi developed the control software.
Youn Seok Lee and Kimia Mohammadi performed the test. Youn Seok Lee performed the wavefront reconstruction and error analysis.

Polarization characterization: Thomas Jennewein and Youn Seok Lee conceived the idea of polarization measurement setup.
Youn Seok Lee developed the measurement apparatus and its control software.
Lindsay Babcock and Youn Seok Lee performed the initial characterization of the developed system.
Kimia Mohammadi and Hugh Podmore prepared the test optics developed for quantum transmitter and satellite payload.
Youn Seok Lee and Kimia Mohammadi performed the polarization test on those opticalcomponents.
Kimia Mohammadi and Youn Seok Lee performed the analysis on the polarization error for the tilt polarimeter.
Youn Seok Lee analyzed the data.
Thomas Jennewein and Brendon Higgins supervised the project.

Chapter 6: Kimia Mohammadi wrote the Conclusion chapter.

Abstract

Since the feasibility of free-space Quantum Key Distribution (QKD) was realized, a new race has begun amongst researchers to achieve the highest secure key rate and the most efficient protocols to form quantum communication channels allowing the creation of a global quantum communication network. Since 1992, multiple demonstrations have been executed that resulted in the first quantum network with 4,600 km coverage using optical fibres and Micius quantum satellite in three Chinese cities. In Canada, the Quantum Encryption and Science Satellite (QEYSSat) mission works towards establishing ground-to-satellite quantum links and forming a secure communication network across the country.

This thesis investigates the design of a transceiver telescope capable of both transmitting and receiving quantum signals at 785 nm, with higher efficiency than similar commercial options. This telescope is aimed to be one of the quantum ground stations of the QEYSSat project, which establishes a ground-to-satellite link (uplink configuration), to perform QKD with polarization encoded photons. Commercial telescopes and lenses are either not designed or optimized for the specific wavelengths required for a free space quantum link, or are not available in the required size to minimize link loss for beam transmission to a satellite in Low-Earth-orbit (LEO). Thus, a refractive telescope was designed with a custom-designed 8-inch lens and two motorized folding mirrors to emit a quantum signal at 785 nm while tracking the beacon light of the satellite at either 980 nm or 1550 nm wavelengths.

Furthermore, the atmospheric turbulence formed by temperature gradients is the main reason for link attenuation in an uplink configuration. Turbulence is highly dependent on the altitude and weather conditions, which makes the prediction challenging. However, it is formulated such that it suggests the maximum length, in which the spatial phase of a travelling light can be saved. By considering the diffraction of the transmitted beam and estimating the turbulence strength we could obtain the lens diameter that has the least link loss in presence of atmospheric turbulence. The manufacturing aspects, like the capability of constructing large lenses and the related costs, were taken into consideration as the important factors in determining the optimal aperture size.

The telescope lens was designed specifically for the desired wavelengths, by selecting the optimal material, thickness and radius of curvature. Therefore, the Seidel aberrations that distort the transmitted wavefront were minimized as much as possible. Since the wavefront distorted by the imperfections of the optics or the atmospheric turbulence can be defined by Zernike polynomials, we developed a model to simulate both the lens and the atmosphere structure to predict the far-field beam detected by the satellite. These

analyses shed light on the lens specifications and accuracy needed in the manufacturing process, which reduced the costs.

Finally, our custom-designed telescope was characterized by applying tests such as polarization measurement to confirm its performance in maintaining the polarization of a transmitted beam at 785 nm. Moreover, the wavefront measurement results and the non-aberrated image of a point light source in a star test validated our optimizations in the lens design. Since the new ground station has passed the preliminary tests for establishing a free-space quantum channel with polarized photons we are looking forward to calibrating the telescope and developing our tracking systems for further QKD experiments, once the QEYSSat microsatellite is launched in near future.

Acknowledgements

My special gratitude goes out to Thomas Jennewein, my supervisor, who had faith in me to be a part of his big family at IQC. Accomplishing this degree could not be possible without his endless encouragement and support. I truly appreciate all the precious learning moments I had during our many insightful conversations. I would also want to thank my Advisory Committee members: Kevin Resch and Norbert Lutkenhaus for their guidance throughout my master's.

I would like to thank all the past and present members of Quantum Photonics Lab whose hard work and support have been inspiring since the first day I joined the group. I am grateful for the only one-term time I had to experience the joyful hours of teamwork in the lab just before the COVID-19 pandemic hit us. However, our online meetings and social events were nothing less than remarkable memories and "hopefully" once-in-a-lifetime experiences. My next thank you goes to Youn, who taught me the ABCs of working in a photonics lab while being patient with all my questions and blunders. I would also like to thank Ramy for his advice and help with this project, as well as, organizing social events that were the birth of many friendships. Also, I am thankful to Ramy and Wilson for proofreading this thesis.

I cherish the days and nights I spent with friends at IQC, to get an assignment done on time, or to enjoy a karaoke night. IQC has been my second home in the past few years, which brought me wonderful friends and was the launchpad for the flight towards my dreams. I am grateful to all Physics and IQC staff and faculties, that made this happen and helped me countless times along this journey.

Thank you to my friends who were tremendous support through this chapter of my life, regardless of where on the globe they were. Many thanks to my housemates, Kimiya, Noura and Donya who were listening ears to all my thoughts, goals and emotions. Finally, my heartfelt thanks go to my favourite people on the Earth: my parents, Rozita and Mehdi and my little brother, Kasra, who have always believed in me and have unconditionally supported me through all stages of my life. Words cannot express my appreciation for having all these amazing people, by my side, online or in-person, without whom achieving this degree could not be possible.

Dedication

This thesis is dedicated to my Mum and Dad, whose endless love and support has been with me in every second of my life, regardless of any geographical boundaries.

Table of Contents

List of Figures

List of Tables

Chapter 1

Introduction

1.1 Quantum Information

Quantum information has extended the frontiers of physics in the past few decades. Since the birth of quantum mechanics and the emergence of quantum information and quantum computers, numerous investigations sharpened our intuition about the mysterious world of quantum physics and push the horizons of our understanding of the current applications and technology. Quantum computers [41], quantum sensors [40], and quantum communication [70] are three major outcomes of the quantum information, which are still very active fields of research all over the work. In Quantum Photonics Lab (QPL) at the Institute for Quantum Computing (IQC), we focus on quantum communication to establish a free-space quantum channel and take advantage of Quantum Key distribution (QKD) to establish secure communication between the ground stations and satellites orbiting the earth.

1.1.1 Quantum Key Distribution

Charles Bennett and Gilles Brassard introduced the first quantum cryptography protocol based on Quantum Key Distribution (QKD), called BB84 [7], in 1984 and since then other protocols such as B92, BBM92 and E91 were developed [23][6]. These protocols use two laws of quantum mechanics to provide secure transmission of data, the Heisenberg uncertainty and no-cloning theorem [32][89][21][57]. Heisenberg uncertainty is typically defined as $\delta_x \delta_p \geqslant \hbar/2$; This equality is not limited to the position and momentum of

a quantum system and it is valid for any pair of complimentary variables of a particle, such as the polarization of the photon on different axis or two orthogonal components of the total angular momentum. Interestingly, the no-cloning theorem argues that copying an unknown quantum state is not feasible, unless the two states are orthogonal. The following example is a proof of this theorem [54]: Consider a cloning device that copies slot A to slot B. Slot A contains the data in form of a pure state $|\psi\rangle$ which needs to be copied to a standard pure state $|s\rangle$ in slot B. If the device starts with the initial sate of $|\psi\rangle \otimes |s\rangle$ and a unitary operator U performs the duplication, then this procedure can be defined as :

$$U(|\psi\rangle \otimes |s\rangle) = |\psi\rangle \otimes |\psi\rangle. \tag{1.1}$$

Now if we intend to copy the two pure states $|\psi\rangle$ and $|\phi\rangle$, we will have

$$\begin{aligned} U(|\psi\rangle \otimes |s\rangle) &= |\psi\rangle \otimes |\psi\rangle, \\ U(|\phi\rangle \otimes |s\rangle) &= |\phi\rangle \otimes |\phi\rangle. \end{aligned} \tag{1.2}$$

$$(U(|\psi\rangle \otimes |s\rangle))^{\dagger}.(U(|\phi\rangle \otimes |s\rangle)) = (|\psi\rangle \otimes |\psi\rangle)^{\dagger}.(|\phi\rangle \otimes |\phi\rangle), \tag{1.3}$$

$$\langle\psi|\phi\rangle \langle s|s\rangle = \langle\psi|\phi\rangle \langle\psi|\phi\rangle, \tag{1.4}$$

Hence,

$$\langle\psi|\phi\rangle = (\langle\psi|\phi\rangle)^2. \tag{1.5}$$

Therefore, for Eq. 1.5 to hold, either $|\psi\rangle = |\phi\rangle$ or $|\psi\rangle$ and $|\phi\rangle$ must be orthogonal. As a result, copying an unknown quantum state is not possible and no general cloning device exists [54]. However, by sacrificing the fidelity of the copied states, quantum copying machines (QCM) can exist. Universal QCM, State-dependant QCM, Symmetric QCM and Optimal QCM are examples of quantum cloners that can copy the input states only with limited fidelities and under certain circumstances [71].

Photons are mostly used in QKD experiments, since their properties allow for the encoding of information onto them and they travel close to light speed and hardly interact with their environment (e.g. they can travel through optical fibre or atmosphere while maintaining their properties). Degrees of freedom of a photon such as its polarization or angular momentum provides the required basis for this purpose. Thus in this project, the polarization states of a photon are considered as our QKD tool.

In quantum information studies, the fundamental unit is known as a quantum bit (qubit) which can be expressed as 0, 1 or a superposition of them. These units can be

2

mapped to points on the surface of a sphere, called Bloch sphere, to graphically visualize them. The unit vectors on the z axis ($+\hat{z}$ and $-\hat{z}$) represents the $|0\rangle$ and $|1\rangle$ states and any unitary operations rotate the vectors to create new states (Please refer to [54] for more information). Since the polarization of a photon is also a two-state system, it can be visualized by Bloch sphere as well. In optics, this sphere is also known as Poincaré sphere, which is commonly used to represent the polarization states (Fig. 1.1). It is conventional to consider $|0\rangle$ as the horizontal polarization state and $|1\rangle$ as the vertical state. Below are the three bases typically used to refer to the polarization states of a photon in QKD experiments.

- Horizontal ($+\hat{z}$) and Vertical ($-\hat{z}$):

$$|H\rangle = |0\rangle, |V\rangle = |1\rangle \tag{1.6}$$

- Diagonal ($+\hat{x}$) and Anti-Diagonal ($-\hat{x}$):

$$|D\rangle = \frac{|0\rangle + |1\rangle}{\sqrt{2}}, |A\rangle = \frac{|0\rangle - |1\rangle}{\sqrt{2}} \tag{1.7}$$

- Right ($+\hat{y}$) and Left ($-\hat{y}$)

$$|R\rangle = \frac{|0\rangle + i\,|1\rangle}{\sqrt{2}}, |L\rangle = \frac{|0\rangle - i\,|1\rangle}{\sqrt{2}} \tag{1.8}$$

Light Polarization

Polarization of a transverse wave is referred to the geometrical orientation of the plane in which the wave is oscillating. This plane is perpendicular to the propagation axis of the light. Monochromatic light has two oscillating planes that contain the electric field and the magnetic field separately. Polarization of light is conventionally known as the path of the plane that the electric field is oscillating in as the beam propagates. This path can be linear, circular, elliptical or etc, but the first three are more common in polarization studies. There are 6 common polarization states as mentioned above. $|H\rangle$, $|V\rangle$, $|A\rangle$ and $|D\rangle$ are the linear polarizations and $|L\rangle$ and $|R\rangle$ are the two circular ones. In investigating the reflection or refraction of light, it is convenient to use another coordinate formalism, which is defined by S and P. If the polarization of the wave is parallel to the incident plane before/after the reflection or refraction, the polarization is indicated as P (Parallel) and if it is perpendicular to the plane it is identified as S (German word for perpendicular).
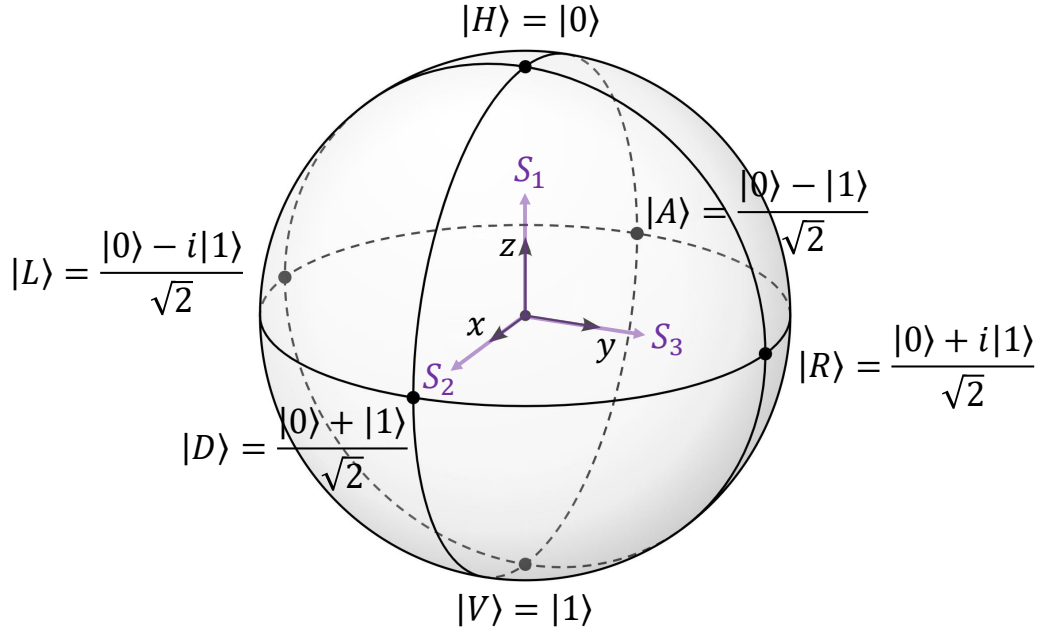
Figure 1.1: Representation of polarization states on Poincaré sphere.

Interaction of light with the atoms of a medium is wavelength dependent and can result in absorption, scattering and reflection or refraction. Birefringent materials have different indices of refraction for the two orthogonal polarization states of a transmitted light. They consist of a fast axis and a slow axis. If the polarization of light is along the fast axis, it experiences a lower index of refraction and as a result, it gains the maximum phase velocity, whereas the opposite occurs for the slow axis. The phase difference between the two axes is known as the phase retardance and is typically reported in wavelength units. The phase retardance is dependant on the material and the thickness of the medium, which is the baseline of constructing waveplates. In generating the six polarization states, a Half Waveplate (HWP) and Quarter Waveplate (QWP) are required to rotate the polarization and obtain the desired states. If the polarization vector is at angle θ with respect to the fast axis, HWP and QWP rotate the polarization by 2θ and θ respectively [68]. In chapter 5, to mathematically investigate the impact of waveplates on an input polarized light, we introduce Stokes vectors and use Mueller matrices to model HWP, QWP and a polarizer.

Stokes vectors are defined as

$$\vec{S} = \begin{pmatrix} S_0 \\ S_1 \\ S_2 \\ S_3 \end{pmatrix} = \begin{pmatrix} I \\ Q \\ U \\ V \end{pmatrix},$$ (1.9)

where I is the total intensity and Q, U and V represent H/V, D/A and R/L intensities. Fig. 1.1 shows the visual representation of polarization states with Stokes parameters on the Poincaré sphere.

Bennett and Brassard 1984 QKD Protocol

The Bennett and Brassard 1984 QKD protocol (BB84) uses a quantum commutation channel and a public classical channel to transmit data securely between 2 parties, Alice and Bob. Alice is traditionally known as the sender and Bob is the one who does the measurements required to receive the message. This protocol uses any two pairs of the polarization bases to transmit the qubits and generate a secure key between Alice and Bob. BB84 assumes the possibility of having an eavesdropper (Eve) in the quantum channel, disturbing the system by measuring the photon sent by Alice and changing the qubit going to Bob.

To demonstrate the protocol, first, Alice and Bob agree on the 2 pairs of bases and the assigned bit values for each state. Here, we consider having x-basis ($|H\rangle$ and $|V\rangle$) and z-basis ($|D\rangle$ and $|A\rangle$) states. Then the protocol is performed as below [7][54]:

1. Alice chooses random data bits, to be sent to Bob.

2. Alice chooses the bases, in which she wants to send the bits and she records both the bits and the bases.

3. Alice sends the selected states to Bob.

4. Once Bob receives the qubits, he measures them in either x or z basis and records the results.

5. Alice announces her used bases over the public channel.

6. Bob compares his bases with Alice's and discards the bits that were measured in the wrong bases.

7. Alice randomly picks a subset of bits to compare with Bob's measurement results. Any difference between the measured bits and the initial ones, indicates the presence of Eve[1].

8. Alice and Bob announce the chosen subset of bits to determine the number of the bits that agree. If this number is sufficient, according to the error tolerance of the protocol, the channel is considered safe and the remaining string of the bits can be used to form the raw key. If not, the protocol is aborted.

9. Alice and Bob perform post processing such as error correction [28][22][50][13] and privacy amplification [17] on the remaining raw key. Finally, they use their shared key with encryption algorithms such as One-Time-Pad [86][72][85] to securely transmit information .

The presence of Eve or any polarization distortions, results in a change in Bob's measured bits which is known as Quantum Bit Error Rate (QBER). The simplest attack model is the *measure-resend attack* that Eve interferes and measures the qubits going to Bob. There is a 50% chance that Eve measures in the correct basis and flips the bit before sending it to Bob. Moreover, there is 50-50% chance that Bob receives either the manipulated bit from Eve or the original bit from Alice. Therefore, presence of Eve, there is always a 25% error in the strings of bits shared between Alice and Bob. Hence, zero QBER implies having a secure channel free of Eve! A more generalized attack by Eve involve coherent interaction with the qubits. The ultimate security threshold of BB84 was first reported as 11% QBER [75], however by modifying the protocol the bit error tolerance has been increased up to 20% [51][31][30]. Furthermore, imperfections of the used component at each end and the the properties of the medium that the photon is traveling in, such as a lossy fibre or a turbulent atmosphere, can increase the QBER. Particularly, in free-space communications, atmospheric turbulence and the imperfections of the optics can distort the polarization of the transmitted photon noticeably. We argue these effects in the following section and suggest possible solutions to minimize the link loss.

1.2   Implementation of Quantum Key Distribution

QKD was first demonstrated in a research lab over 32 cm free space in 1992 [6] and extended to 100 km using optical fibres and Decoy state QKD, after 15 years [67][58].

---

[1]If Alice and Bob do the measurements in the same basis, the bits must also agree, if not the polarization of the photon could be distorted due to imperfections of the system or the bit could be changed by Eve.

Later, in 2016, *Hua-Lei Yin et al.* was able to reach up to 404 km over optical fibres, in their QKD experiment by taking advantage of the measurement-device-independent method [34] and then this limit was stretched to 509 km in 2020 [8][19][7]. However, to create a global commutation network, optical fibres alone are not sufficient, and free-space links are required to establish such wide network across various global locations. A free-space entanglement-based QKD performed over 144 km by *Ursin, R., et al.* [84] was an important milestone in 2007, that paved the path for ground-space communications. In 2017, *Sheng-Kai Liao, et al.* [48] achieved a satellite-to-ground QKD over 1,200 km using Miscius satellite in low-Earth-orbit (LEO). The key rate of 1.1 kbit/s obtained in this experiment was improved to 47.8 kbit/s by the same group in an article in 2021 [20]. The recent work, accomplished a quantum communication network between four cities of China, using about 700 fibre links and two high-speed satellite-to-ground free-space links, covering 4,600 km in total. The development of QKD since it was first introduced, has been tremendous in the the past few decades and has demonstrated the feasibility of attaining a global QKD network in near future.

1.3   Ground-Satellite Quantum Key Distribution

Ground-satellite QKD can be performed in an uplink or downlink configurations. A downlink refers to having a satellite-based transmitter and a receiver on the ground. This configuration generates a higher key rate since it experiences less photon loss and lower dark counts, as well as being almost immune to the atmospheric turbulence [9][39][33]. However, having the transmitter mounted on the satellite increases payload's total weight, which could elevate the complexity and cost of the project. On the other, uplink has no limitation on the weight or number of photon sources and can carry other optical components needed for error corrections or characterizations, such as polarization compensation[2] as well. Nonetheless, the effect of atmosphere in attenuating the link and reducing the key rate is unavoidable.

The Quantum Encryption and Science Satellite (QEYSSat) mission funded by the Canadian Space Agency (CSA) is a ground-satellite QKD demonstration in an uplink configuration for secure communications across Canada [35]. This experiment consists of a ground station and a microsatellite, orbiting the Earth at 500-600 km altitude in LEO, with a 30 cm aperture to detect the quantum signal transmitted from the Earth [9]. The ground

---

[2]The photon generated by the photon source travels through optics such as a telescope to be transmitted to the satellite. The polarization state might be distorted before leaving the telescope, so a polarization compensation is required at the aperture to do the correction.

station receives a beacon signal from the satellite and emits the quantum signal, such that it reaches the predicted location of the satellite. For this purpose, an Acquisition-Pointing-Tracking (APT) system is considered at both ends to track the satellite and establish the quantum channel successfully.

The science team working on this nationwide project is lead by Dr. Thomas Jennewein in Quantum Photonics Laboratory (QPL) group. A series of experiments performed by QPL group verified the feasibility of having a ground-to-satellite link and helped with the improvement of this mission [9][11]. The outdoor experiment that established a QKD link between a ground station and a receiver carried in a flying airplane at 3-10 km altitude, to model an airborne receiver, is one of the noticeable achievements [62]. In this experiment, for some passes of the plane over the transmitter, links were generated for few minutes, resulting in up to 868 kbit keys with 3-5% QBER. Hence, the viability of QEYSSat mission was confirmed.

In order to enhance the key rate to be practical for secure communications, we studied the ground station to minimize the link loss induced by the physical properties of the transmitter, such as the imperfections of the optics. In an uplink system, atmospheric turbulence has a dominant effect on the distortion of a transmitted beam. As the signal encounters the turbulent medium, it deviates from its original path and creates beam wandering on the receiver. In addition, the absorption and scattering of the photons by the atmosphere as well as the fibre coupling efficiencies at each end, reduce the detected power on the satellite. In polarization-based QKD, the turbulence and imperfections of the optics distort the wavefront of the quantum signal. As a consequence, it increases the QBER and the link attenuation. In this thesis, we investigate the factors that affect the link budget[3] in an uplink channel, such as atmosphere structure (chapter 2) and optical properties of the transmitter (chapter 3).

1.3.1 Requirements of a Free-Space Quantum Link

To reduce the link loss caused by the imperfections in the components, the ground station requires a transceiver[4] that is optimized to have the highest performance at the wavelengths used in the experiment. Considering the absorption of the atmosphere and the limited wavelengths that are compatible with current technology of photon detectors and photon sources, 785 nm has resulted in a higher key rate. Hence, it is recommended to be used as

---

[3]Link budget is an accounting of all the power losses and power gains that a signal experiences in a telecommunication system.

[4]A system that can be used both as a transmitter and a receiver.

the quantum signal [9]. However, the commercial optics and telescopes are not typically optimized at this wavelength which can significantly aberrate the transmitted beam. Also, the coating of the optics controls their transmittance and reflection, so it is crucial to select the coating such that it minimizes the link attenuation. Moreover, refractive telescopes are more preferred in this work since the secondary mirror of reflective telescopes blocks a portion of the transmitted beam which reduces the total power received on the satellite and also using them in polarization-encoded QKD experiments requires post processing to compensate for the polarization change in the reflection of the beam from the mirrors.

In chapter 2, we discuss the effective aperture size of our ground station, for which the link attenuation of an uplink is minimized[5]. We obtained an 8-inch lens is a reasonable trade-off between its performance and the costs. However, an 8-inch refractive telescope or an off-the-shelf lens designed and corrected for 785 nm use, is not easily available, since refractive telescopes typically come in smaller apertures and are mostly considered functional at visible or NIR spectrum for astronomy purposes, and commercial lenses with unique specifications are often built in small dimensions (1 inch) to be used in optics research labs. Furthermore, commercial telescopes commonly have a large field of view to allow observation of a larger portion of the sky, which is not ideal for satellite-ground communications, that desires to collect as much photons as transmitted by the ground station, on a small aperture on the satellite.

1.3.2 Custom-Designed Transceiver

Considering the constraints and requirements mentioned in the previous section and having almost no options in using commercial optics, we decided to have a custom-designed telescope. In chapter 3, the procedure of designing the lens and optimizing it for certain wavelength are provided. Furthermore, the specifications of the lens have been determined by modeling a far-field beam transmitted through our lens and detected by a satellite in the presence of atmospheric turbulence. As a result, we were able to reduce the total manufacturing costs by avoiding unnecessary procedures such as having smaller surface irregularity than needed, to achieve the required spot size and quality for the far-field beam at the satellite (Chapter 3).

Moreover, we designed the mechanical parts to facilitate the alignments and calibration of the telescope by adding folding mirrors. This approach was also beneficial in reducing the

---

[5]The link loss in free space in due to diffraction of the beam and the strength of turbulence. At a particular aperture size, the diffraction effect is dominant and increasing the diameter no longer helps with reducing the total link attenuation.

total length of the telescope, which made the scanning of the sky at higher elevation angles easier and kept the tube's thermal condition more stable. The details of the mechanical design are thoroughly discussed in Chapter 4. Finally, we characterized the telescope's performance to validate our designs and confirm our ground station's ability to transmit signals at certain wavelengths, with minimum wavefront distortion and high polarization preservation (Chapter 5).

QPL new ground station consisting of the custom-designed transceiver, two different photon sources (weak coherent pulses and entangled photon sources[36]), the APT system, and any potential optical configurations for error correction is going to be used in free-space QKD tests and studies to improve the link budget and the secure key rate generated in the upcoming QEYSSat experiments and ultimately, get Canada one step closer to establish a secure quantum communication network across the country.

Chapter 2

Atmosphere vs. Free-Space Optical Links

An important aspect of quantum communication is analyzing and approximating the transmission loss in the quantum channel. Particularly, for free-space quantum communication the impact of atmospheric effects such as beam wander, beam spread, scintillation, pointing error, and link attenuation that occur to the detected beam due to traveling through a turbulent medium, must be well understood to obtain a successful communication between the satellite and the ground station. Furthermore, choosing the right orbit for the satellite, the best location for the ground station and the best time for the experiment can help with mitigating the errors significantly.

In this chapter, we introduce the factors affecting the link efficiency and discuss the link attenuation for an uplink. Specifically, these discussion are used to determine the optimal telescope aperture size required for the quantum photonics lab (QPL) quantum optical ground station telescope for the QEYSSat mission. Later on, we present the tracking system used for establishing a channel with a moving satellite and propose the modification needed for our current device.

2.1   Atmospheric Turbulence

Fluid dynamics introduces "Turbulence" as a chaotic change in the pressure or velocity of the fluid. Considering the atmosphere as a viscous fluid, the temperature gradient changes the velocity of the wind which gives a rise to fluctuations in the index of refraction of the

atmosphere. In other words, the atmosphere acts like small lenses with random indices of refraction which are called optical turbules or eddies. As a result, the beam spot radius spreads more than that from the diffraction alone, which causes power loss in the detected beam. Temporal and spatial fluctuations in the irradiance (scintillation) and phase of the beam, are other impacts of eddies on the propagating beam through the turbulent atmosphere.

To study the turbulence, different models are presented such as H-V model, HAP model, AFGL AMOS Night model, and SLC Day and Night models [4]. In this work, we are looking at small zenith[1] angles (less than 60° or 45° in case of strong ground-level turbulence) and using weak fluctuations theory based on the Rytov approximation. Based on Hufnagel-Valley (H-V) atmospheric model [4][43], the *Structure Parameter* (C_n^2) of the atmosphere can be defined for different altitudes (h) considering the geographical location conditions (V and A). This parameter measures the strength of the fluctuations in the refractive indices at different parts of the atmosphere. For example, C_n^2 can be considered constant over fixed horizontal paths during short time intervals. However, for vertical or slant paths, C_n^2 varies noticeably with height. At low altitudes, the atmosphere has a thermal exchange with the Earth surface which is called atmospheric boundary layer (ABL) and extends to 1 or 2 kilometres [43]. In this region, the temperature gradient varies in day and night. During daytime, thermal plumes occur which guide warm and less dense air to rise. However, at night the Earth is surrounded by cold air which is less likely to rise and it is more stable. Thermally neutral condition happens near sunset and sunrise. Atmospheric structure parameters of ABL varies with altitude as below [16]:

$$C_n^2(h) = C_n^2(h_0)(\frac{h}{h_0})^{-b}, \tag{2.1}$$

Where h is the altitude, b is experimentally found between 4/3 for unstable conditions (day) and 2/3 for neutral or stable conditions (night). As a result, a plot of path-averaged values of C_n^2 over 24 hours, near the ground (1.5 m above the Earth), shows a diurnal cycle that reaches its maximum in the mid-day, is almost constant during the night and has its minimum near the sunset and sunrise. Therefore, near the sunset, which is thermally stable and has less sun reflection than the sunrise, has been suggested as the ideal time for free-space optical communication.[43]

To model the propagation of a beam that travels on a vertical or slant path, different models are presented. The propagated beam profile can vary from day to night. Here, we

---

[1]Zenith angle is the angle measured from the vertical. As the zenith angle increases, the beam path gets longer (considering the same height). As a consequence, the beam experiences more turbulence effects.

use a more general and widely used C_n^2 profile model based on H-V, which predicts that the atmosphere structure changes exponentially relative to the altitude [43],

$$C_n^2(h) = 0.00594(\frac{V}{27})^2(10^{-5}h)^{10}exp(-\frac{h}{1000})+2.7\times10^{-16}exp(-\frac{h}{1500})+Aexp(-\frac{h}{100}). \quad (2.2)$$

Here, V is RMS wind speed which is normally 21 m/s and $A_0 = 1.7 \times 10^{-14}m^{-\frac{2}{3}}$ is the nominal value of C_n^2 on the ground. $C_n^2 > 10^{-13}m^{-2/3}$ is considered as a strong turbulence, whereas $C_n^2 \approx 10^{-16}m^{-2/3}$ is within weak turbulence regime at ground level [16][80]. As suggested by many researchers, the last term of this equation can be replaced by Eq. 2.1, to consider temperature gradient during different times of a day at lower altitudes[2]. The optical wave experiences loss of spatial coherence and fluctuations of its intensity as it goes through the turbulence. Therefore atmospheric coherence diameter r_0 (also known as Fried's parameter) for a beam propagating over a path of length H is defined as,

$$r_0 = (0.423\mu_0 k^2 \sec \zeta)^{-\frac{3}{5}},$$
$$\mu_0 = \int_{h_0}^{H} C_n^2(h)dh. \quad (2.3)$$

Fried's parameter indicates that how long the spatial coherence of the signal can be preserved, so it affects the irradiance and phase fluctuations of the detected beam. For instance, a large r_0 means that the coherence is preserved over a longer path and the turbulence is relatively weaker. Moreover, Fried's parameter can be interpreted as the radius of an aperture that the propagating beam is passing through. The diffraction occurs due to this aperture, increases the beam divergence which results in the power loss at the far-field beam. (The link attenuation is discussed in Sec. 2.1.6.)

The atmosphere stretches to approximately up to 700 km above the Earth, but the most turbulent regions are at low altitudes. Hence, the effects of turbulence is significantly different in an uplink and downlink since in an uplink the transmitter is close to the turbulent layers whereas, in a downlink the receiver is based on the Earth. The issues caused by the turbulence at the beginning of the path persists throughout the beam propagation toward the satellite so the turbulence is much more detrimental in uplink. On the other

---

[2]Larry C. Andrews, has modified Eq. 2.2, in his recent paper, by considering Eq. 2.1 and a scaling factor to represent the strength of the average background turbulence at high altitudes, to have a more precise model of the atmosphere structure [80].

hand, in downlink the beam is larger and has a higher spatial coherence when it confronts the turbules at the end of its path, so that it is saved from significant distortions. This research focuses more on uplinks and studies the behaviour of a beam propagating toward a satellite in *Low Earth Orbit (LEO)*.

2.1.1   Earth Orbits

Before discussing the turbulence experienced by the optical signal propagating during an uplink, we will first argue the reason behind choosing LEO for QKD experiments. Orbits of the Earth are divided into 3 groups according to their altitude and are used for different purposes based on these specifications. Fig. 2.1 and Table 2.1 show the orbits altitudes and orbital periods[56][66][43].
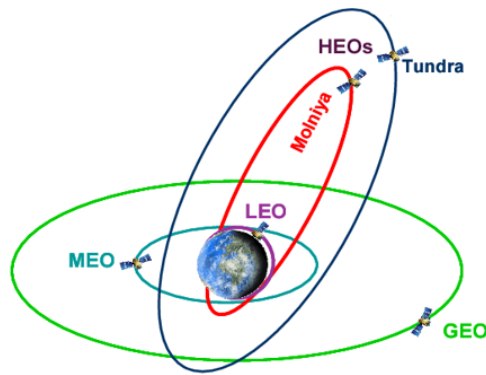
Figure 2.1: Earth orbits at different altitudes. LEO (Low Earth Orbit): Mostly used for science applications. MEO (Medium Earth Orbit) suitable for navigation and communication satellites. GEO (Geostationary Orbit): Important to weather forecasting satellites. HEOs (Highly Elliptical Orbits): Tundra and Molniya orbits are two well-known HEOs. Communication satellites in theses orbits provide continuous coverage for the users in higher latitudes such as the North/South Poles, Russia, North America and etc. [77]

A Geostationary Orbit (GEO) is the furthest to the surface of the Earth and at the altitude of about 35,786km and which takes 23 hours 56 minutes and 4 seconds to orbit the Earth (Almost the same as the Earth's) [91][43]. Therefore, a satellite in this orbit is always spotted over a single place which is extremely valuable for weather forecasting satellites [66].

Medium Earth Orbit (MEO) is about 2,000 to 35,786 km which orbits the Earth every 12 hours and is mostly used for navigation and communication satellites such as GPS [66].

Orbit	Altitude	Orbital Period
Geostationary (GEO)	35,786km-41,680 km	Equal to Earth
Medium Earth Orbit (MEO)	$\sim$ 20,200 km	12 hours
Low Earth Orbit (LEO)	180–2000 km	90 min

Table 2.1: Different Earth orbits

Low Earth Orbit (LEO) is the closest to the Earth with an orbital period of about 90 minutes. This orbit is from 180 to 2,000 km and has the fastest speed relative to the other orbits. Moreover, typically at 600 km to 800 km, a sun-synchronous orbit exists, which indicates that a satellite in this orbit always has the same relative position to the sun. As a result, it allows the satellite to always pass a particular part of the Earth at the same local time. Also, the angle of the sunlight on the Earth is kept as consistent as possible which makes this orbit useful for science applications, particularly quantum communication experiments [66].

Since LEO is the closest orbit to the Earth, it experiences the minimum diffraction loss, which is advantageous for quantum key distribution experiments. However, a slower orbit (such as MEO or GEO) enables a continuous link which allows for performing QKD for a longer time. Despite this advantage, MEO and GEO suffer from a high rate of radiation and greater propagation loss [56]. In addition, other complications such as the higher probability of sunlight reflecting off of the satellites to the ground station can be problematic and probably more detrimental is the financial burden since MEO and GEO missions require larger budgets. As mentioned earlier, LEO has a higher speed which not only reduces the allowable link time between the ground station and the satellite but also increases the pointing requirements. However, the reduced amount of loss, smaller amount of diffraction as a consequence of the short link distance, and requiring a lower budget comparing to the other orbits, make the LEO the preferred orbit for QKD satellites [56]. As a consequence, the QEYSSat mission has chosen LEO for free-space quantum communications. Hence, in this section, we investigated the properties of a link, established between a ground station and the QEYSSat satellite at 600 km above the Earth, to comprehend the potential sources of link loss in a quantum communication channel.

2.1.2   Beam Spread and Beam Wander

Turbulent atmosphere generates eddies that vary in size. Big eddies can cause a significant deviation in the path of a beam toward a satellite (Fig. 2.2(a)). Since the turbulence is

(a)

(b)
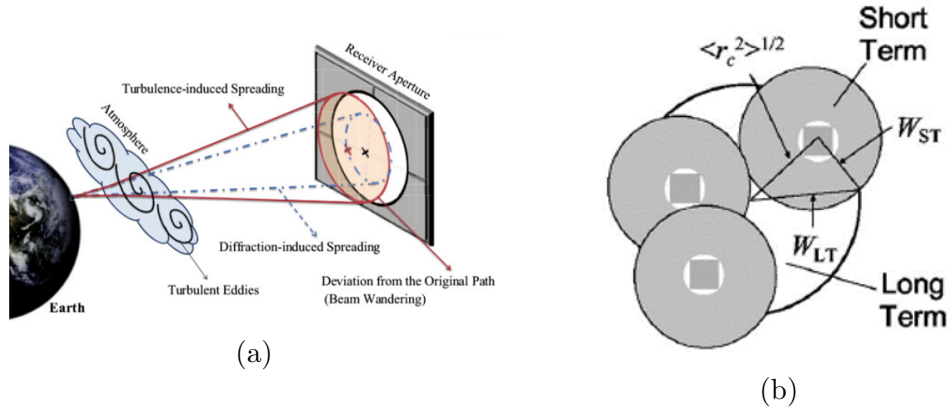
Figure 2.2: (a) A Beam transmitted from a ground station deviates from its original path due to turbulent eddies [73]. (b) Short/long term beam spread on the satellite [42]. $\langle r_c^2 \rangle^{1/2}$ is the beam wander which represents the distance from the center of the short term spot to the long term one.

changing randomly, the beam can be detected on different spots on the satellite, so a good approximation of the beam location is the average spot location over a certain time. We use *Short Term* (W_{ST}) and *Long Term* (W_{LT}) beam spread to distinguish between the detected spots in short intervals and the averaged one (Fig. 2.2(b)). From weak fluctuations theory (W_{LT}) is defined as:

$$W_{LT} = W\sqrt{1+T},$$
$$T = 1.33\,\sigma_R^2\,\Lambda^{5/6},$$

where W is diffracted beam waist, $\sigma_R^2 = 1.23\,C_n^2\,k^{7/6}\,H^{11/6}$ is the Rytov variance which indicates the scintillation index of a plane wave in weak fluctuations regime and it is proportional to the atmosphere structure (C_n^2) and the distance between the transmitter and the receiver (H) to imply the strength of the turbulence, $\Lambda = 2H/kW^2$ (k is the wave number) is the beam parameter and T represents the change in the mean on-axis irradiance of the beam on the satellite [43]. To be more specific, we can rewrite the equation in terms of large-scale and small-scale turbulence :

$$W_{LT}^2 = W^2 + W^2 T_{SS} + W^2 T_{LS} = W_{ST}^2 + \langle r_c^2 \rangle. \tag{2.4}$$

Here, T_{SS} refers to Small Scale (SS) eddies that cause on-axis irradiance fluctuations, so $W^2 T_{SS}$ adds an additional beam spreading to the diffracted beam spot (W) on the

16

satellite which is known as *Beam Breathing*. Therefore, $W^2 + WT_{SS}^2$ can be considered as the short-term beam spread W_{ST}^2. Moreover, The last term in Eq. 2.4 is responsible for the displacement of the spot center on the detector, that occurs due to Large Scale (LS) eddies. This effect is called *Beam Wander* ($\langle r_c^2 \rangle$). Finally, by substituting T and using approximations each term is derived as below. (Please refer to [43][26] for more details.)

$$W_{ST}^2 = W_0^2(1 + \frac{h^2}{Z_0}) + 2\left(\frac{4.2h}{kr_0}(1 - 0.26(\frac{r_0}{W_0})^{\frac{1}{3}})\right)^2, \tag{2.5}$$

$$\sqrt{\langle r_c^2 \rangle} = 0.73(H - h_0)\sec(\zeta)(\frac{\lambda}{2W_0})(\frac{2W_0}{r_0})^{\frac{5}{6}}, \tag{2.6}$$

$$W_{LT} = \begin{cases} W(1 + (\frac{D_0}{r_0})^{\frac{5}{3}})^{\frac{1}{2}} & 0 \ll (\frac{D_0}{r_0}) \leq 1 \\ W(1 + (\frac{D_0}{r_0})^{\frac{5}{3}})^{\frac{3}{5}} & 1 < (\frac{D_0}{r_0}) < \infty \end{cases} \tag{2.7}$$

W_0 is the initial beam waist at the exit of the transmitter and D_0 is the telescope aperture diameter. Here D_0 is considered[3] as $D_0^2 = 2^3 W_0^2$. Using Eq. 2.7, the long term beam spread transmitted from a 20 cm aperture, in presence of a weak turbulence $r_0 = 8.5$ cm, results in a 5.58 m beam on a receiver in LEO.

2.1.3 Strehl Ratio

Intensity of the detected beam on the satellite can be reduced due to turbulence and optical aberrations. This change is defined by Strehl ratio (S), which is the ratio of the measured on-axis intensity of the detected spot ($\langle I(0, L) \rangle = I_0(W_0^2/W_{LT}^2)$), to the diffraction-limited one.

$$\langle S \rangle = \frac{\langle I(0, L) \rangle_{W_{LT}}}{\langle I(0, L) \rangle_W} = (\frac{W}{W_{LT}})^2 = \frac{1}{1 + T}, \tag{2.8}$$

$$\langle S \rangle \cong \begin{cases} (1 + (\frac{D_0}{r_0})^{\frac{5}{3}})^{-1} & 0 \ll (\frac{D_0}{r_0}) \leq 1 \\ (1 + (\frac{D_0}{r_0})^{\frac{5}{3}})^{\frac{-6}{5}} & 1 < (\frac{D_0}{r_0}) < \infty \end{cases} \tag{2.9}$$

---

[3]This assumption is discussed later in Section 2.2.3
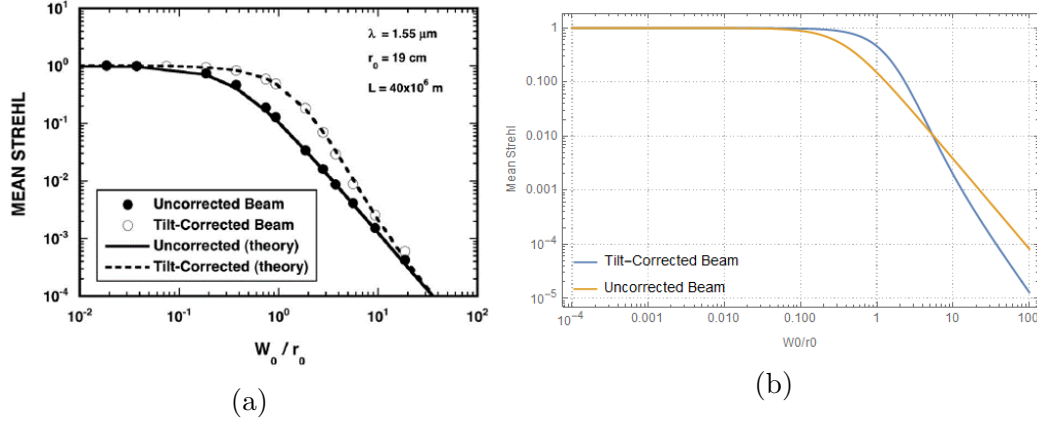
Figure 2.3: (a) Measured and theoretical on-axis mean Strehl ratio for both uncorrected and tilt-corrected beam provided in [42]. (b) Calculated on-axis mean Strehl ratio for $\lambda = 785$ nm and H = 600 km according to Eq. 2.9 and Eq. 2.10 .

$$\langle S \rangle_{tilt-corrected} = \big(1 + (5.56 - \frac{4.84}{1 + 0.04(\frac{W_0}{r_0})^{5/3}}) \times (\frac{W_0}{r_0})^{5/3}\big)^{-6/5} \tag{2.10}$$

If the size of the beam is much smaller than the Fried parameter, Strehl ratio can be about one, but if it gets larger or r_0 decreases (strong turbulence) then Strehl ratio goes to zero. However, by utilizing adaptive optics and implementing tilt corrections this ratio can be increased. Fig. 2.3 shows the plots for a measured and theoretical mean Strehl ratio for both uncorrected and tilt-corrected beam presented in [42] and the results of our calculations for a beam at 785 nm and a receiver at 600 km above the Earth.

In conclusions, it is preferred to keep the beam waist in the same order as the atmospheric coherence parameter to obtain a high on-axis Strehl ratio on the satellite. Details on a tilt corrected beam can be found in [42] and [43]

2.1.4 Scintillation

In addition to the reduction of the average intensity of the beam in far-field, there can also be temporal fluctuations in the irradiance. Since the beam goes through random turbules, the detected power on the satellite varies according to the ratio of the beam waist to the coherence parameter. To estimate the fluctuations, *Scintillation Index* is used which represents the variance of intensity over the mean value:

18
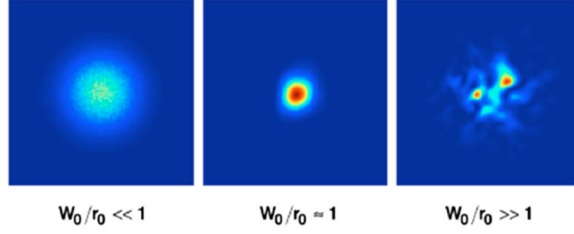
Figure 2.4: Beam profile in far field for different W_0 and r_0 ratios [42]

$$\sigma_I^2 = \frac{\langle I^2 \rangle - \langle I \rangle^2}{\langle I \rangle}. \tag{2.11}$$

Here $\langle I \rangle$ is the mean irradiance on the detector at H distance. Intensity can be defined in 2 terms: 1) On-axis intensity, 2) Intensity at r distance from the optical axis. Therefore, we can rewrite the scintillation index as $\sigma_I^2(r, L) = \sigma_I^2(0, L) + \sigma_{I,r}^2(r, L)$, where it represents the longitudinal and radial components separately. More detailed calculations of this index are beyond the scope of this work. They have been investigated in details in [26] and [43].

Fig. 2.4 shows a far-field beam in presence of atmospheric turbulence, for different ratios of W_0/r_0, which goes from a diffraction-limited image to speckles of light after the beam breaks up and saturation happens [42]. In other words, when the beam waist is much larger than r_0, the turbulence acts like a series of different lenses that each refracts the light separately.

However, in polarization-encoded QKD having beam speckles or aberrations are acceptable only if the detected beam has the required gain and the initial polarization is preserved. As a result, the transmitter with an aperture equal or larger than the atmospheric coherence diameter will be optimal for the photon transmission.

2.1.5 Pointing Error

In establishing a ground-to-satellite link, pointing and tracking are of great importance to have a better link budget. *Lead-Ahead Error, Aperture Mismatch* and *Beam Wander* are the main reasons for a pointing error in ground to space communication. Since the satellite is orbiting the Earth with v velocity, the signal leaving the transmitter should be pointed towards the future location of the satellite to avoid missing the satellite aperture, this is called lead-ahead error (Fig. 2.5b). To facilitate the tracking and reduce the pointing error,

19
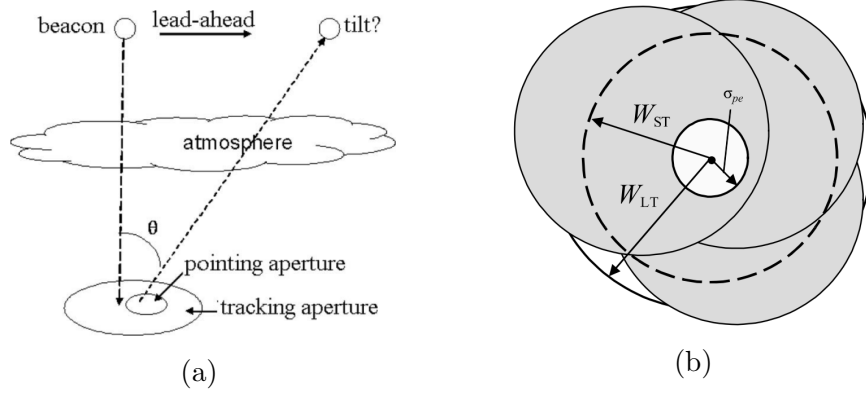
Figure 2.5: (a) aperture mismatch and lead a head error in a ground-to-satellite optical link [69]. The pointing aperture must have an overlap with the tracking aperture. (θ is the pointing angle). (b) Wander-induced pointing error [43]; The middle white circle indicate the pointing error for $W_0 < r_0$.

the satellite has a beacon light, which is detectable by the ground station and helps with transmitting the quantum signal at the correct angle. Due to the constraints on the design of the ground stations and satellites, the location and size of the apertures receiving and sending the beacon light, might vary. If this difference is not taken into consideration, it can increase the pointing error, that is commonly known as aperture mismatch (Fig. 2.5a). As a conclusion, to obtain the correct pointing angle in transmitting a signal to a satellite, it is crucial to study the impacts of lead-ahead and aperture mismatch as well as the turbulence effects such as beam wandering, to minimize the loss in a free-space link [59][69].

To formulate the wander-induced pointing error, we use the same approach as Eq. 2.1.2. We consider W^2T as the variance of the pointing error that occurs to a detected beam on the satellite, that has a waist smaller than the spatial coherence width: $W_0 < r_0$. ($W_0 > r_0$ beam breaks up and we can no longer look at the beam wander of the centroid)[43][42] The pointing error variance σ_{pe}^2 is expressed as:

$$\sigma_{pe}^2 = \langle r_c^2 \rangle \left(1 - \left(\frac{C_r^2 \frac{W_0^2}{r_0^2}}{1 + C_r^2 \frac{W_0^2}{r_0^2}}\right)^{\frac{1}{6}}\right). \tag{2.12}$$

$\langle r_c^2 \rangle$ is the mean beam wander from Eq. 2.6 and C_r^2 is a scaling factor which is typically about 2π. We can simplify this equation based on its asymptotic behavior for different $2W_0/r_0$ values, as below [43].

20

$$\sigma_{pe}^2 \sim \begin{cases} (\frac{\lambda}{2W_0})^2 (\frac{2W_0}{r_0})^{\frac{5}{3}} (H - h_0)^2 \sec^2(\zeta) & \frac{2W_0}{r_0} \ll 1 \\ (\frac{\lambda}{2W_0})^2 (\frac{r_0}{2W_0})^{\frac{1}{3}} (H - h_0)^2 \sec^2(\zeta) & \frac{2W_0}{r_0} \gg 1 \end{cases} \tag{2.13}$$

In other words, if $\frac{2W_0}{r_0} \ll 1$ then $\sigma_{pe}^2 \approx \langle r_c^2 \rangle$ and since the beam waist at the satellite is quite large, $T = \frac{\sigma_{pe}^2}{W^2}$ gets relatively small; and if $\frac{2W_0}{r_0} \gg 1$, σ_{pe}^2 goes to zero. Therefore, it can be said that, in an uplink configuration, beam wander has small effects on the scintillation of the centroid, in either way [42].

2.1.6   Link Attenuation

To compare the difference in the mean power received by satellite and the mean power transmitted by the ground station, we use a parameter called *Link Attenuation*. Link attenuation depends on the pointing error of the experiment, diameter and transmission factors of both the ground transmitter and satellite telescope. If

1. The receiver is at far-field of the transmitter ($H \gg \frac{D_t^2}{\lambda}$).

2. The telescope is diffraction-limited.

3. There is no atmospheric turbulence.

the link attenuation can be expressed as,

$$A = \frac{H^2 \lambda^2}{D_T^2 D_R^2} \frac{1}{T_T (1 - L_P) T_R}, \tag{2.14}$$

Where λ is the wavelength of the beam transmitted from a telescope with D_T aperture diameter and T_T transmission factor and L_P the pointing loss, and received by a satellite with D_R and T_R. This equation can also be used in a downlink (2.2.2) where turbulence effects are negligible [5].

On the other hand, as mentioned before, turbulent atmosphere can cause a significant loss in an uplink (2.2.3), so we need to introduce an atmospheric parameter in Eq. 2.14 to have a correct estimate of the link loss [5]:

$$A = \frac{H^2 (\theta_T^2 + \theta_{atm}^2)}{D_R^2} \frac{1}{T_T (1 - L_P) T_R} 10^{\frac{A_{atm}}{10}}, \tag{2.15}$$
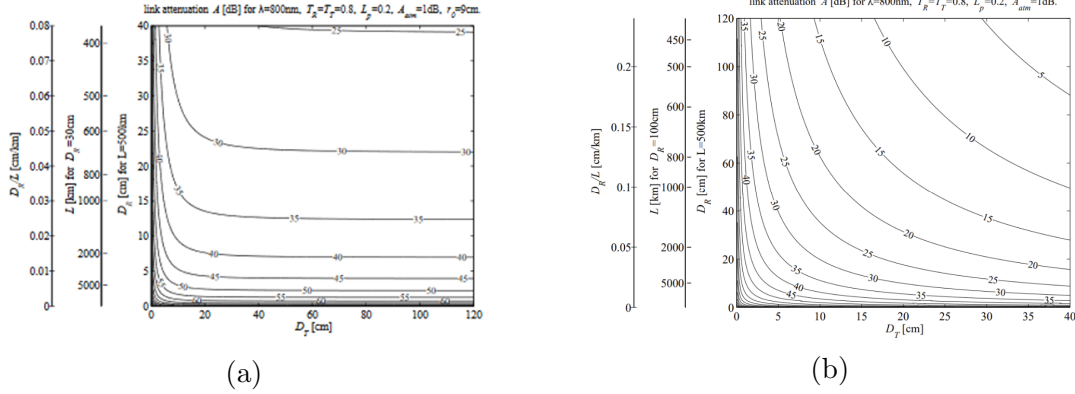
Figure 2.6: ; counter plots of link attenuation in (a) an uplink and (b) a downlink, for different aperture diameters of the receiver and the transmitter. Ground aperture: 1m, LEO aperture: 20 to 30 cm, transmission factors: $T_T = T_R = 0.8$, pointing loss: $L_p = 0.2$, $r_0 = 9$ cm and $\lambda = 800$ nm. [5]

Where $\theta_T = \frac{\lambda}{D_T}$ and $\theta_{atm} = \frac{\lambda}{r_0}$ are the divergence angles due to the transmitter aperture and the presumed r_0 radius aperture caused by the turbulence, respectively.

It should be noted, that link attenuation includes the beam spreading due to atmospheric turbulence, beam diffraction and pointing error. However, losses due to optical elements and detector efficiencies are not considered[4].

Fig. 2.6 illustrates that increasing the aperture size of the transmitter is not linearly proportional to the loss. With increasing the diameter of the transmitter, link attenuation reduces but beyond a certain number, enlarging the aperture has no effect on the link budget. Fig. 2.6a shows a contour plot of A as a function of the transmitter aperture size. It determines that for any size of the aperture, the attenuation is less than 60 dB. In addition, it suggests that for a 30 cm satellite and relatively weak turbulence, the effective diameter of the transmitter ($D_T = 2W_0$) should be about 40 cm, since a larger aperture has no advantage on reducing the loss [5][9].

In practice, this parameter depends significantly on the altitude and weather of the experiment location. Clearly, having no fog, haze or clouds, and choosing a high altitude location helps with mitigating atmospheric effects.

---

[4]These losses were reported as 3 dB for each photon link and 3.5 dB for each detector in [5].

2.2 Ground-Satellite Link

2.2.1 Wavelength Considerations

A major contributor in having a low loss ground-satellite channel is the choice of wavelength. There are several factors to consider when finding the optimal wavelength for a quantum communication link. For instance, different wavelengths experience different absorption and scattering rates while propagating through the atmosphere. Longer wavelengths suffer less from atmospheric turbulence and absorption, whereas, shorter wavelengths have less diffraction loss. Furthermore, the availability of different wavelengths for photon sources and single photon detectors are limiting factors that must be taken into consideration while choosing the wavelength. Bourgoin *et al* [9] investigated the existing challenges with commercially available photon detectors and provides key rates achieved at different wavelengths for an uplink and a downlink using both weak coherent pulse (WCP) and entangled photon sources. As a reult, 785 *nm* is suggested as an optimal wavelength for free-space QKD. Currently, InGaAs APDs and superconducting single photon detectors are used for Infrared wavelengths. InGaAs APDs have low efficiency with high dark count, while superconducting single photon detectors can have higher performance. However, with today technology, they only work at cryogenic temperatures which makes them impractical for low cost ground-satellite projects. In the future with improvements in photon detectors, longer wavelengths with higher key rates will be more applicable [9].

2.2.2 Downlink

If a satellite carries an optical transmitter[5], and a ground station is used as a receiver, the channel created is called *Downlink*. Downlinks do not suffer as much as uplinks from atmospheric turbulence, since the turbulent layers are closer to the receiver on the ground, and the beam only confronts the eddies at the very end of its path. Therefore, the turbulence-induced aberrations can be ignored, and only the fibre coupling loss due to beam wander needs be considered. As a consequence, the downlink experiences less link loss and has better key rates, when compared to an uplink. However, setting up the transmitter on the satellite can be quite challenging due to the payload capacity of satellites and the big budget and advanced technologies required for that.

---

[5]An optical transmitter is a telescope that uses a photon source to transmit photons towards a receiver. In other words, the signal is prepared at the focal point, to obtain a collimated beam after the telescope aperture and propagates on a path that the telescope is pointing to.
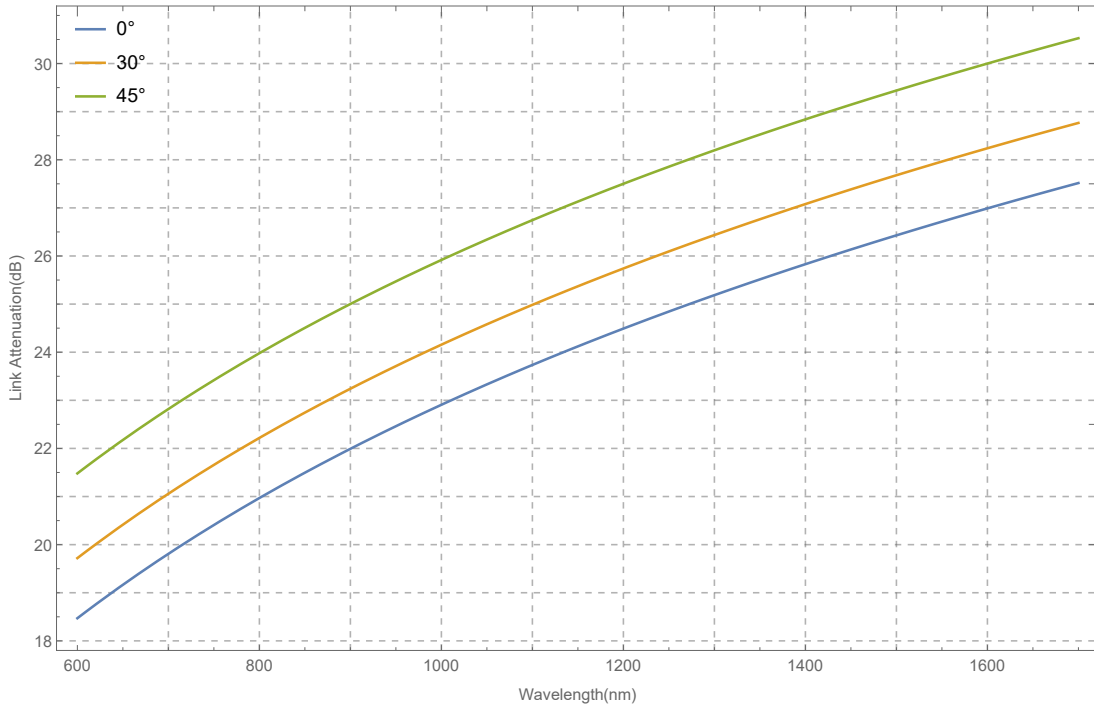
Figure 2.7: Preliminary estimation of link attenuation as a function of wavelength for a downlink, at 0°, 30° and 45° zenith angles. The shortest distance between the transmitter and the receiver (0° zenith angle) is 600 km and atmospheric turbulence is neglected. Telescopes transmission factors, $T_T = T_R = 0.8$; Pointing loss $L_P = 0.2$; Transmitter and receiver diameters, $D_T = 30$ cm, $D_R = 20$ cm.

To estimate the loss of the channel, one can ignore turbulence effects at first orders, take Eq. 2.14 into consideration and add the fibre coupling efficiencies, detectors efficiency and other optics imperfections. Fig. 2.7 shows the link attenuation for 600 nm to 1700 nm wavelength for different zenith angles. Larger angles correspond to longer paths of the beam. So clearly, the minimum loss occurs when the satellite is above the ground station. Modelling a downlink with regard to potential loss sources such as single mode and multi mode fibre coupling efficiency is beyond the scope of this work but in plans for future works.
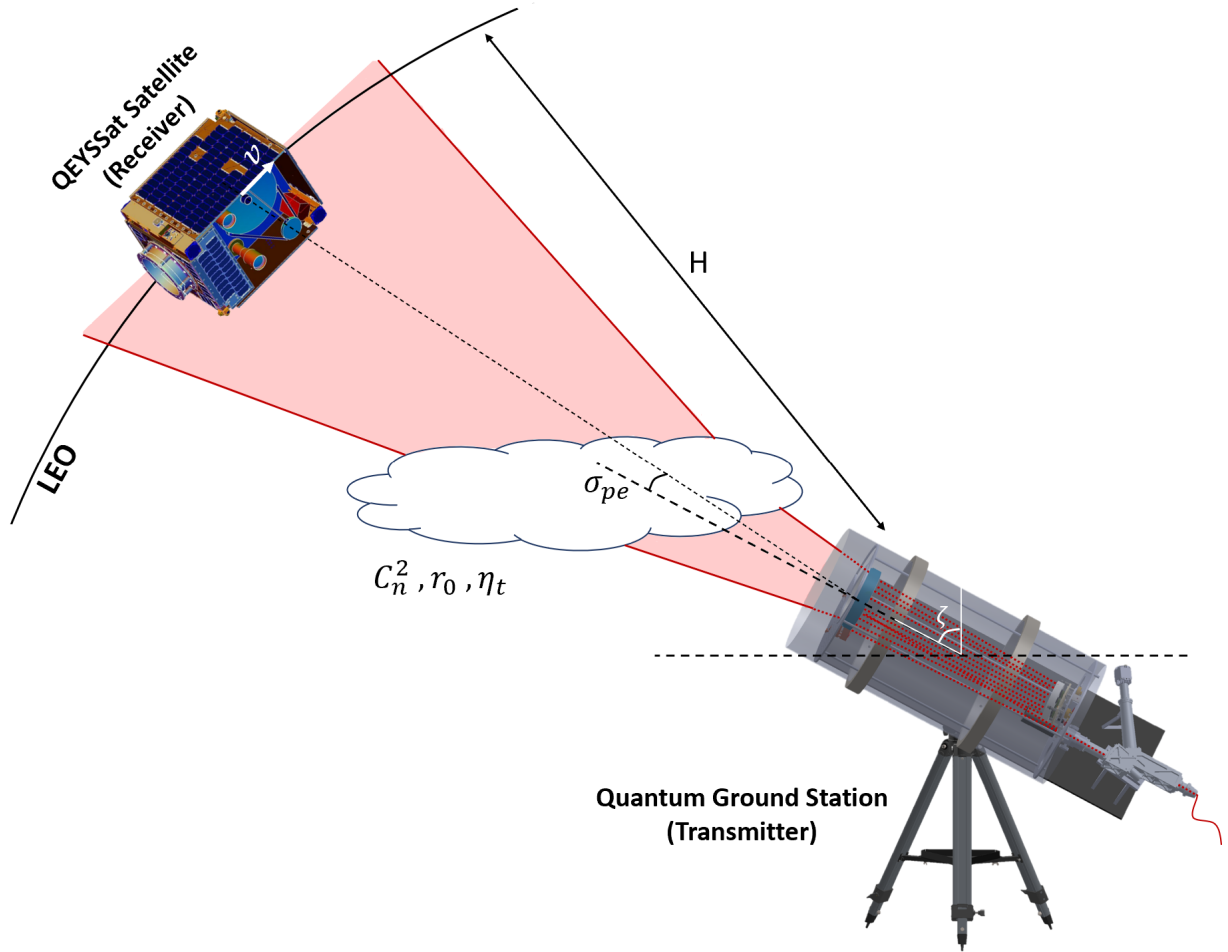
Figure 2.8: Uplink configuration between QEYSSat satellite [35] and our custom-designed telescope, in presence of atmospheric turbulence (r_0, C_n^2). H, distance between the transmitter and the receiver; ζ, zenith angle; σ_{pe}, pointing error; η, atmospheric transmittance.
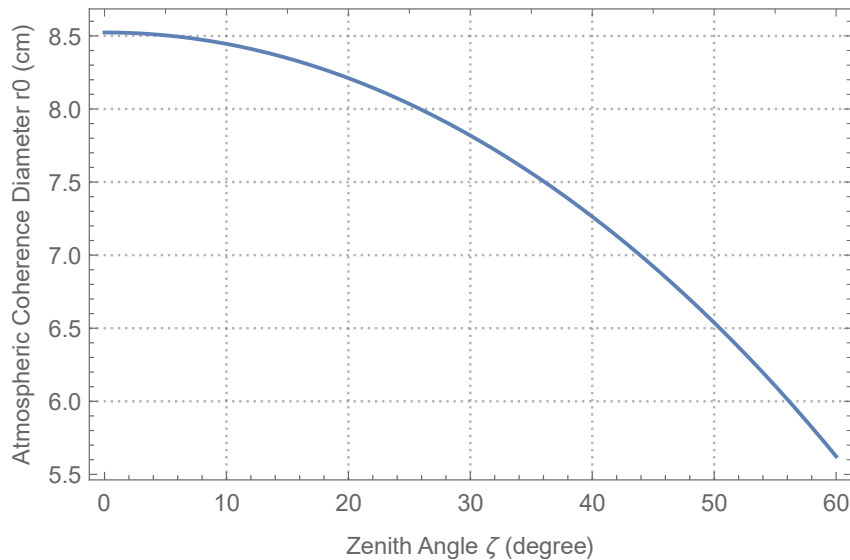
Figure 2.9: Variation of atmospheric coherence diameter (r_o) over 0 to 60° zenith angles at 785 nm. This is calculated using Eq. 2.3 and Eq. 2.16.

2.2.3 Uplink

The purpose of this thesis, as mentioned before is building the optical transmitter of our ground station for having a better link budget in an uplink. As illustrated in Fig. 2.8, in an uplink configuration, the beam goes through turbulent layers of the atmosphere shortly after leaving the transmitter. So it is crucial to have the right beam size to pass the eddies successfully and get detected by the satellite. In this section we discuss the analysis of determining the appropriate aperture size of the telescope for a successful high efficiency uplink. This analysis considers the both atmospheric effect discuss in Section 2.1 and manufacturing limitations.

Effective Aperture Size of the Telescope

Our ground station is designed to establish a quantum channel with a satellite at 600 km above the Earth, in LEO orbit. The satellite carries the photon detectors and it is considered to have a 30 cm aperture to receive the signal. The practical pointing loss (L_P) is set at 0.2 and the transmittance of the transmitter and the receiver are assumed to be 0.8 at 785 nm [9]. Given these parameters, we estimated the link attenuation to determine the optimal aperture size. Since the major loss in an uplink is caused by the turbulence,

26
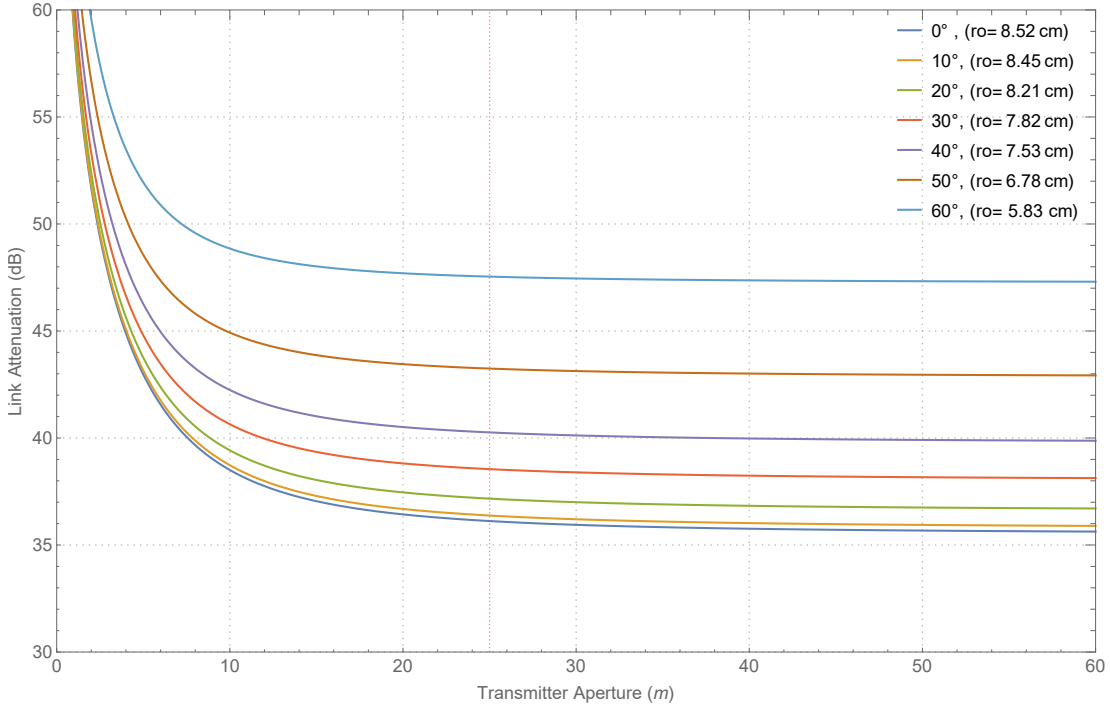
Figure 2.10: Calculated link attenuation as a function of transmitter aperture size. The atmospheric loss is almost constant for apertures larger than 25 cm.

in Fig. 2.9 we plotted the atmospheric coherence diameter (r_0), over $0°$ to $60°$ zenith angle using Eq. 2.3, to achieve the maximum coherence diameter, we can expect given the initial design constraints mentioned above. However, these r_0 values are only estimations over short intervals of time and one location for which the weather condition is relatively constant. In reality, r_0 is continuously changing, since the atmosphere structure varies for different conditions. Furthermore, as increasing the zenith angle results in a larger distance between the satellite and the ground station (H), we considered the distance as a function of the zenith angle in Eq. 2.3:

$$H = \frac{H_0}{\cos \zeta}. \tag{2.16}$$

H_0 is 600 km as the shortest distance, where the satellite is above the transmitter $(\zeta = 0°)$.

Fig. 2.9 shows that the maximum coherence diameter we expect in a relatively normal condition for which $A_0 = 1.7 \times 10^{-14} m^{-\frac{2}{3}}$, is 8.5 cm, while at $60°$ it decreases to 5.8 cm. Clearly, bad weather condition can reduce it significantly. The Fried's parameter can be calculated at different conditions by considering the nominal value of the atmosphere

structure parameter on the ground (A_0) and using it in Eq. 2.3.

As mentioned in Sec. 2.1.4 and 2.1.3, if the beam waist is smaller than r_0 the spot is diffraction limited and log normal statistics with unity mean value is observed, at this region Strehl ratio is at maximum. However, when the beam waist is roughly as big as r_0 the image gets focused and contains the highest intensity on the optical axis, so Strehl ratio still remains about 1. Once the beam radius gets larger than Fried parameter, the beam breaks up, so the on-axis intensity falls down noticeably. As a result on-axis Strehl ratio goes to Zero. However, as discussed in Section 2.11, as long as the detectors receive the required intensity, the link can stay strong and stable. Therefore, having speckles of light is not an issue for QKD purposes. Hence, we consider the radius of the beam, leaving the telescope, to be the same or larger than the atmospheric coherence diameter, which is considered 8.5 cm at maximum. However, if the beam diameter is much larger than r_0, ($2W_0/r_0 \gg 1$), roughly speaking, the pointing error can be ignored, as seen and discussed in Section 2.1.5.

Furthermore, enlarging the telescope aperture is not always effective in reducing the atmosphere impacts on the beam, see 2.1.6. Beam diffraction determines the base line of the link attenuation. Therefore, after a certain aperture size, making it larger does not help with reducing the loss. Once the optimal aperture size is determined and satisfies the conditions mentioned above, one can choose the effective lens size for a desired transmitter.

In Fig. 2.10, Eq. 2.15 is plotted for a receiver with a 30 cm aperture. The plot shows the link attenuation for different diameters of the transmitter aperture, at 0° to 60° zenith angles. It indicates that the asymptotic loss of a channel at 0° zenith angle is 35.5 dB and after $2W_0 = 25$ cm, link attenuation varies less than 1 dB for larger apertures. Therefore, $2W_0 = 25$ cm can be considered as the minimum diameter, beyond which enlarging the aperture is no longer beneficial. Nevertheless, manufacturing costs must be taken into consideration. As lens get larger, the number of the manufacturers capable of building the lens reduces. As a result, the price increases significantly. Considering manufacturing costs, we found that changing the lens size from 10 inch (25.4 cm) to 8 inch (20.32 cm), is optimal for both performance of the lens and the price. An 8 inch aperture has only 0.3 dB more attenuation than a 10 inch, but it reduces the costs remarkably. However, the price was still varying between 14,000 USD to 70,000 USD. So careful optimizations are required to control the cost drivers such as surface specifications, which are discussed in Chapter 3.

(a)

(b)
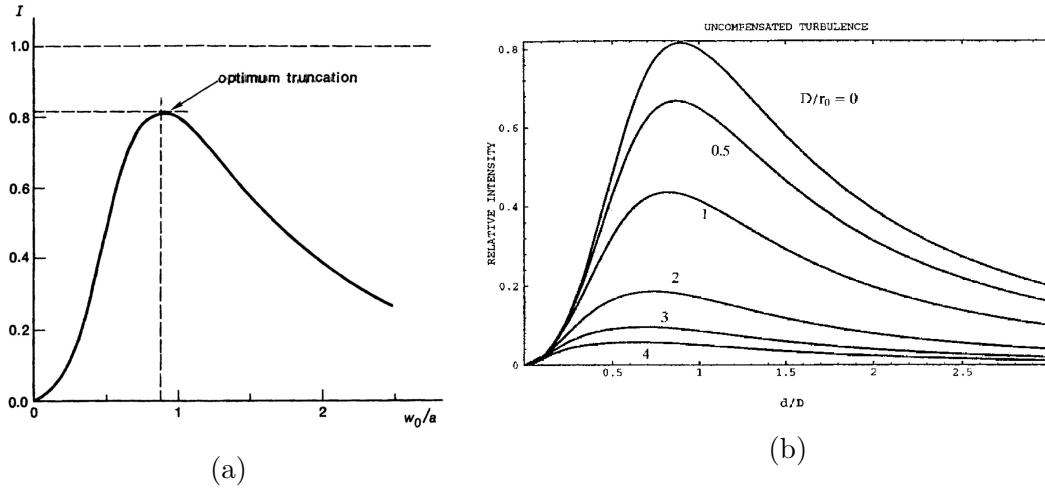
Figure 2.11: (a) The maximum far-field on-axis intensity is achieved at $W_0/a \approx 0.89$. W and a are respectively the beam and aperture radii. [76] (b) far-field on-axis intensity versus different ratio of $2W_0$ to transmitter aperture, in presence of turbulence. The maximum intensity occurs at $2W_0 < 0.89D_T$. $d = 2W_0$, where W_0 is $1/e^2$ beam radius. [95]

Optimal Coupling of Gaussian Beam to the Telescope

One assumption for transmitter aperture is considering $D_T = 2W_0$, that suggests having a Gaussian beam truncated at its $1/e^2$ diameter by the aperture. Nonetheless, $D_T^2 = 8W_0^2$ has been used by many authors [43][42][15]. Here we discuss the best ratio of the transmitter aperture and the Gaussian beam width.

Anthony E. Siegman in his "Lasers" book [76], investigates a truncated Gaussian beam going through a circular aperture. He reviews aperture diffraction and far-field beam properties to define the optimum transmitter diameter for the maximum on-axis intensity. By increasing the beam width to fill the aperture, far-field angular spread reduces and beyond a certain number, the total power also decreases, since the beam is cropped by a fixed circular aperture.

The intensity of a Guassian beam near/on the optical axis (z) for a near and far-field is defined as:

$$I(r, z) \approx [\frac{W_0}{W(z)}]^2 \times |1 - \delta_a e^{-j\pi N} J_0(2\pi N r/a)|^2 \qquad (r \ll a), \qquad (2.17)$$

29

Where $\delta_a \equiv e^{-a^2/W_0^2}$ represents the wave amplitude at the edge of the beam that is cut off by the aperture. So $\delta_a \leq 1$ and $\delta_a = 1$ corresponds to a uniform plane wave at the aperture. a is the aperture radius, while N and $J_0(r)$ are related to Bessel function defining a Gaussian beam. Siegman plotted far-field on-axis intensity over different ratios of beam radius (W_0) and aperture radius (a). He concluded that the maximum on-axis intensity happens at $W_0/a \approx 0.89$ and the maximum intensity is $\approx 81\%$ of the total power (Fig. 2.11a). In other words, the aperture of the transmitter must be 2.247 times of the $1/e^2$ beam waist.

Later, H. T. Yura studied the optimal truncation and presented a precise analytic approximation for a far-field beam irradiance distribution [95]. He expanded his analysis to the propagation of a beam in presence of turbulence. As mentioned in Section 2.1.3 if $W_0/r_0 \gg 1$, the Strehl ratio drops rapidly by increasing the aperture size. Therefore, there is a trade off between fulfilling $2W_0/D_T \approx 0.89$ which mitigates truncation effects, and $2W_0 \to 0$ which maximizes the Strehl ratio. Since the Strehl ratio of $2W_0 < 0.89D_T$ is larger than the Strehl ratio of $2W_0 > 0.89D_T$, the optimal ratio in presence of turbulence must be $2W_0 < 0.89D_T$. Figure 2.11b compares on-axis intensity over $2W_0/D_T$ for different D/r_0 values [95]. To satisfy the conditions mentioned above, it is customary to consider the ratio of a *Soft Aperture*, Gaussian beam width, and a *Hard Aperture*, opening of the transmitter as below [43].

$$D_T^2 = 8W_0^2, \tag{2.18}$$

For completeness we note that, J-P Bourgoin *et al.* [9] suggested that the beam FWHM must be the same as the transmitter diameter for a WCP source (since the intensity losses due to clipping can be compensated), and half the transmitter diameter for an entangled photon source. By plugging $2W_0 = (1.699\ \text{FWHM})$, into Eq. 2.18, we obtain that FWHM is about 0.7 of the transmitter diameter (as opposed to $2W_0/D_T \approx 0.89$). Thus, Eq. 2.18 can be considered as an optimal relation for both photon sources.

Ground Telescope Acquisition, Pointing and Tracking System

In free-space communication, the transmitter needs to track the receiver successfully, to create a quantum channel. Thus, Acquisition, Pointing and Tracking (APT) system is used for this purpose. The APT acts as an optical fine pointing system, whereas the telemetry data and telescope mount alignment do the coarse pointing. The Ground station APT collects the beacon light at 980 nm or 1550 nm from the satellite and uses a Fast Steering Mirror (FSM) to guide the quantum signal at 785 nm, towards the receiver. Fig. 2.12 illustrates our current transmitter APT [63].
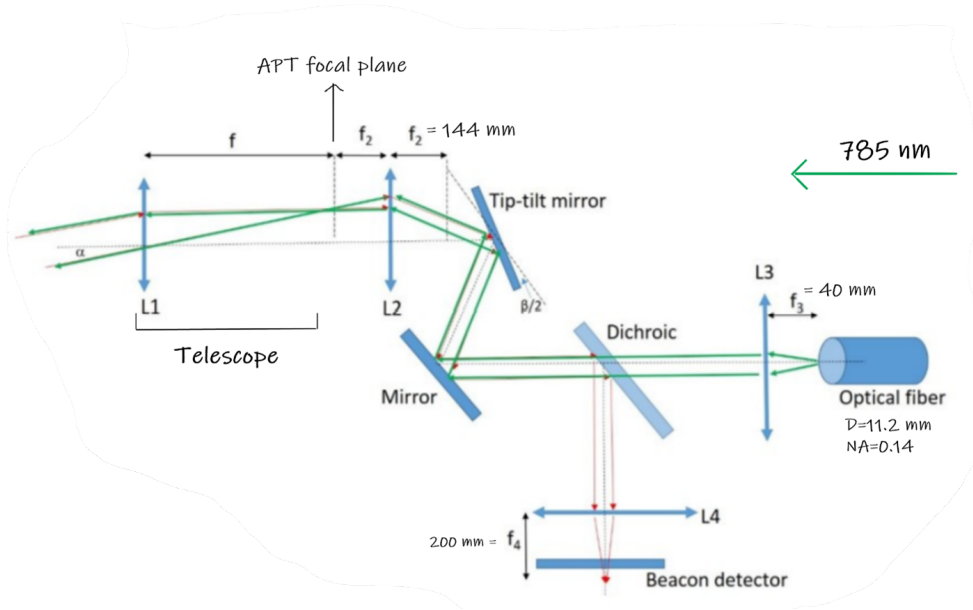
Figure 2.12: Ground telescope APT. A lens (L2) at the entrance of APT, collimates the beacon light received from the satellite (red line). After reflecting from the folding mirrors, a dichroic mirror separates the two wavelength and the beacon light gets focused on a detector. One of the folding mirrors does small angular deflections to align the two signals. Beacon signal and Quantum signal propagate in opposite directions.[63]

One criteria not considered in the previous sections was whether the current APT system is capable of being optimally used with the new telescope. We determined the size of the lens to be 8 inch (20.32 cm) and by accepting Eq. 2.18, the beam waist (W_0) at the aperture is obtained as 7.18 cm. Therefore, the signal generated by the APT, must have the correct magnification to result in a beam at the telescope aperture with a radius of 7.18 cm. Thus by taking the mode field diameter of the optical fibre used for the quantum signal can be assumed to be $1/e^2$ the width of a Gaussian beam. Then,

$$\text{Airy Disk Radius} = 1.22\lambda N, \tag{2.19}$$

and,

$$\text{f-Number}: N = \frac{f}{D} \approx \frac{1}{2NA}. \tag{2.20}$$

With NA= 0.14 of the fibre, the spot radius is calculated as:

31

$$1.22 \times 785nm \times \frac{1}{2 \times 0.14} = 3.68\mu m. \tag{2.21}$$

The 3.68 μm spot gets magnified by the L2 and L3 lenses, 3.68 μm $\times$ (144/40)= 13.24 μm and results in a focused beam, with beam waist of 13.24 μm at the focal plane of the APT collimating lens and the telescope. Now considering the Gaussian beam expressions Eq. 2.22, a 13.24 μm beam radius at the focal plane of the telescope corresponds to a 4.6 cm beam waist at the aperture.

$$\begin{aligned} W(z) &= W_0\sqrt{1 + (\frac{z}{z_R})^2} \\ z_R &= \frac{\pi W_0^2 n}{\lambda} \end{aligned} \tag{2.22}$$

However, as mentioned before, the goal is to attain a beam with W_0 =7.18 cm. Therefore, the current APT needs modifications to match the new transmitter telescope. According to Eq. 2.22, a 7.18 cm beam waist at the aperture requires a spot with a radius of 8.48 μm at the focal plane of the telescope and APT. Therefore, the focal length of the collimating lens (L2) must be reduced to 92.23 mm.

$$L2 = \frac{144mm}{13.24\mu m} \times 8.48\mu m = 92.23mm \tag{2.23}$$

Modifying the APT to have the right beam size and higher performance is the future work of the group. New coating design for the mirrors to preserve the polarization at 785 nm and have high reflectivity at 980 nm and 1550 nm, a better coating for the dichroic mirror to increase the transmission at 785 nm and reflection at 980 nm and 1550 and a new collimating lens to correct the spot size are some examples of the modifications required for the current APT. Moreover, according to the manufacturer, since designing the dichroic mirror specifically for the mentioned wavelengths is challenging, we are investigating other approaches to replace the dichroic with another optical element that can separate the signals while having high transmission/reflection.

2.3 Conclusion

The impacts of the atmospheric turbulence on a propagating Gaussian beam is reviewed in this chapter to obtain the optimal aperture size required for our new ground station.

According to the chosen wavelength and satellite specifications of our uplink experiment, minimum link attenuation is calculated as 35.5 dB and the effective transmitter aperture is derived as 25 cm. Considering the fabrication costs and less than 1 dB change for a 5 cm smaller aperture, we concluded choosing a 20.32 cm (8 inch) lens. So far, we have a good understanding of the link attenuation in an uplink configuration, however link analysis considering the fibre coupling efficiencies and other optical imperfections for a downlink requires more analysis.

Furthermore, discussed the truncation of a Gaussian beam to achieve the highest intensity at far field. As a result, $D_T^2 = 8W_0^2$ is considered to estimate the Gaussian beam size at the focal point of the telescope and modify our current tracking system. The ground station APT collimating lens, requires 51.77 mm shorter focal length to meet the required conditions. Correcting the APT system for the new transmitter and modifying its structure to be more mechanically stable is for future work.

Chapter 3

Optics Design
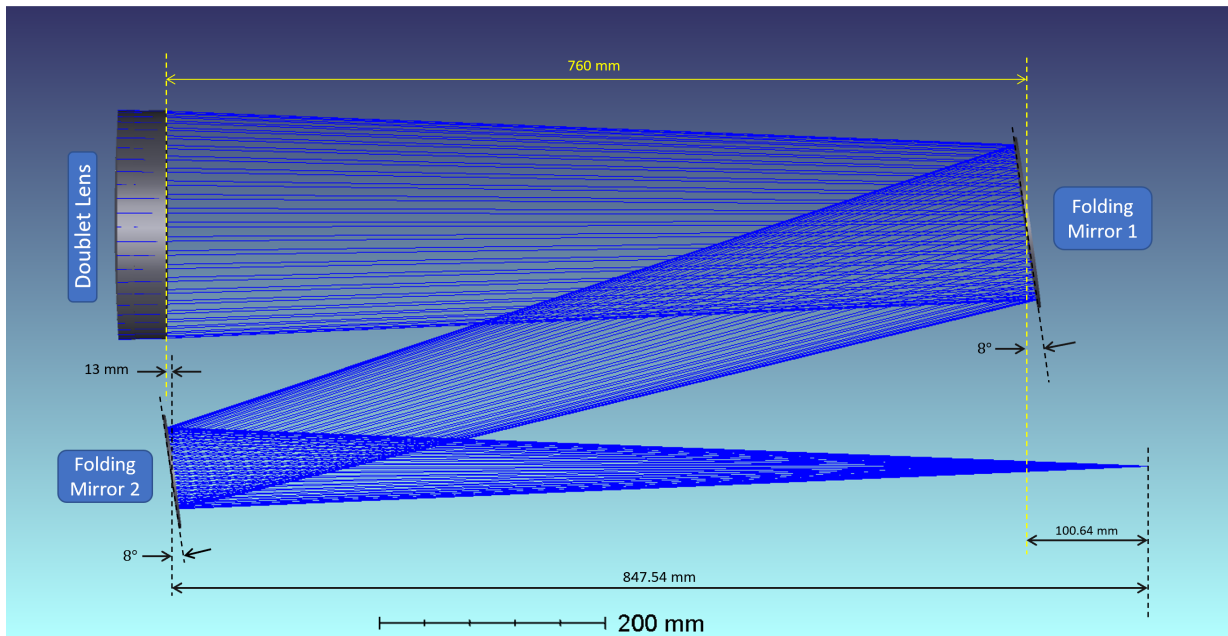
Figure 3.1: Configuration of the doublet lens and folding mirrors, designed in Zemax.

Designing a customized lens that is compatible with QKD requirements, is a major component of this thesis. In chapter 2, we calculated the aperture size of the transmitter according to the link loss in a ground to space channel. This resulted in the requirement for a lens with a minimum diameter of 8-inch (203.2 mm), that is also corrected for the

desired wavelengths. The convenient way of getting the lens is always going with off-the-shelf options. However, there were several constraints needed to be considered in this work. Commercial refractive telescopes typically have smaller apertures and larger fields of view, whereas reflective telescopes can be found in various diameters including 8-inch and even larger [1]. In addition, commercial lenses are usually designed and optimized for visible wavelengths, which results in noticeable wavefront distortion at our desired wavelengths. Also, customized and specialized optic instruments that have high variety of coatings and designs, are mostly manufactured in smaller diameters to be used in research labs. As a consequence, there was a need for us to design and optimize the lens specifically for this project, to achieve the expected performance.

In this chapter, we study the distortions that happen to an image, due to the imperfections of the lens and discuss the methods that correct them. Finally, by taking theses parameters into account, we present our custom-designed lens and determine the surface specifications based on far-field beam modeling. We simulated atmospheric turbulence and lens imperfections as a hologram to observe their impacts on a detected beam at the satellite, which also helped us to avoid unnecessary procedures in the fabrication.

---

[1] High quality lenses are made of blocks of different materials, which are not always in large dimensions. To build a big lens out of a certain glass, it might be needed to reshape the blocks to reduce the thickness and increase the surface area, which can cause major impurities in the glass. However, mirrors are built via deposition of different layers on a substrate. So it allows to have desired large pieces depending on the manufacturing company capability.
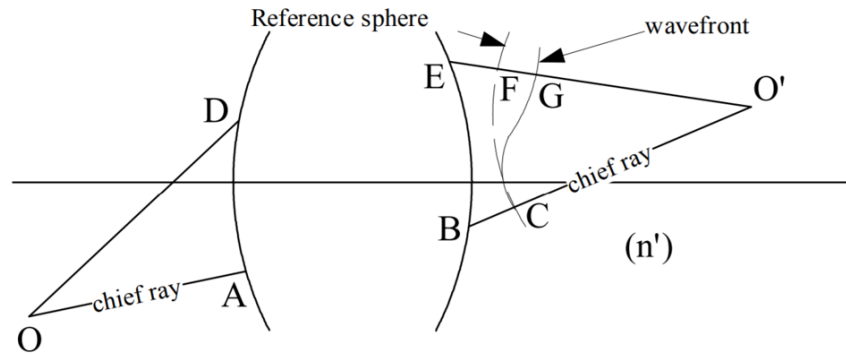
Figure 3.2: Wavefront Aberration; FG shows the optical path difference between the reference sphere and the distorted wavefront [37].

3.1 Wavefront Aberration

Fig. 3.2 illustrates two rays going through the lens and forming an image at O'. Due to the properties of the lens, GC wavefront is observed on the other side, instead of FC which is the reference sphere that the beam had to follow if there was no distortion. Hence, FG shows the path difference between the distorted wavefront and the reference sphere. This length multiplied by the index of refraction of the image space (n') is known as the wavefront aberration or optical path difference (OPD) of the beam. Wavefront aberration appears in several forms such as defocus, coma, astigmatism, chromatic aberration and etc. Polynomials can be used to describe the wavefront properties, specifically Zernike polynomials that have the same forms as the aberrations [37][93]. These polynomials are discussed in the following section.

Radial degree (n)	Azimuthal frequency (m)					
	0	1	2	3	4	5
0	$Z_1 = 1$ Constant					
1		$Z_2 = 2r\cos\theta$ $Z_3 = 2r\sin\theta$ Tilts (Lateral position)				
2	$Z_4 = \sqrt{3}(2r^2 - 1)$ Defocus (Longitudinal position)		$Z_5 = \sqrt{6}\,r^2\sin2\theta$ $Z_6 = \sqrt{6}\,r^2\cos2\theta$ Astigmatism (3rd Order)			
3		$Z_7 = \sqrt{8}(3r^3 - 2r)\sin\theta$ $Z_8 = \sqrt{8}(3r^3 - 2r)\cos\theta$ Coma (3rd order)		$Z_9 = \sqrt{8}\,r^3\sin3\theta$ $Z_{10} = \sqrt{8}\,r^3\cos3\theta$		
4	$Z_{11} = \sqrt{5}(6r^4 - 6r^2 + 1)$ 3rd order spherical		$Z_{12} = \sqrt{10}(4r^4 - 3r^2)\cos2\theta$ $Z_{13} = \sqrt{10}(4r^4 - 3r^2)\sin2\theta$		$Z_{14} = \sqrt{10}\,r^4\cos4\theta$ $Z_{15} = \sqrt{10}\,r^4\sin4\theta$	
5		$Z_{16} = \sqrt{12}(10r^5 - 12r^3 + 3r)\cos\theta$ $Z_{17} = \sqrt{12}(10r^5 - 12r^3 + 3r)\sin\theta$		$Z_{18} = \sqrt{12}(5r^5 - 4r^3)\cos3\theta$ $Z_{19} = \sqrt{12}(5r^5 - 4r^3)\sin3\theta$		$Z_{20} = \sqrt{12}\,r^5\cos5\theta$ $Z_{21} = \sqrt{12}\,r^5\sin5\theta$
6	$Z_{22} = \sqrt{7}(20r^6 - 30r^4 + 12r^2 - 1)$ 5th order spherical		Z_{23} Z_{24}		Z_{25} Z_{26}	

Figure 3.3: Zernike polynomials generated from Eq. 3.1 (ρ and θ' are replaced with r and θ in this table). Each term of the polynomial describes an optical aberration. [55]

3.1.1 Zernike Polynomials

Zernike polynomials are infinite complete sets that are defined on two orthogonal real bases (ρ, θ) over a continuous space inside a unit circle:

$$Z_n^m(\rho, \theta) = \sqrt{2(n+1)} R_n^m(\rho) e^{im\theta}, \tag{3.1}$$

$$Z_n^m(\rho, \theta) = U_{nm}(\rho, \theta) + iV_{nm}(\rho, \theta), \tag{3.2}$$

Where, $n \geqslant |m|$, $n \geqslant 0$, $n - m$ is even and U_{nm} and V_{nm} are defined as,

$$U_{nm}(\rho, \theta) = \sqrt{2(n+1)} R_n^m(\rho) \cos(m\theta), \tag{3.3}$$

$$V_{nm}(\rho, \theta) = \sqrt{2(n+1)} R_n^m(\rho) \sin(m\theta). \tag{3.4}$$

Any functions such as $\phi(\rho, \theta)$ can be defined as a linear sum of U_{nm} and V_{nm} with arbitrary weighting of coefficients A_{nm} and B_{nm}, due to the orthogonality of these polynomials.

$$\phi(\rho, \theta) = \sum_{n=0}^{\infty} \sum_{m=0}^{n} [A_{nm} U_{nm}(\rho, \theta) + B_{nm} V_{nm}(\rho, \theta)]. \tag{3.5}$$

37

This function can be used either for expressing surfaces with constant phase across a wavefront or only a phase mask to change the wavefront based on the specifications of the optical components or the impacts of the perturbed environment that the beam is propagating through.

Below are some interesting and important properties of the polynomials [93]:

1. Due to rotational symmetry, it can be expressed as $R(\rho)G(\theta')$, where $G(\theta')$ represents a continuous periodic function that repeats every 2π. So, if the system rotates with an angle of α, the polynomial doesn't change. This, allows to define $G(\theta' + \alpha)$ as,

$$G(\theta' + \alpha) = e^{\pm im\theta'}, \; m \geq 0 \tag{3.6}$$

2. The radial part must be defined such that $R(\rho) \propto \rho^n$ for all $n > m$.

3. If m is even (odd) then $R(\rho)$ must be even (odd).

Considering the second and third conditions, the radial part can be written as a special case of Jacobi polynomials and must satisfy the orthogonality and normalization:

$$\int_0^1 R_n^m(\rho)R_{n'}^m(\rho)\rho \, d\rho = \frac{1}{2(n+1)}\delta_{nn'}. \tag{3.7}$$

Assuming that $R_n^m(1) = 1$, the radial polynomial can be rewritten as $R_{2n-m}^m(\rho) = Q_n^m(\rho)\rho^m$, where $Q_n^m(\rho)$ is:

$$Q_n^m(\rho) = \sum_{s=0}^{n-m}(-1)^s\frac{(2n-m-s)!}{s!(n-s)!(n-m-s)!}\rho^{2(n-m-s)}. \tag{3.8}$$

Finally, the equation for wavefront OPD is derived as[93] :

$$W = \overline{\Delta W} + \sum_{n=1}^{\infty}\left[A_nQ_n^0(\rho) + \sum_{m=1}^{n}Q_n^m(\rho)\rho^m(B_{nm}\cos m\theta' + C_{nm}\sin m\theta')\right], \tag{3.9}$$

where $\overline{\Delta W}$ is the mean OPD and A_n, B_{nm}, C_{nm} are the polynomial coefficients. Fig. 3.3 shows 36 terms of Zernike polynomials. Each term represents either one or a combination of different aberrations.

38

To write the power series defining the wavefront by adding all of these terms together, it is more convenient to use Hopkin's notation [37]. This notation uses η', r, ϕ, where η' is the image height on the image plane and r and ϕ describe the ray intersection with the exit pupil plane in polar coordinate (Fig. 3.4). By accepting the rotational symmetry about the z axis (beam propagation direction), without loss of generality, it can be assumed that all images fall along η'. Therefore the aberration observed in the image is directly related to η', r and $\eta' r \cos \phi$ (more details provided in Chapter 4 of [37]). Hopkin's notation suggests writing each term of the polynomial in form of $_i w_{jk} \eta'^i r^j \cos^k \phi$, which has the advantage of identifying the aberration with only the suffixes. These power series can be rewritten as below [37]:

$$
\begin{aligned}
W = {}& _0w_{20}r^2 \quad \text{Defocus} \\
& + {}_1w_{11}\eta r \cos\phi \quad \text{Change in scale} \\
& + {}_2w_{00}\eta^2 \\
& + {}_0w_{40}r^4 \quad \text{Spherical aberration} \\
& + {}_1w_{31}\eta r^3 \cos\phi \quad \text{Coma} \\
& + {}_2w_{22}\eta^2 r^2 \cos^2\phi \quad \text{Astigmatism} \\
& + {}_2w_{20}\eta^2 r^2 \quad \text{Field curvature} \\
& + {}_3w_{11}\eta^3 r \cos\phi \quad \text{Distortion} \\
& + {}_4w_{00}\eta^4 \\
& + {}_0w_{60}r^6 \quad \text{Spherical aberration} \\
& + \ etc.
\end{aligned}
\tag{3.10}
$$

3.1.2 Seidel Aberrations

Describing the image plane by two orthogonal axes of $\eta'\ \xi'$, and the exit pupil plane by x and y, the aberration of the image is defined by $\delta\eta'$ and $\delta\xi'$, which are related to the change of wavefront in x- and y-directions, and $\delta U'$, the angle that the aberrated ray makes with the reference sphere radius. Hopkin defined y_{rel} and x_{rel} for these equations that represent the relative pupil coordinates that vary from -1 to +1.
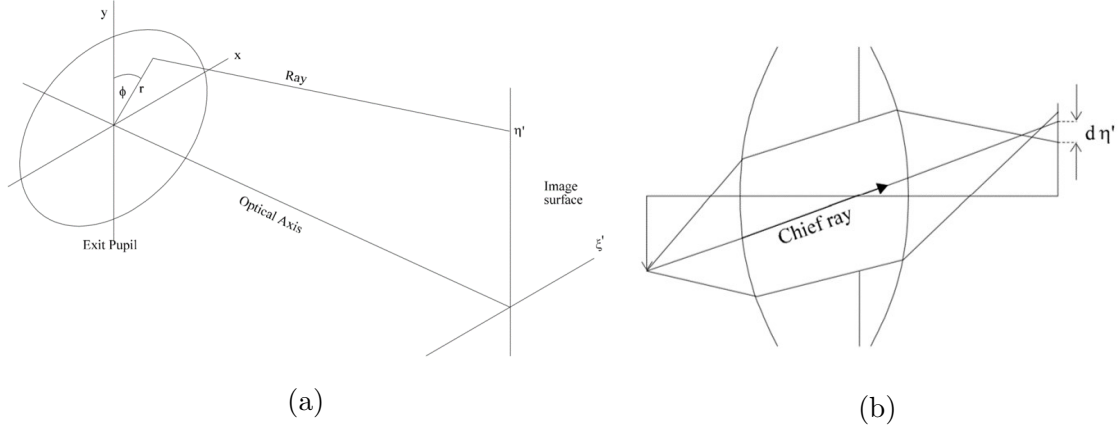
Figure 3.4: (a) Aberration coordinate; Image is always along η' due to the symmetry of the lens about the z axis (beam propagation direction). r and ϕ define the intersection of the ray with exit pupil plane in polar coordinates. (b) $\delta\eta$ indicates the y-component of the aberrated transverse ray in image space. [37]

$$
\begin{aligned}
\delta\eta' &= -\frac{-1}{n'\sin U'}\frac{\partial W}{\partial y_{rel}}, \\
\delta\xi' &= -\frac{-1}{n'\sin U'}\frac{\partial W}{\partial x_{rel}}.
\end{aligned}
\tag{3.11}
$$

By taking the derivative of each term of Eq. 3.10, the effect of each term of aberration on the image can be comprehended. Table 3.1 summarizes the results. For simplicity, r^2 and $r\cos\phi$ are replaced with (x^2+y^2) and y. Here, x and y are interpreted as the aperture size at the exit pupil and η indicates the field.

Defocus and *Lateral Image Shift* are considered as first-order aberrations since they are proportional to the second order of the aperture and field ($\delta\eta'$ is dependent on the first order of y and η.) The same explanation applies to the next five aberrations which are known as third-order aberrations. These 5 terms are called *Seidel Aberrations* that consists of *Spherical aberration, Coma, Astigmatism, Field Curvature* and *Distortion*.

(a)	(b)
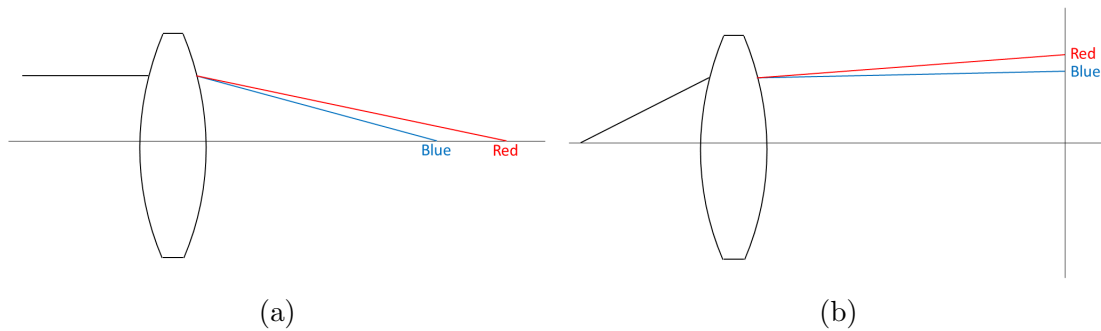
Figure 3.5: (a) axial color aberration; (b) lateral color aberration.

3.1.3 Chromatic Aberrations

Longitudinal Chromatic Aberration (Axial Color) and *Transverse Chromatic Aberration (Lateral Color)* occur when different wavelengths of a polychromatic light do not focus at one point. Axial color aberration can be seen as different focal points along the optical axis whereas, lateral color aberration is responsible for having different focal points with different heights on η' axis. As an example, comparing 2 wavelengths of red and blue, the focal point of blue ray falls before red on the optical axis and lower on the image plane due to its shorter wavelength (Fig. 3.5).

Optical Aberrations				
Aberration	**Wavefront term**	$\delta\eta' \propto$	$\delta\xi' \propto$	**properties**
Defocus	$_0w_{20}r^2 = {}_0w_{20}(x^2+y^2)$	2y	2x	The focus is changing along the optical axis. If the aberration terms have r^2, they can be related to the change of focus
Lateral image shift	$_1w_{11}\eta r\cos\phi = {}_1w_{11}\eta y$	η	0	Transverse ray aberration is Constant for a given η. It is responsible for the magnification of the image, since the rays intersect at points that are laterally shifted.
Spherical aberration	$_0w_{40}r^4 = {}_0w_{40}(x^2+y^2)^2$	y^3	x^3	This term is independent of η and ϕ. The wavefront aberration is proportional to r^4 which creates a spot with either brighter center or brighter outer rings, depending on the position of the image plane on the optical axis.
Coma	$_1w_{31}\eta r^3\cos\phi = {}_1w_{31}\eta(x^2+y^2)y$	$\eta(x^2+3y^2)$	$2\eta yx$	The rays going through the outer parts of the lens focus at different heights comparing to the chief ray and make a spot like a water drop.
Astigmatism	$_2w_{22}\eta^2 r^2\cos^2\phi = {}_2w_{22}\eta^2 y^2$	$2\eta^2 y$	0	Astigmatism creates a cylindrical defocus, since it only affects the tangential section. In other words, tangential focal line does not intersect the sagittal one
field curvature	$_2w_{20}\eta^2 r^2 = {}_2w_{20}\eta^2(x^2+y^2)$	$2\eta^2 y$	$2\eta^2 x$	It is a defocus that is proportional to the second order of field angle (η^2). So the image of a flat object focuses on a curved plane instead of having a flat one.
Distortion	$_3w_{11}\eta^3 r\cos\phi = {}_3w_{11}\eta^3 y$	η^3	0	Distortion is the lateral image displacement which can be observed at the edges of the image. It is proportional to third order of field angle but it is common to be defined as $\frac{\delta\eta'}{\eta'}$ to be expressed as terms of η'^2.

Table 3.1: Optical aberrations for a monochromatic beam [37]
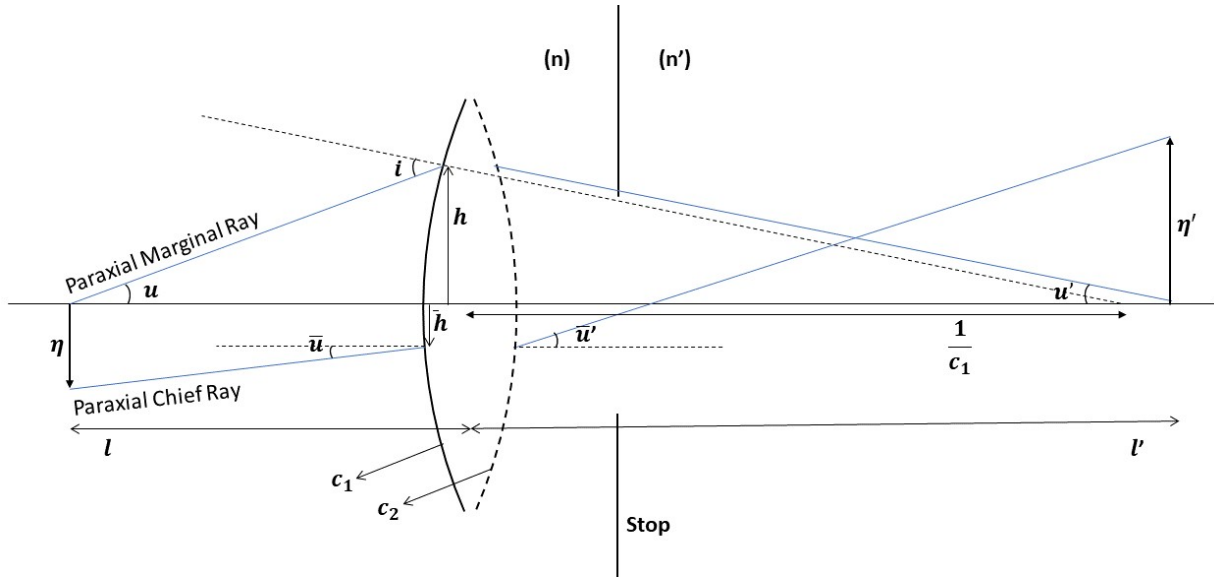
Figure 3.6: Paraxial rays going through a thin lens, from an object (η) on the left.

c_1 , c_2	Curvature of the lens
B	Shape factor: $B = \frac{c_1+c_2}{c_1-c_2}$
H	Lagrange Invariant: $H = nu\eta = n'u'\eta'$
A	Refraction Invariant: $A = ni = n'i'$
E	The eccentricity: $HE = \frac{\bar{h}}{h}$
K	Power of the lens: $K = K_1+K_2-\frac{dK_1K_2}{n'_1}$ where $K_1 = (n-1)c_1, K_2 = -(n-1)c_2$; d and n'_1 represent the thickness and index of refraction of the lens.
C	Conjugate factor: $C = \frac{m+1}{m-1}$ where, m is the transverse magnification.
V	Abbe V-number: $V = \frac{n-1}{\delta n}$ where n is the refractive index of the glass and δn indicates the dispersion.

Table 3.2: Optical parameters of a lens.

3.1.4   Lens Design and Correction

In order to design a lens and correct it for aberrations, it is important to know how these terms are related to the structural parameters of a lens, such as shape factor, radius of

43

curvature, index of refraction and etc. Therefore, instead of using the Zernike polynomials, the optical path difference of an aberrated wavefront relative to the reference sphere can be derived geometrically for each aberration form Fig. 3.6 based on the optical parameters. Eq. 3.12 to Eq. 3.18 represent coma, astigmatism, field curvature, distortion, axial color and lateral color aberrations respectively, that ideally must be zero to have aberration free image. In this approach, u and u' are the angles of a paraxial marginal ray [2] with the optical axis for the object and the image respectively. h is the height of the point the the marginal ray enters the lens to the optical axis. $\overline{u}$, $\overline{u'}$ and $\overline{h}$ are related to a paraxial chief ray [3] [37].

Spherical Aberration:

$$S_1 = \frac{h^4 K^3}{4} \left[\frac{n^2}{(n-1)^2} + \frac{n+2}{n(n-1)^2} (B + \frac{2(n^2-1)C}{n+2})^2 - \frac{nC^2}{n+2} \right]. \tag{3.12}$$

Coma:

$$S_2 = -\frac{h^2 K^2 H}{2} \left[\frac{(n+1)B}{n(n-1)} + \frac{(2n+1)C}{n} \right]. \tag{3.13}$$

Astigmatism :

$$S_3 = H^2 K. \tag{3.14}$$

Field Curvature:

$$S_4 = H^2 \frac{K}{n}. \tag{3.15}$$

Distortion:

$$S_5 = \frac{\overline{A}}{A}(S_3 + S_4). \tag{3.16}$$

Axial color:

$$C_1 = h^2 \frac{H}{V}. \tag{3.17}$$

Lateral color:

$$C_2 = \overline{A} h \delta(\frac{\delta n}{n}). \tag{3.18}$$

To obtain a corrected lens, the specifications of the lens must be chosen carefully, so that all the above terms are minimized. The first step in designing, is being aware of the

---

[2] Marginal ray goes from the the center of the object and passes at the maximum aperture of the lens.
[3] A chief ray is from an off-axis point of the object that goes through the center of the lens.

existing degrees of freedom and the wavelengths at which the lens needs to be To start designing a lens, it is crucial to be aware of the lens variables that can be changed and the desired wavelengths that the lens must be corrected for. According to Eq. 3.12 to Eq. 3.18, three variables given in Table 3.2 affect the aberrations noticeably and should be chosen carefully: 1. Material of the lens (indicated by the Abbe V-number) 2. K power of the lens (important in all 5 Seidel aberrations) 3. B the shape of the lens (affects Spherical aberration and Coma).

Correction of Distortion and Lateral Color Aberration

First aberrations that can be corrected are distortion and lateral color. Lateral color shift is a result of having separate focal points for different wavelengths at different heights relative to the optical axis. While, distortion is interpreted as a lateral image displacement that is proportional to the third power of the field angle. Therefore, a solution to eliminate these aberrations is limiting the rays to the region between marginal rays which occurs by adding an aperture stop at the surface of the lens. This can be shown using Eq. 3.16 and 3.18, which are dependent on $\overline{A}$ (Refraction invariant of a chief ray). This term is defined as,

$$\overline{A} = \frac{H}{h}(AhE - 1), \tag{3.19}$$

where E implies the distance between the surface and the aperture stop. So by having the stop at the lens surface, E equals zero and $\overline{A}$ is obtained as,

$$\overline{A} = \frac{H}{h}. \tag{3.20}$$

Then, by plugging it into Eq. 3.16 and 3.18 and accounting for effects at both surfaces of the lens, distortion and lateral color go to zero. The proof is as below [37].

- Distortion:

  S_3 and S_4 can be rewritten as,

$$S_3 = -\overline{A}^2 h\delta(\frac{u}{n}),$$
$$S_4 = -H^2 c\delta(\frac{1}{n}). \tag{3.21}$$

  substituting these terms in Eq. 3.16, the distortion of a single surface is derived as,

$$S_5 = \frac{\overline{A}}{A}(-H^2\frac{\delta(\frac{u}{n})}{h} - H^2 c\delta(\frac{1}{n})) = \frac{\overline{A}}{A}(\frac{AH^2}{h}(\frac{1}{n^2} - \frac{1}{n'^2})). \tag{3.22}$$

45

Then, considering both surfaces we get,

$$S_5 = \frac{H^3}{h^2}(1 - \frac{1}{n^2} + \frac{1}{n^2} - 1) = 0. \tag{3.23}$$

- Lateral Color:

  By plugging Eq. 3.20 into Eq. 3.18, the lateral color of a thin lens (considering both surfaces), with an aperture stop at the surface is obtained zero:

$$C_2 = -H\delta(\frac{\delta n}{n}) = -H[(\frac{\delta n}{n})_1 + (\frac{\delta n}{n})_2] = 0. \tag{3.24}$$

Correction of Axial Color Aberration

Axial color aberration (also known as chromatic aberration) can be mitigated using a doublet lens instead of a singlet, provided the aperture is relatively small (up to $f/4$) and the field angle is not larger than a few degrees. As light goes through a convex lens, due to the dispersion of light, different wavelengths focus at different spots along the optical axis. The Sellmeier equation describes the change in index of refraction of a medium as a function of the wavelength of the light [78][68].

$$n^2(\lambda) = 1 + \Sigma_i \frac{B_i \lambda^2}{\lambda^2 C_i}, \tag{3.25}$$

Where B_i and C_i are Sellmeier coefficients.

For instance, a longer wavelength has a smaller index of refraction which results in a longer focal length and a smaller power. Therefore, the focal point of the blue light falls behind that of the red light (This is called primary spectrum). Using two lens elements with opposite power signs, one can fix the chromatic aberration. The first element must have low dispersion and positive power which is called *Crown glass*, and the second element must have high dispersion and negative power, known as *Flint glass*. If we consider the power of a thin lens as $K = \frac{1}{f} = (1 - n)(c_1 - c_2)$, the variation of power for 2 different wavelengths is expressed as:

$$\delta K = K \frac{\delta n}{n - 1}, \tag{3.26}$$

$$V = \frac{n - 1}{\delta n}, \tag{3.27}$$

46

where δn is the dispersion of the lens and V is Abbe V-number that $1/V$ shows the variation of the focal lengths. To remove the chromatic aberration δK must be zero for two desired wavelengths,

$$\delta K = \frac{K_1}{V_1} + \frac{K_2}{V_2} = 0. \tag{3.28}$$

Furthermore, the total power is the summation of each element power $(K = K_1 + K_2)$. So K_1 and K_2 are derived as,

$$K_1 = \frac{KV_1}{V_1 - V_2}, \quad K_2 = -\frac{KV_2}{V_1 - V_2}. \tag{3.29}$$

As mentioned before, the powers must have opposite signs, which is also verified here.

So far the doublet is corrected for 2 wavelengths, for instance we consider the C and F lines of Helium[4]. However, since the refractive index curve as a function of wavelength is not linear, bringing the focal points of F and C together does not correct the focal points of all the wavelengths between them. For example, considering the d-line (which wavelength is almost in the middle of C and F), correcting C and F focal points results in a shorter focal length for d[5]. This is called the secondary spectrum of the lens. To correct the lens for the third wavelength as well, We need to rewrite Eq. 3.28 for F and d and take the relative partial dispersion into account.

$$\delta K_{d-F} = \frac{K_1}{V_{1_{d-F}}} + \frac{K_2}{V_{2_{d-F}}}, V_{d-F} = \frac{n_1 - 1}{n_F - n_d}. \tag{3.30}$$

So the relative partial dispersion can be expressed as,

$$p = \frac{n_F - n_d}{n_F - n_C} = \frac{V_{C-F}}{V_{d-F}}. \tag{3.31}$$

Hence, δK is derived based on the Abbe V-number and relative partial dispersion for C-F band of the materials used [37].

$$\delta K = K \frac{(p_1 - p_2)}{(V_1 - V_2)}. \tag{3.32}$$

---

[4]Refractive index at different bands of Helium varies for different materials that can be found in the datasheet of the glass, e.g., for BK7, n_c is 1.51432 at 656.3 nm and n_F is 1.52238 at 486.1 nm.

[5]For BK7, n_d is 1.51680 at 587.6 nm.

Finding the best material for which $p_1 = p_2$ results in having a lens corrected for all 3 desired wavelengths. This lens is called *Apochromatic*.

Doublet lenses can be either *Cemented* or *Air-Spaced*. The latter typically has higher performance. However, it has lower stability since they are fixed in a lens cell to keep the elements at a certain distance, and are thus more sensitive to any disturbance from the environment such as temperature variations. In addition, considering manufacturing, they require more effort and precision comparing to cemented doublets.

Correction of Field Curvature and Astigmatism

(a)

(b)

(c)
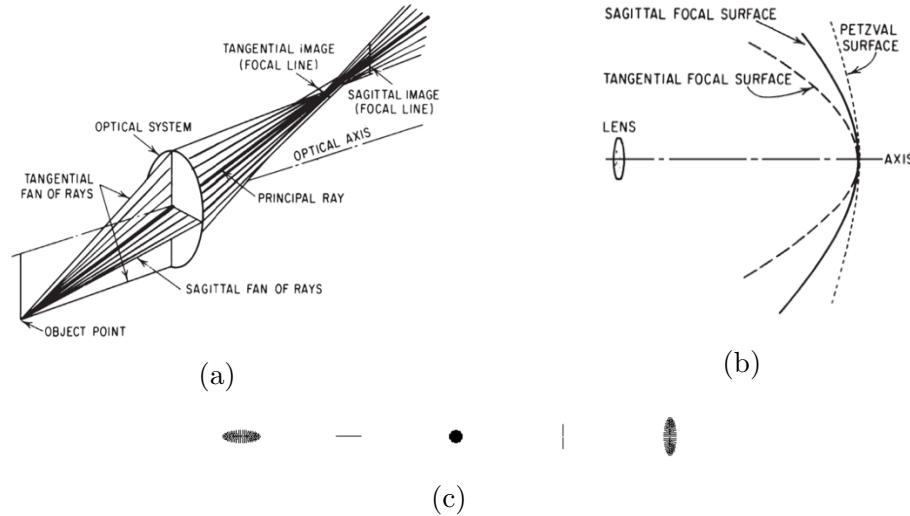
Figure 3.7: Illustration of a)Tangential and sagittal focal lines [78] b) Petzval surface, [78] and c) Spot diagram [37] in presence of astigmatism and field curvature

Two planes are considered for the rays coming from the object: Sagittal and Tangential. Both planes are along the optical axis but normal to each other (Fig. 3.7(a)). For an ideal lens with no astigmatism the rays coming from both planes coincide and form a point image. However, in presence of astigmatism, we observe separate focal lines for tangential and sagittal rays and the image between them gets blurry in a form of a circle or an oval (Fig. 3.7(c)). In addition, for a single lens the image plane is always a curved surface which is called Petzval and it contains the focal points of different field angles. In other words, Petzval curvature or field curvature indicates how much the image departures from a focal flat surface. In presence of astigmatism, the tangential image curve lies three times further

48
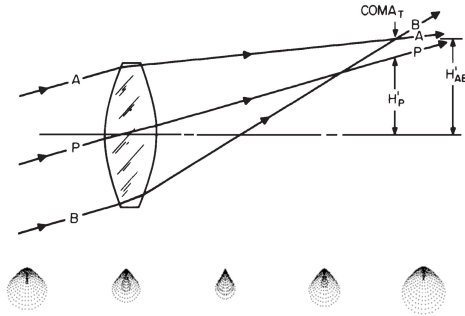
Figure 3.8: Spot diagrams of a focused beam with Coma aberration for different detector plane positions along the optical axis. [37][78]
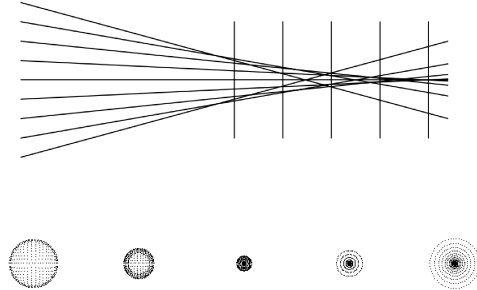
Figure 3.9: Spot diagrams of a converging beam with Spherical aberration, for different detector plane positions in and out of focus. [37]

away than the sagittal image surface to Petzval surface (Fig. 3.7(b)). To correct field curvature one should make use of a combination of lenses. In case of having an aperture stop at the lens, astigmatism and field curvature depend only on the power of the elements (Eq. 3.14 and Eq. 3.15). However since the power is already set to achieve zero chromatic aberration, these two terms can no longer be corrected. For an arbitrary stop which is not at the lens, $\delta S_3 = 2(H\delta E)S_2) + (H\delta E)^2 S_1$ holds and implies that astigmatism can be minimized by the introduction of Coma. Nevertheless, in order to correct S_1, S_2 and S_3 two lenses are required at a significant distance from each other. To correct the field curvature under these constraints, one can use techniques such as having 1.multiple lenses with different refractive indices, 2.separate lenses, or 3.a thick meniscus lens.

Correction of Spherical Aberration and Coma

Coma is the variation of the scaling across an aperture, which causes the image to look like a water drop (Fig. 3.8), while spherical aberration defines the variation of focusing. As a result, the rays from the edge of the lens focus before the ones near the optical axis [78]. Therefore, the image goes from a spot with a brighter outer ring to focus and then to a circle with brighter center (Fig. 3.9) [37]. Since the material and power has already been chosen, the only tool that can be used to correct these aberrations, is the shape factor. So Eq. 3.12 and Eq. 3.13 must be solved for $S_1 = 0$ and $S_2 = 0$. Using a doublet, gives us 4 surfaces for which we need to determine the radius of curvature. To preserve the focal length, we must keep one surface fixed. Also since we are considering a cemented

lens, the two touching surfaces are considered to have the same curvature, so in total 2 radii of curvature are available as variables. Fig. 3.10 shows the aberrations dependant on shape factor. As expected astigmatism and field of curvature are constant, so the goal is to find the intersection of coma, spherical aberration and the horizontal axis to obtain zero aberration for both. However, this might not be always feasible. In this case the material of the elements must be changed to minimize the aberration. It is important to repeat all the steps with the new materials to consider the optimized power for minimum axial color aberration.
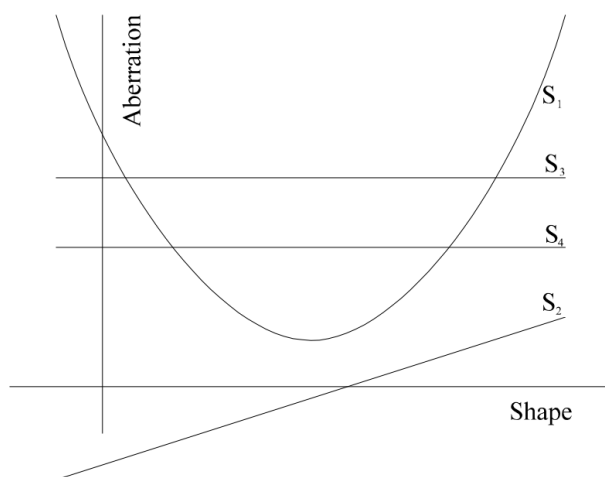
Figure 3.10: Dependency of Seidel aberrations of a thin lens on the shape factor. The lens is at the stop and S_3 (astigmatism) and S_4 (field curvature) are already determined, the shape factor must be selected such that it corresponds to the minimum aberration for both S_1 (spherical aberration) and S_2 (coma). An ideal material must have the point of intersection of S_1 and S_2 on the x axis to have obtain aberration. [37]

3.2   Lens Simulation

To design a lens specifically for a certain application one should solve the equations mentioned above and optimize the variables by ray tracing. However, solving by hand[6] can be tedious and that there are computation software that can expedite the process. In this

---

[6]In old-fashioned manual design, it is recommended to start with the closest existing model and optimize it by minimizing aberration equations and trying different materials. More details can be found in [78], Chapter 12.8.
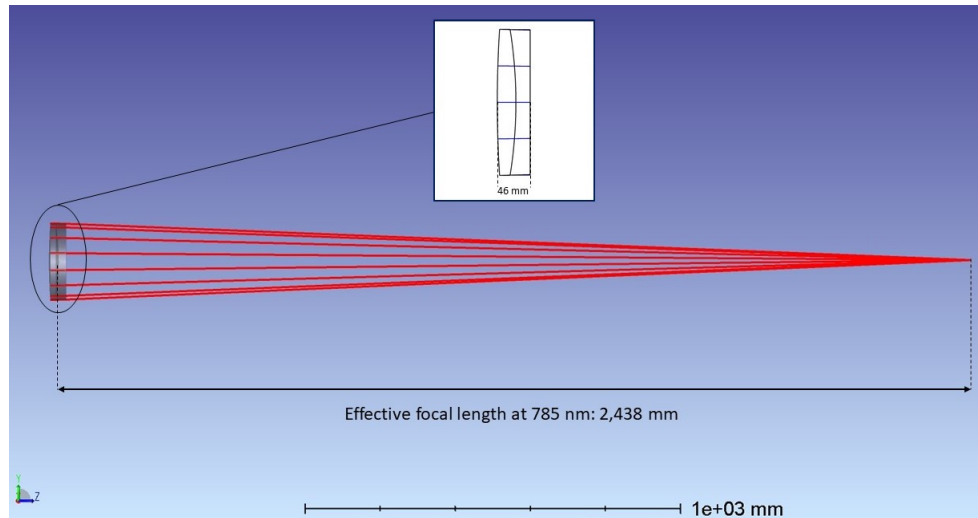
Figure 3.11: The 8-inch achromatic doublet design in Zemax. The custom-designed 8-inch lens is corrected to have minimum aberration at 785nm, 980nm, and 1550nm.

work, we used Zemax to design the lens and minimize the aberrations at desired wavelengths and field of view. Zemax OpticStudio is a powerful optical design software that is used for designing and analysing optical components based on applying the ray-tracing on multiple rays of a beam propagated through the optical system.

Here, we discuss designing the new lens of our telescope. Since, the telescope has to be compatible with the current APT system that has an f-number of 12, we consider the same f-number for the lens. In Sec. 2.2.3, we obtain the optimal aperture size based on free space attenuation. Thus, we could start designing the lens by knowing the diameter, focal length and f-number. In addition, we already discussed that to avoid lateral color and distortion the stop must be at the lens and to minimize axial color aberration a cemented doublet is preferred. Therefore, we need to set the material of each element, find the radius of curvature of 3 surfaces (since it is cemented the second and third surfaces have the same curvature) and determine the thickness before optimization.

An Abbe diagram, which plots the refractive index versus Abbe number, can help with identifying the right flint and the crown. It is important to keep in mind that since the doublet is cemented, the flint and the crown must have almost the same thermal properties so that any thermal expansion does not damage the lens. The initial material can be a rough estimation that gets optimized later.

A good starting point is selecting from the many commercially available glasses or the

51

suggested pairs in textbooks. For example, SK11 (crown) and SF19 (flint) or BK7 (crown) and SF19 (flint) are suggested materials in [37] and [90] respectively, which have close relative partial dispersions. Our initial starting material was 20 mm BK7 and 20 mm SF19, which was changed later in the optimization process.

The last variable left is radius of curvature. An article by Igor Nesterenko [53] studies multiple configurations of doublets and reports the OPD, strehl ratio, axial and spherical aberration for each. Then, based on the desired configuration, the equation to derive the radius of curvature is provided. The f-number of the doublets investigated in the paper is different from ours, so the numbers are not accurate, but helpful to use as starting values. We selected #4 crown-forward configuration from the paper, so $R_4 = -R_1$ and $R_2 = R_3$ was considered for the curvature of the surfaces.

$$R_1 = 2(n_1 - 1)\frac{\frac{V_2}{V_1} - 1}{\frac{n_1-1}{n_2-1}\frac{V_2}{V_1} - 1}f,$$

(3.33)

$$R_2 = 2(n_1 - 1)\frac{\frac{V_2}{V_1} - 1}{\frac{n_1-1}{n_2-1}\frac{V_2}{V_1} + 1}f.$$

We calculated the Abbe V-number at our desired wavelengths using $V = \frac{n_c-1}{n_s-n_l}$, where n_c is related to the center wavelength (980 nm), n_s and n_l are related to the shorter (785 nm) and longer (1550 nm) ones. The Abbe V-numbers for BK7 and SF19 were calculated 48.82 and 38.30 respectively. By using Eq. 3.33, the radius of curvature of each surface was calculated as R_1= 1386.93 mm , R_2=R_3= -330.221 mm and R_4= -1386.93 mm.

Now we have enough input data to create a first draft of the lens and start the optimization process. The computer adds the initial values and the desired values for a limited number of aberrations to a prescription. It computes a set of simultaneous equations to make the needed changes to the parameters. Then, it adds the new values to the prescription and repeats the process until the aberrations are as close as possible to the desired values. The *Merit Function* indicates how an optical system is close to a specified set of target values. The difference between the actual and desired value can be weighted based on the required optimization. Merit function considers the square root of the summation of the difference, so it is expected to be zero ideally. Then, the optimization algorithm aims for minimizing it as much as possible. Zemax allows us to set target values of several parameters such as aberration terms and effective focal length for all wavelengths by the use of merit function. Therefore, one can increase the weight of each term to correct the lens. Once the optimization is done, if the result does not meet the requirements, it is

suggested to optimize the material. Zemax is capable of searching through all of its glass catalogues and replaces them with the current material of each element and calculates the merit function until it finds the optimal values.

After attaining the goal performance, the initial design was sent to optical shops for fabrication. The first manufacturing challenge we encountered was changing the material according to the available options by the manufacturers. Zemax suggests a wide range of materials to maximize the performance of the lens, but not all of them are available in the stock. In addition, glasses usually come in a block of certain sizes, which were smaller than our lens dimensions. As a solution, the glass could get melted and reshaped to fit the target thickness and diameter. However, this process could add impurities and increase bubbles and inclusions in the element, which overall reduces the quality of the glass. Moreover, some glasses are more sensitive to temperature gradients, so it is crucial to select the materials with smaller thermal coefficients to avoid the temperature-induced aberrations. Also, since the two elements of the lens are cemented, the thermal property of each part must match the other one to prevent the lens from shattering when the temperature changes. Therefore, the materials were changed based on the recommendations we received from the manufacturers. Appendix A has a brief report of our experience in searching and selecting the manufacturer to fabricate our lens based on the constraints such as the time-line and costs as well as the lens quality.

In optimization of the lens 785 nm is the primary wavelength, since it is the signal wavelength used for the free space quantum channels by the telescope. Nevertheless, 980 nm and 1550 nm must be taken into consideration since they are used as the beacon signal for the QEYSSat mission. Using a doublet helps with reducing the axial color aberration, however the focal length of three wavelength do not need to be perfectly matched. The APT system which detects the beacon light and sends out the quantum signal, has two mechanically separate channels for each wavelength (Sec. 2.2.3). Either 980 nm or 1550 nm has to be focused on the beacon light detector and 785 nm is sent out from the other arm. The current configuration of APT allows about 10 mm focal shift for beacon wavelengths, so as long the variation of the focal lengths is within the acceptable range for the APT, longitudinal chromatic aberration can be ignored. Furthermore, the APT field of view (FOV) is set as ± 470 μrad, which implies that ideally the aberration must not be sensitive to field angle at ± 470 μrad. In order to have more degrees of freedom in calibrating the system we considered twice the FOV in optimizations. Thereby, considering four times of the target FOV ($\sim \pm 0.1$ degree) in the optimizations guarantees that the lens is corrected within the required region.

By taking the aforementioned conditions into account we prepared our final design (Table 3.3) which was manufactured by Hyperion Optics fabricated it. In addition, they

53

(a)

(b)

(c)
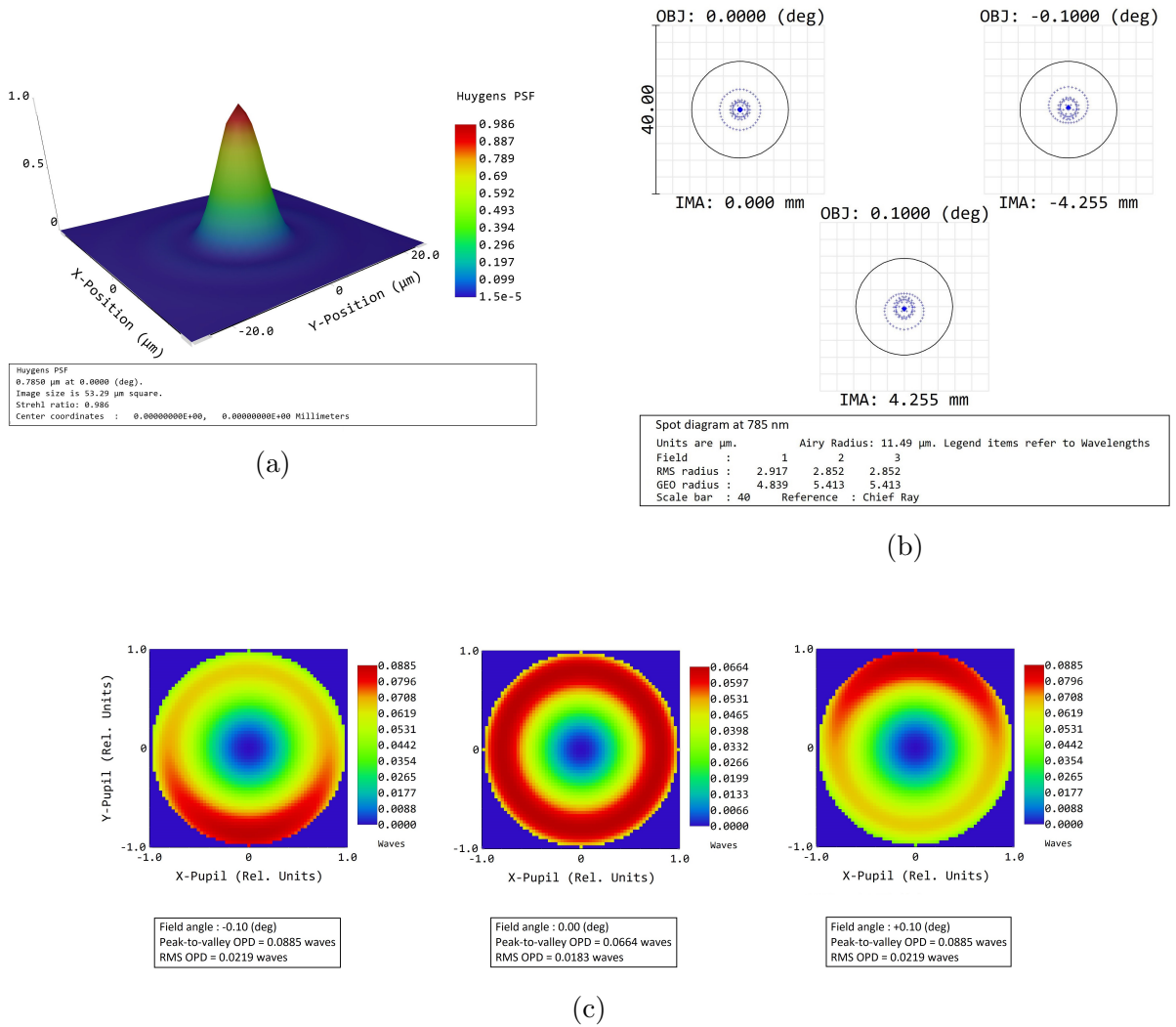
Figure 3.12: a) The 3D plot is the Huygens point spread function of the beam at the focal point. Strehl ratio is calculated as 0.986 on the optical axis. b) Spot diagram of the focused beam within the field of view; The RMS radius is smaller than the Airy disk which confirms that the lens is diffraction limited. c) Wavefront map at 0° and ±0.1°; The peak-to-valley OPD only increase by 0.022 λ at ±0.1° field angles. The wavelength in all plots is 785 nm.

54
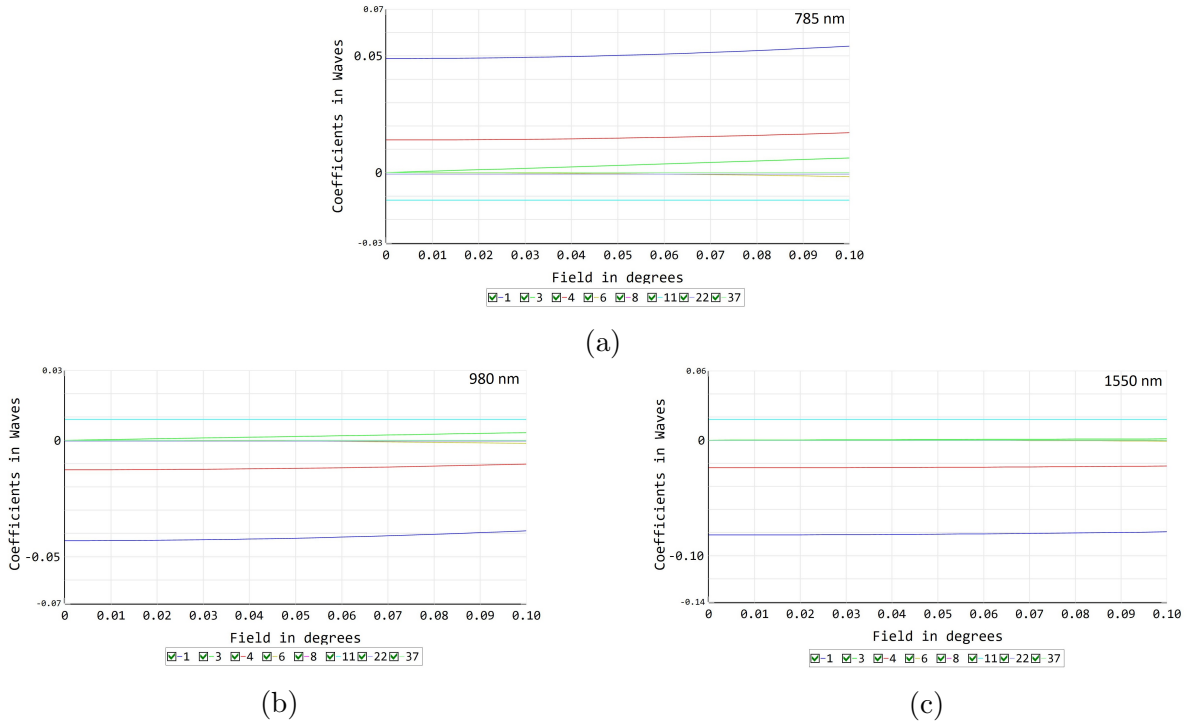
Figure 3.13: Zernike standard terms vs. field angle at 785 nm, 980 nm and 1550 nm. The variation of aberration terms are less than 0.005 waves in all wavelengths. (1: Constant, 3: Tilts, 4: Defocus, 6: Astigmatism, 8: Coma 11: 3rd order spherical, 22: 5th order spherical)

assisted with refining the lens and improving its performance. Due to their restrictions on the material, we allowed for a weak coma at $\pm0.1°$ as a trade off for minimal spherical aberration and less than 10 mm of focal shift. The resulting lens was an 8-inch doublet with 243.8 cm effective focal length (f/12) designed and corrected for Seidel aberrations at 785 nm (quantum channel), 980 nm and 1550 nm (satellite tracking signal) with Strehl ratios of 0.98, 0.99, 0.96 respectively. The two parts of the doublet are cemented and each side is coated with 6 layers of TA_2O_5 and SiO_2 to keep the reflectivity below 0.5% at specified the wavelengths. Moreover, the properties of the coated surfaces were determined to keep the wavefront distortion at $\lambda/4$ which was confirmed by our far field link modelling (Sec. 3.6).

Table 3.4 summarizes the image data for a focused beam at 785 nm, 980 nm and 1550 nm. The effective focal length of each wavelength is estimated from the center of lens to the focal point, whereas the back focal length indicates the distance between the last surface of the lens and the image plane. The focal shift is set to 5 mm at maximum to be compatible with the current APT system. To have a diffraction limited telescope the RMS

55

Surface	Radius of Curvature (mm)	Thickness	Glass	Clear Diameter (mm)
Object	Infinity	Infinity	-	-
Stop	1622.225	26	H-LAF2	203.1667
2	-639.67	0	-	202.4302
3	-639.67	20	H-ZF5	202.4302
4	Infinity	2410.212	-	201.1299

Table 3.3: Design parameters of the lens; An aperture stop is considered at the entrance of the lens. "Thickness " of each surface is referred to its distance to the next surface.

radius of the focused beam must be smaller than the Airy radius which has been fulfilled in the simulation. Finally, the peak-to-valley optical path difference (PV OPD) is minimized to reduce the lens-induced aberrations especially spherical aberration. However, due to the manufacturing constraints, surface irregularity corresponding to less than $\lambda/4$ PV OPD, requires high precision facilities which is typically costly and time consuming. So $\lambda/4$ is considered in the fabrication. More details on the surface irregularity is provided in 3.4.3. Peak-to-valley OPD is well preserved at $\pm 0.1°$ at all three wavelengths with only 0.002 λ increase at 980 nm and 1550 nm, and 0.022 λ at 785 nm (Fig. 3.12). As shown in Fig. 3.13, the Seidel aberration is more sensitive to the field angle at 785 nm comparing to the other two wavelengths. Nevertheless, the variation is less than 0.005 λ, which confirms that the lens performance does not change noticeably within the field of view.

3.3 Coating

To maximize the transmittance of the lens at certain wavelengths, it is required to use anti-reflection coating at each outward facing surface (since we are using a doublet lens, two out of four sides need coating. The other two are cemented). Optical coating is depositing thin layers of materials such as MgF_2 and SiO_2 on the surface of an optical element, with physical thickness of $\lambda/2$ or $\lambda/4$ to modify the transmission or reflection. In fact, if the deposited layer has a thickness of one-quarter wavelength, the wave reflected

Image Data	785 nm	980 nm	1550 nm
Effective focal length (EFL) [mm]	2,438	2,431.91	2,437.382
Back focal length (BFL) [mm]	2,410.212	2,404.179	2,409.654
Airy radius [μm]	11.490	14.340	22.680
RMS radius [μm]	2.917	2.139	7.406
Strehl ratio	0.981	0.990	0.966
Peak-to-valley OPD [waves]	0.066	0.057	0.109

Table 3.4: Lens data from Zemax simulation at three different wavelengths.

from the second layer and the first layer have $\lambda/2$ phase difference, which cancel out each other when they combine at the first surface. If the total power of light from each surface is equal, then a full cancellation will happen and no light will be reflected [78]. According to the range of wavelengths for each application, the coating differs. V-AR is used for short ranges such as visible light whereas, broadband AR coating is needed to keep the reflectivity low over wide spectrum of wavelengths such as NIR II (750 nm-1550 nm). Regarding our custom-designed lens, 6 layers of Ta_2O_5 and SiO_2 were deposited on both surfaces of the doublet to keep the reflection below 0.5% at 785 nm , 980 nm and 1550 nm (Fig. 3.14). The throughput power measurement was done to confirm the transmittance of the lens using a narrow laser beam. At first, we simply used a power meter to measure the power at random spots before and after the lens. Later, we used a broad band light source to measure the optical spectrum of the transmitted light to observe the transmission at different wavelengths. The initial power measurements confirmed that the power was varying less than $0.1\mu W$ (for a 23.5μW beam) at 785 nm, we therefore assumed unity transmittance at this wavelength. Direct power measurement of 980 nm was not feasible,

since we did not have the required light source. Finally, we tested 1550 nm and measured average $(3.97 \pm 0.844)\%$ loss at 4 different spots, which agrees well with the theory. The materials used for the lens cause 3.89% absorption at 1550 nm, so considering the possible reflection from the surfaces (fig. 3.14), it is expected to experience about $(3.89 \pm 0.5)\%$ loss. Table 3.5 shows the theoretical absorption of the lens material at 785 nm, 980 nm and 1550 nm.

Wavelength (nm)	H-ZF5		H-LaF2		Total Absorption (%)
	Thickness (cm)	Absorption Coefficient (cm^{-1})	Thickness (cm)	Absorption Coefficient (cm^{-1})	
785	2.00	0.0031387	2.50	0.0020020	1.13
980	2.00	0.0020020	2.50	0.0020020	0.90
1550	2.00	0.010933	2.50	0.0065703	3.83

Table 3.5: Theoretical absorption of the lens at 785, 980 and 1550 nm based on material parameters.

In order to observe the transmittance of 980 nm, we used a spectrometer to measure the intensity variation over 600 nm to 1200 nm, before and after the lens. We used a super-continuum laser to generate a wide range of wavelengths and applied a short-pass filter with the edge wavelength at 1000 nm. Then, by coupling the light into a multi-mode fibre, before and after the lens we could measure the intensity over the spectrum. Since our previous measurements confirmed that 785 nm has almost unity transmittance, to correct the mismatch coupling efficiency occurred before and after the lens, we used 785 nm as the reference and attained the loss at 980 nm. The red line in Fig. 3.15(a) shows the measured intensity before the lens over the spectrum and the blue line is the transmitted intensity after multiplying it by the fibre coupling efficiency correction factor. The plot indicates the change in the intensity of the transmitted light at 980 nm. To obtain the amount of this loss, we divided the intensity measured after the lens, by the initial measurement before the lens as displayed in Fig. 3.15(b). As expected, 785 nm has unity transmittance, however 980 nm suffers from more loss than expected which could be the result of using a short-pass filter with a cut-off wavelength close to the one under the measurement.

Nonetheless, it verified having less transmittance at 980 nm which was mentioned in a plot provided by the manufacturer (Fig. 3.14). As a conclusion, the measured transmittance of 1550 nm was proved by comparing the measured values with the theoretical estimations and the reflectivity documents, 785 nm was measured to have almost unity transmittance considering low reflection from the surfaces and low absorption, while 980 nm transmittance was qualitatively confirmed. However, more precise measurements are required to achieve the absolute loss at 980 nm.
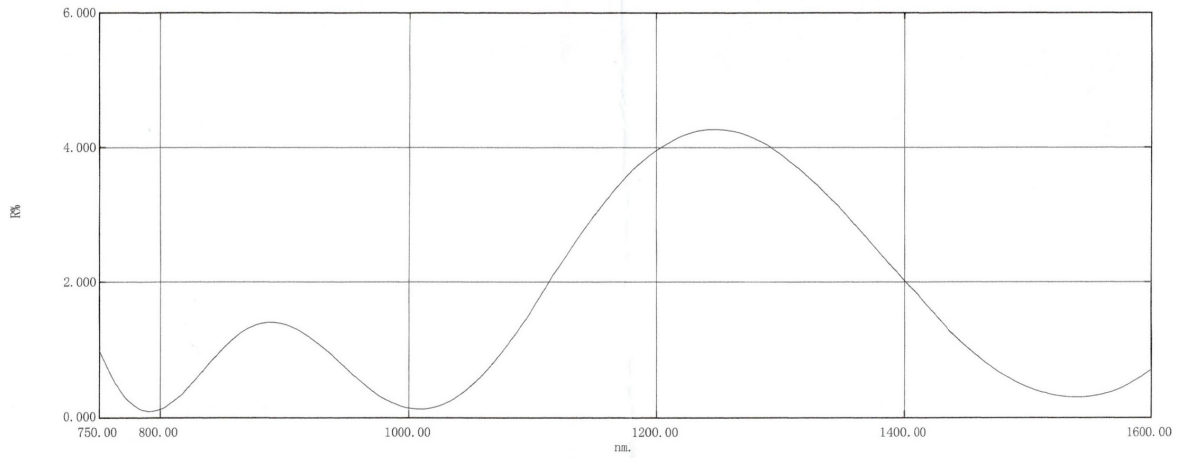
(a)
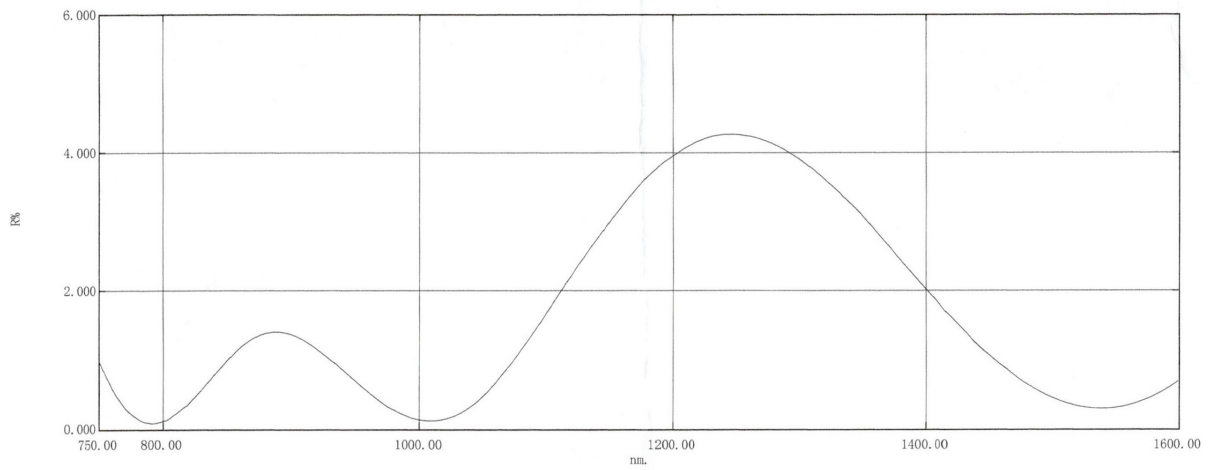
(b)

Figure 3.14: Reflectivity of (a) H-LaF$_2$ and (b) H-ZF$_5$ with AR coating over 750 nm to 1600 nm, provided by the lens manufacturer (Hyperion Optics). Reflectivity is below 0.5% at 785mn, 980 nm and 1550 nm
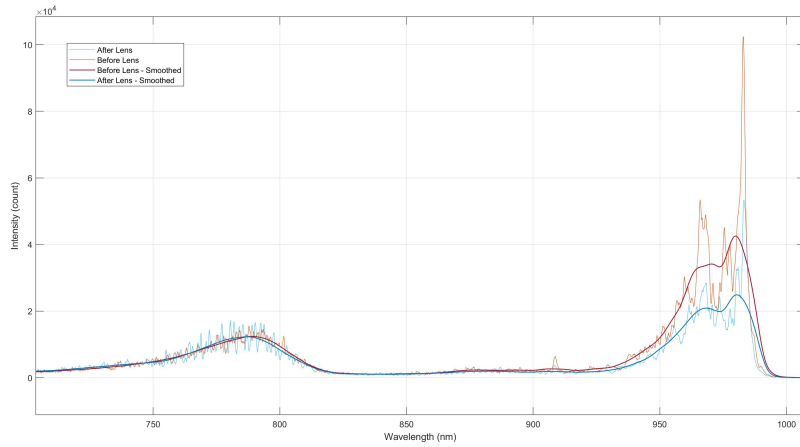
(a)
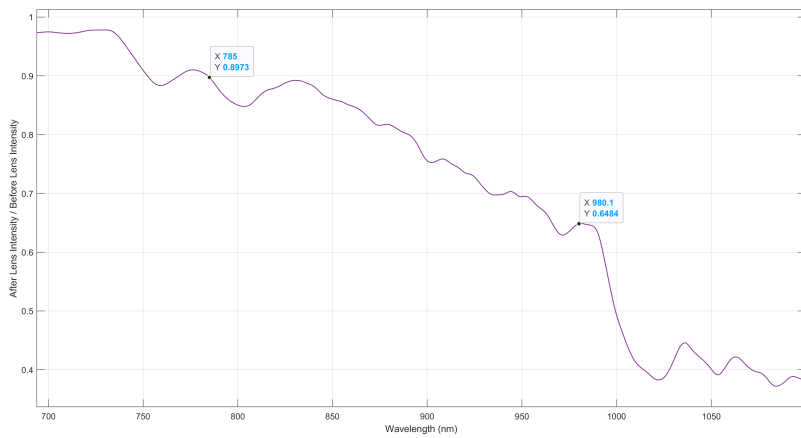
(b)

Figure 3.15: (a) Measured intensity of an incident beam (super-continuum laser with a 1000 nm short-pass filter) before and after lens; Fibre coupling efficiency mismatch is corrected by considering full transmittance at 785 nm. This plot is normalized by dividing the "after lens" data by the "before lens" results as illustrated in (b). The plots confirm almost 100% transmittance at 785 nm and 65% at 980 nm. Using a short pass filter with the edge wavelength at 1000 nm, has distorted the transmittance at 980 nm. Details of the measurement is explained in the main text.

3.4 Surface Specifications

Surface specifications is a major cost driver in manufacturing a lens. Therefore when it comes to determining the specifications, 2 factors must be taken into consideration: 1) The requirements of having high performance lens based on its application. 2) The budget and the time frame defined for the project. Almost any degrees of precision can be achieved if there are no constraints on the latter one [78]. In addition, large optics (usually larger than 6") require specific facilities which limit the number of manufacturers capable of building and polishing such optics. Manufacturing specifications are categorized as thickness, centering, scratch-dig and surface irregularity. Thickness of the element is already determined by ray tracing and optimizing the lens. Other factors are explained in more details in the following subsections.

Moreover, since the surface of any optics is prone to contamination, it is crucial to find the best cleaning method, in order not to damage the coating. In some cases, if the contamination does not affect the performance of the optic, it is recommended not to be cleaned. Regarding this custom-designed lens, as suggested by the manufacturer, a solution of 70% alcohol and 30% Diethyl ether must be used for cleaning, if needed.

3.4.1 Centering

Centering refers to the diameter tolerance and the accuracy of having the optical axis on the mechanical axis. For a centered optic, the standard diameter tolerance is usually +0.0/-0.03 to keep the element fitted in the cell or the holder it is designed for. The concentricity of an optic is defined by how much an axial ray deviates when it is incident to the mechanical center of the element [78]. To measure the deviation in a spherical lens, we send collimated light through the center of the lens along its optical axis. By rotating the lens, any decentering of the element changes the beam path and creates a circle with radius Δ in the focal plane [90]. Deviation angle and wedge angle of the lens is defined as:

$$\delta = \frac{\Delta}{f}, \tag{3.34}$$

$$W = \frac{\delta}{(n-1)}. \tag{3.35}$$

where, W is typically considered as 3 arcmin at commercial grade and 1 arcmin at precision grade. In this work, the diameter and wedge tolerance of the designed lens were set at +0.0/-0.5mm and less than 3 arcmin, respectively. These numbers were confirmed in the final inspections of the constructed lens, by the manufacturer.

3.4.2 Scratch-Dig

Scratch-Dig is a number which indicates the level of defects on the surface of optics. These defects such as bubbles or inclusions could be formed during the fabrication process. Pits, scratches or stains, could be the result of a mistake at the final steps of surface treatment. They are mostly considered as "beauty defects", since they might cause negligible loss in the throughput power or increase the scattered light, but they do not impact the performance of the optics significantly. Nevertheless, the effect could be considerable if [78]:

1. Defects are on the surface of an optical element close or in a focal plane of a lens, where the size of the defect may be comparable to the size of the image on the surface.

2. Defects are on a surface exposed to high level of power. They can absorb the energy and damage optics.

3. The system is highly sensitive to stray light.

The U.S. Military Performance Specification MIL-PRF-13830B, describes these defects as 2 numbers following each other. The first number refers to "scratch", which is related to the apparent size of a tolerable scratch and compares it with an standardized one [92]. The number could be 10, 20, 40, 60, 80 or higher. The larger the "scratch" is, the more brightness a scratch on the surface has. The second two digits represent "dig", which is the diameter of pits in micron divided by 10. So a dig number of #40 stands for a pit with 0.4 mm diameter [78]. "Scratch-dig" numbers of 80-50 or larger are usually achieved easily in commercial optics. 60-40 and 40-20 have more precision and they are recommended to be used for low to moderate power laser which can tolerate little scattered light. 20-10 and smaller are considered as very high precision that are usually required for extra-cavity or intra-cavity optics [92].

In this work, since our system is not too sensitive to the defects according to the definitions mentioned above, it was possible to have larger scratch-dig (S/D) number to save on the time and the costs. Our doublet lens has S/D = 60-40 after coating for each surface.

3.4.3 Surface Irregularity

Surface irregularity is the most important factor in determining the wavefront error of the beam. It is usually measured by counting and examining the regularity of interferometric
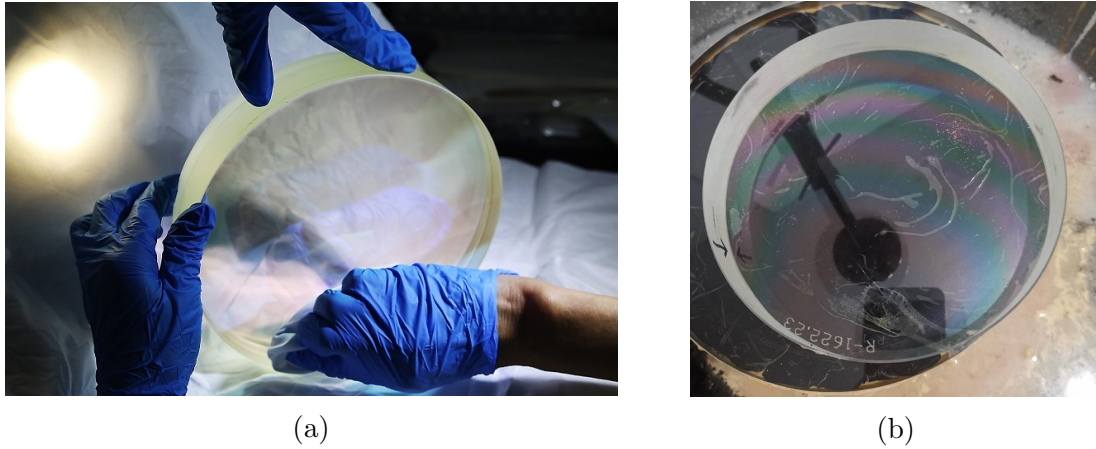
Figure 3.16: (a) The custom designed lens fabricated by Hyperion Optics lens. (b) The lens is under the measurement to determine its surface irregularity. Power rings (Newton's rings) can be seen in the photo. (The photos are taken by the manufacturer.)

fringes (Newton's rings) that appear due to the difference between the sphericity of the surface under the measurement and a test plate. Test plates are considered to be extremely flat to be used as the references in surface measurements. The fitting of the element in the test plate gauge must be within an exact number of fringes and it must have the regularity within a certain number of rings. For instance, if the fit does not show more than 5 fringes, then identifying irregularities of less than 1 fringe is impossible. The common ratio of these power rings to the maximum tolerance of irregularities, must not be less than 4 or 5 times, otherwise, the irregularity of a small part of the ring can not be resolved easily. Our lens surface was considered to have less than 5 power fringes to have the required precision in measuring the flat and spherical surfaces [78]. The power rings of the lens are shown in Fig. 3.16. To obtain the wavefront error induced by surface irregularity, Peak-to-Valley OPD is expressed in terms of the observed fringes (FR):

$$OPD = \frac{1}{2}(\#FR)(n' - n)[\text{waves}]. \tag{3.36}$$

A "sensibly", well corrected optic must be within Rayleigh criterion which indicates that the Strehl ratio remains more than 80%, if OPD does not exceed $\lambda/4$. Therefore, Eq. 3.36 can be rewritten as an inequality for all surfaces,

$$\Sigma(\#FR)(n' - n) < 0.5. \tag{3.37}$$

Considering a material with $n' = 1.5$, Eq. 3.37 implies that the element can have half-fringe of any irregularities on each side, while staying in Rayleigh criterion. Thus, irregularity tolerance of each surface can be determined. [78]

In terms of manufacturing specifications, surface irregularity of 1λ is known as a typical grade, whereas $\lambda/4$ is considered as precision grade and $\lambda/10$ and $\lambda/20$ are used for very high precision applications [90].

Our custom-designed lens is optimized to have minimum OPD, which is 0.066λ at 785 nm. However, obtaining this value in the fabrication, was not practical according to our budget and timeline. So we studied the far-field beam detected by satellite, considering the turbulence and optics imperfections to determine the maximum surface irregularity that can be negligible comparing to atmospheric effects. As a result, we confirmed that $\lambda/4$ is an optimum trade-off for the lens performance and the costs. The link analysis is presented in Sec. 3.6.

Surface irregularity of each surface of the lens was measured using a Zygo laser interferometer[7] with a 546.07 nm laser by the manufacturer. The PV irregularity of each surface is reported less than $\lambda/4$. However, due to the limitations of the device, only some parts of the lens were measured. The results are shown in Table 3.17. Since, this measurement was not taken using a 785 nm laser, we did a wavefront measurement with our home-made setup to comprehend the effect of the lens surface irregularity on the wavefront of the transmitted beam, which is discussed in Sec. 5.2.

The surface specifications of the lens are summarized in Table 3.6. Appendix B demonstrates a list of manufacturing surface specifications of a spherical lens, provided by a optical manufacturer.

---

[7]Zygo is an optical metrology instruments supplier. Hyperian Optics used their laser interferometer to measure the surface flatness of the lens.

Surface Specifications				
Center Thickness Tolerance	Diameter Tolerance	Centering	Scratch/Dig	P-V Irregularity
± 0.4	+0/-0.5 mm	W < 0.3 arcmin	60-40	OPD $< \lambda/4$ Left: 5(0.5)* Right: 3(0.5)

*A fit of five power rings, with a sphericity or regularity of half ring

Table 3.6: Surface specifications of the telescope lens, designed by our group, fabricated by Hyperion Optics. The numbers are reported by the manufacturer and the measurements were done at 546.07 nm.

3.5 Folding Mirrors

A pair of folding[8] mirrors are considered in the design of the telescope to allow for fine alignments and calibration, as well as reducing the total length of the tube. The mirrors are fixed on motorized mounts that can tilt the mirrors with high precision. The position of the mirrors are added to the Zemax design, considering the dimensions of their mounts and position of the focal point. Both mirrors are 8° tilted to minimize the total diameter of the tube. As a result, a beam with diameter of 200 mm goes through the lens and converges to 140 mm at mirror 1 and 74 mm at mirror 2. In the design, first we considered the size of the mirrors as the same size of the beam reflecting from them. Then, by looking at the commercial size of mirrors, and also considering the fact that the beam must not be too close to the edges, we opted a 6-inch mirror (diameter of 152.4 mm) as mirror 1 and a 4-inch one (diameter of 101.6) as mirror 2, with flatness of $\lambda/20$. More information on the purchased optics and mounts are discussed in chapter 4.

3.6 Link Analysis Impacted by Lens Aberration

It is important to have a full understanding of the characteristics of the beam detected on the receiver since it can facilitate the improvements of the quantum channel efficiency. As discussed in Chapter 2, atmospheric turbulence can be detrimental to a free-space link and affect the far-field beam spot significantly. However, the distorted wavefront can be

---

[8]Since these mirrors bend the beam and create a z-shape path, they are known as folding mirrors.
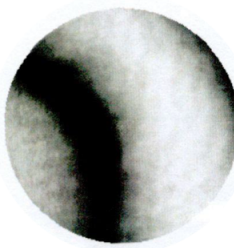
Surface 1	Radius of curvature: 1622.225 mm	Power: 0.10 fringes	
		Irregularity: 0.19 fringes	
		PV Irregularity: 0.082 waves	
Surface 2	Radius of curvature: -639.67 mm	Power: 4.87 fringes	
		Irregularity: 0.23 fringes	
		PV Irregularity: 0.097 waves	
Surface 3	Radius of curvature: -639.67 mm	Power: 4.17 fringes	
		Irregularity: 0.43 fringes	
		PV Irregularity: 0.184 waves	
Surface 4	Radius of curvature: Infinity	Power: 0.18 fringes	
		Irregularity: 0.34 fringes	
		PV Irregularity: 0.163 waves	

Figure 3.17: Surface irregularity measurement; The images are the intensity map of the scanned area. The measurement was taken by Hyperion optics.

corrected with modeling the turbulence and compensating for it by using adaptive optics such as spatial light modulator (SLM). This approach is beneficial to both astronomical and military applications [43][44] as well as free-space QKD. Zernike polynomials (Eq. 3.1) can be advantageous in modelling turbulent atmosphere using Kolmogorov model. These polynomials are complete and orthogonal and directly represent known optical aberrations. In addition, Kolmogorov turbulence polynomial coefficients can be analytically calculated. Thus, Zernike polynomials are a convenient basis-set to model the atmosphere [55].

As mentioned in Section 3.10, Zernike polynomials can be used to define a phase mask that changes the optical wavefront of the propagated beam. Considering a function such as,

$$\phi(\rho, \theta) = \sum_{n=0}^{\infty} \sum_{m=0}^{n} [A_{nm} U_{nm}(\rho, \theta) + B_{nm} V_{nm}(\rho, \theta)].$$

that is a linear sum of U_{nm} and V_{nm} with arbitrary weighting of coefficients, the phase mask induced by the turbulence, can be modelled by Kolmogorov theory. In the Kolmogorov model usually only even terms (A_{nm}) are considered, $A_{nm}=B_{nm'}$. To extract the phase function, the Noll Matrix approach is used [55]. As a result, normally distributed Zernike coefficients with mean zero have the variance as below [18],

$$\sigma_{nm}^2 = I_{nm} \left(\frac{D}{r_0}\right)^{5/3},\tag{3.38}$$

Where I_{nm} is the so-called Noll matrix and it is expressed as [55]

$$I_{nm} = \frac{0.15337(-1)^{n-m}(n+1)\Gamma(14/3)\Gamma(n-5/6)}{\Gamma(17/6)^2\Gamma(n+23/6)}.\tag{3.39}$$

To generate the phase mask, one must calculate 3.39 and obtain $\sigma_{n'm'}^2$ from Eq. 3.38, for the desired n' and m' based on the turbulence strength presented by Fried's parameter (r_o). Using using this distribution, the coefficients $A_{n'm'}$ can be randomly chosen. Effectively, by taking the summation over all A_{nm} coefficients, many Kolmogorov phase masks are constructed which simulate the random atmospheric turbulence [14]. Moreover, the Strehl ratio can be derived as $exp(-\sigma_{nm}^2)$. Finally, Rayleigh-Sommerfeld diffraction theory is used to calculate the intensity of a far-field beam, for an arbitrary input beam going through a random phase hologram created by the simulated turbulence [9]:

$$I_{out}(c, d) = \sum_{a,b} \frac{z^2 \Delta a^2 exp[i\phi(a,b)]\sqrt{I_{in}(a,b)} \exp\left\{\frac{2i\pi\sqrt{L}}{\lambda}\right\}}{L\lambda},\tag{3.40}$$
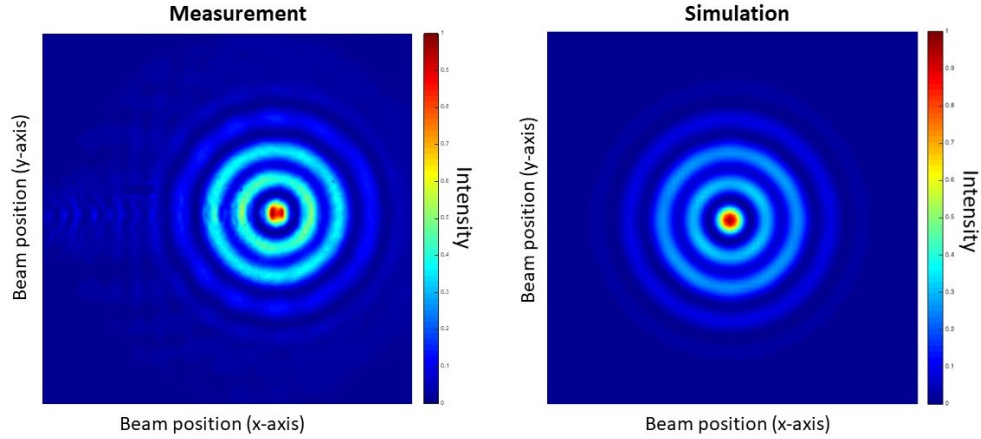
Figure 3.18: The spherical aberration is modelled using Zernike polynomials and uploaded on an SLM. The left image is the output measured on the SLM and the right is a contour plot generated by our code in MATLAB. These plots were created by Dr. Katanya Kuntz.

Where $L = z^2 + (c - a)^2 + (d - b)^2$, (a, b) is the input beam coordinate, (c, d) is the output beam coordinate, Δa is the spacing between the pixels of the input image and $\phi(a, b)$ is the phase hologram.

Furthermore, due to the beam wandering, the centroid displacement must be taken into account for the far-field beam simulation. The tilt angle variance of centroid displacement is expressed as [18][83],

$$\sigma^2 = 0.364 \left(\frac{D}{r_0}\right)^{5/3} \left(\frac{\lambda}{r_0}\right)^{5/3}. \tag{3.41}$$

The QPL group developed a program to generate random turbulence holograms according to the turbulence strength, to predict the beam quality received by the satellite in LEO orbit. We uploaded the holograms on an SLM and simulated the desired aberration or random turbulence to observe how it affects a beam at the far field. Then, the measured output beam was compared with the model calculated and plotted by the code [18]. (In this model, r_0 remains the same along the path, however, in a ground-to-satellite link, the strength of the turbulence can vary.) Fig. 3.18 shows a simulated spherical aberration which was measured on the SLM and generated by the code. The result validates our approach. One can use this method to apply desired combinations of the Zernike terms on the beam.

To model the turbulence, we generated random weightings for 44 terms of the Zernike

69

polynomials based on the turbulence strength (r_0) and applied them to the input beam as a phase mask. Several unique hologram masks were generated to obtain a more realistic model of the turbulence. From Fig. 2.10, we calculated that the maximum coherent diameter of the atmosphere corresponds to 90° elevation angle that equals 8.5 cm (It can be considered as the minimum turbulence strength). Fig. 3.19, illustrates the impact of random turbulence with an 8.5 cm Fried's parameter on a 7.17 cm input beam ($1/e^2$ beam waist is considered), generated by one phase mask.

Moreover, as discussed before, lens properties can be also defined in Zernike terms. To study the lens aberrations effects, the weightings obtained from the Zemax model can be used for the hologram mask. They get added to the random turbulence weightings to have a qualitative understanding of the beam behaviour affected by the lens imperfections in presence of atmospheric turbulence. Fig. 3.19(f), presents the far-field beam transmitted from our custom-designed lens under the same turbulence mask. As a result, we comprehended that the aberrations of our lens do not affect the far-field beam with considering the minimum predicted turbulence.

In Sec. 3.4.3, we discussed how the surface irregularity can be a cost-driver in the process of the fabrication, so we corrected the lens for different optical path difference (OPD) values to find the optimal one considering both the costs and the quality. Fig. 3.20, shows the output beam results for (d) 0.1 λ, (e) 0.2 λ, and (f) 0.5 λ peak-to-valley OPD. 0.25 λ is the precision grade, which is usually used for commercial optics, anything below that requires more effort and consequently an increased price. It is observed that 0.5 λ OPD shows significant spherical aberration comparing to the others. However, 0.1 λ and 0.2 λ, show less than 5% difference in the intensity of the spherical aberration rings. Therefore, 0.2 λ is an optimal estimation for the surface specifications in the fabrication process.

So far using these methods, we are able to plot the minimum link loss at different zenith angles for a beam transmitted by a ground station and received by a satellite 600 km above the earth (2.1.6). We also studied the impact of turbulence and lens aberrations on the beam shape, qualitatively over a path of 600 km with constant r_0 (Section 3.6). We are looking into expanding our analysis to model the transmitted beam on the satellite and obtain more precise and quantitative results on the effects of the atmosphere and the lens aberrations as well as the losses induced by the receiver, such as fibre coupling efficiencies, in both uplink and downlink channels.

70
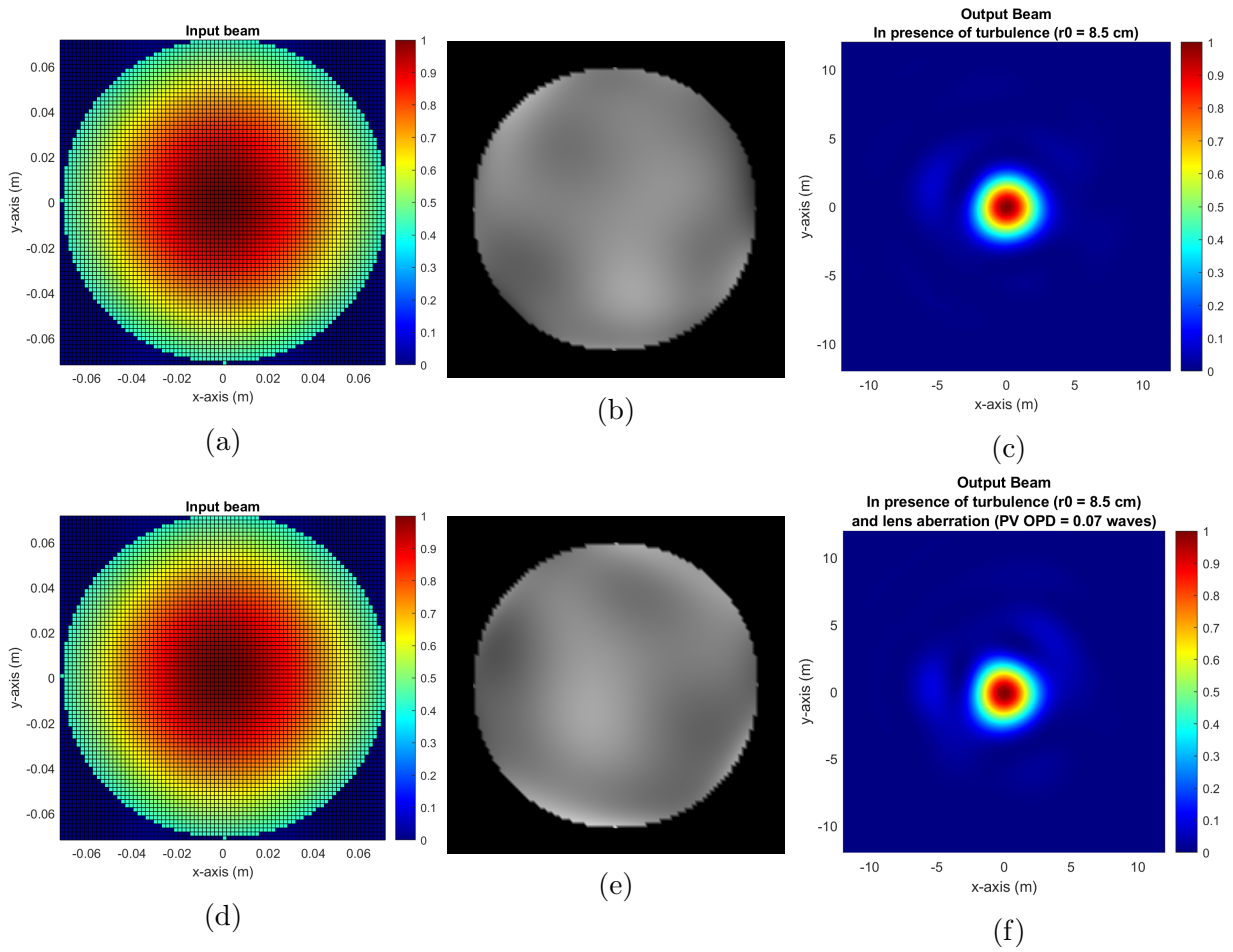
Figure 3.19: Top: A phase mask (b) is generated to simulate the atmospheric turbulence for r_0=8.5 cm and it is applied to the input beam (a) to study the far-field beam (c). Bottom: Same turbulence with the lens aberration, is considered in (e) and applied to the input beam (d). The far-field beam (f) indicates that the lens aberration does not affect the received beam noticeably.
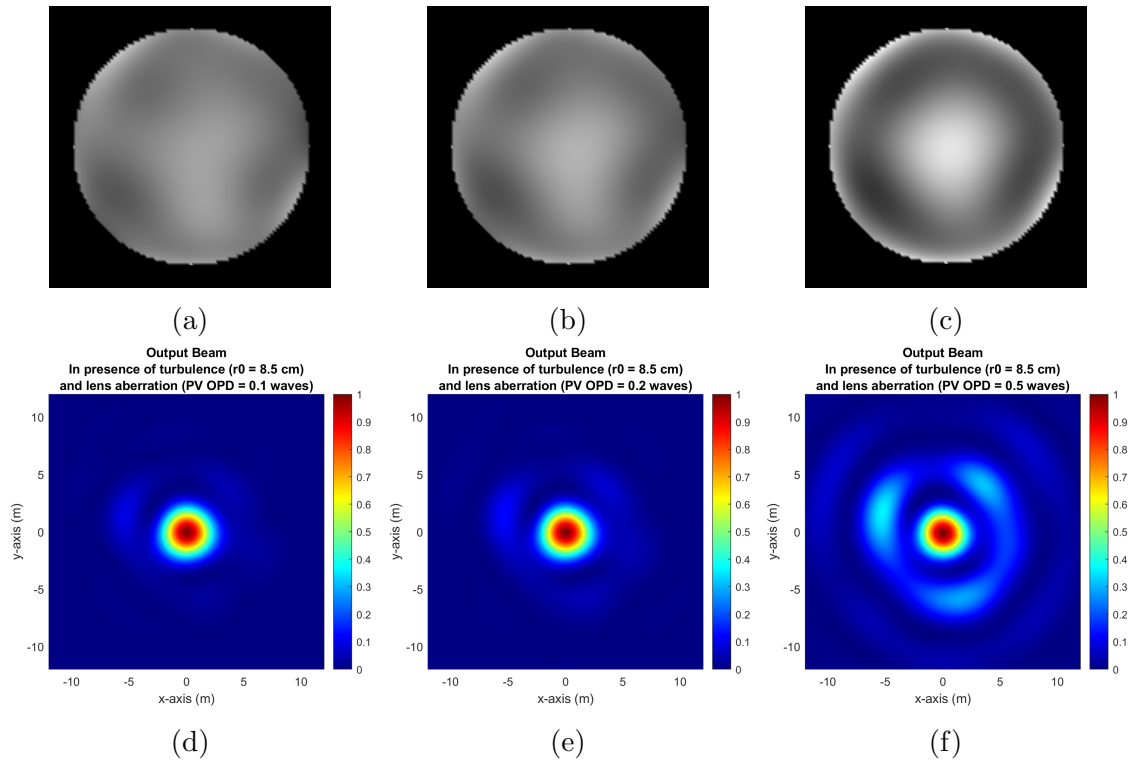
Figure 3.20: We generated the phase mask for different peak-to-valley optical path differences. The first row shows the holograms applied to the 7.17 cm input beam in Fig. 3.19, and the second row is their effects on the far-field beam. As a result, $\lambda/4$ OPD (e) is a promising surface quality for the lens of a transmitter, in presence of the turbulence. Increasing the OPD implies more spherical aberration in the image (f).

Chapter 4

Mechanical Design

Not only does our new transceiver telescope have a custom-built lens, but also its mechanical parts have been designed and optimized for higher functionality and stability while keeping the total weight as light as possible. The telescope will feature two motorized folding mirrors inside the tube to allow easy and precise fine alignments, as well as reducing the total tube length by more than half. Moreover, the telescope tube will be built from carbon fibre to minimize bending, weight, and thermal expansion whereas, the remaining parts are built from aluminum to be easily machined (the softness of this metal was considered in the design to avoid any deformations). As a result, our custom telescope assembly weighs less than 30kg, including all the mounted optics. The weight and specifications of each individual part are provided in Table 4.2 and 4.1. Furthermore, the coating of the interior parts are investigated to minimize the reflection of stray light inside the tube at NIR range.

We used Solidworks computer-aided design (CAD) program to design all mechanical parts, which were either purchased from commercial options or built by University of Waterloo science machine shop.

4.1 Telescope CAD Model

The overall design concept is a folded refractor. The refractor is chosen because it offers an unobstructed aperture, while the folding is selected in order to reduce the length of the tube, as well as enable fine-alignment by moving the two folding mirrors.
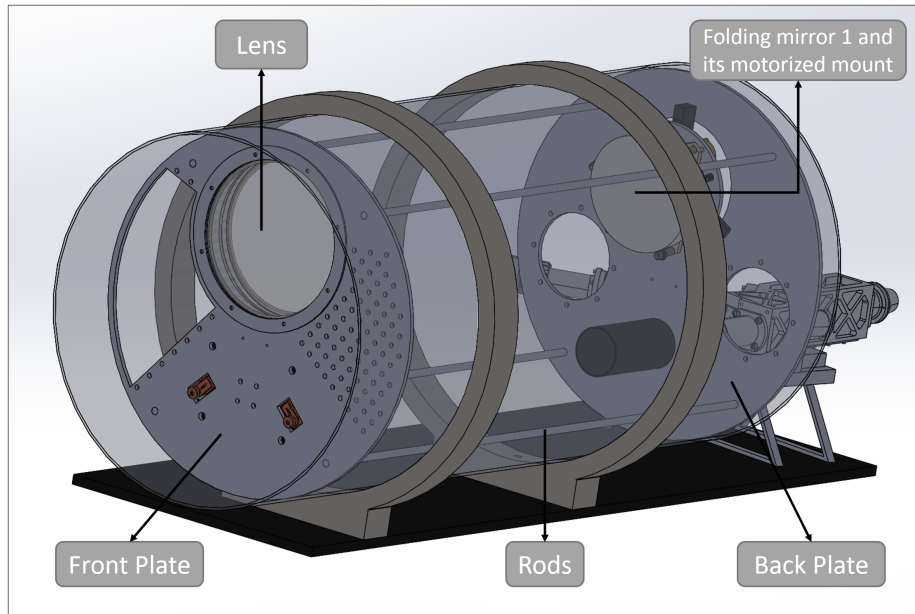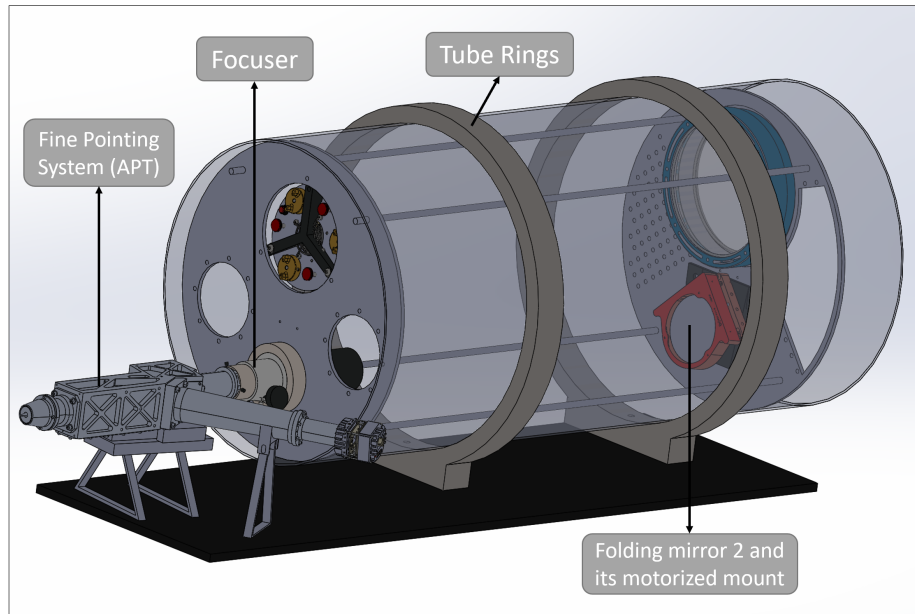
Figure 4.1: CAD model of the whole telescope with the APT attached to it. The tube is fixed on the black breadboard via 2 tube rings. The APT at the back of the telescope in connected to a focusor and placed on the board with a dovetail and brackets. (a) and (b) show the front and back view of the telescope.

A design goal was that the motorized folding mirrors and the mounting of the end-plates, have a sufficient range of motion such that the focal plane can be either inside or outside of the tube. Another design challenge was how to correctly assemble the parts of the telescope, in particular the two end-plates. During assembly, we must ensure the two plates are parallel to each other to avoid any tilting effects in the experiment. However, having identical mounting holes with equal spacings at each end of the tube, can not be done accurately due to the limitations of the machine shops. As a solution, we used four same length rods that connect the two plates together to avoid the tilting of each plate with respect to the other one. Also, by use of different sizes of spacers the distance between the end plates can be adjusted and then fixed inside the tube using six brackets. In this section we discuss the logic and concerns behind the design of each individual part in more details.

4.1.1   Lens Cell

Unlike most telescopes which have a primary mirror or a lens fixed inside the walls of the tube, our telescope requires a lens cell that can be fixed on the front plate, since the tube is much larger that the lens itself (Fig. 4.1. Also, since big lenses of refractive telescopes typically come with their own lens cells, it is unlikely to find the required cell from the commercial options. Therefore, we designed and machined our own lens cell based on the requirements and constraints discussed below.

The design challenge for the cell is to ensure the lens is firmly fixed inside the cell, however without any noticeable stress on the lens to avoid stress-induced birefringence or aberration that can alter the polarization of the transmitted beam. In addition, as the telescope will be used for outdoor experiments, allowing for thermal expansion is critical. Another requirement that we considered in the design, was being able to use the lens cell separately, when it is not mounted on the plate, for further tests on the lens.

As a result, we designed the lens cell in two parts that slide in each other and hold the lens in between. Fig. 4.2 shows the configuration that consists of two separate parts: Part A and Part B. Part A has 8 threaded holes fixing this part to the plate. On the other side, a set of 8 threaded holes are used to screw down part B to part it (The holes are distributed with equal spacing for the sake of symmetry). Part B has a short wall which helps with sliding in and centering the two parts. There is a 5.7 mm gap between them to allow for thermal changes without exerting force on the lens. We added two high temperature soft silicon O-rings to cushion both sides of the lens, to absorb pressure along its edges, and to protect it. Slot cuts were added on both parts for further weight reduction. It
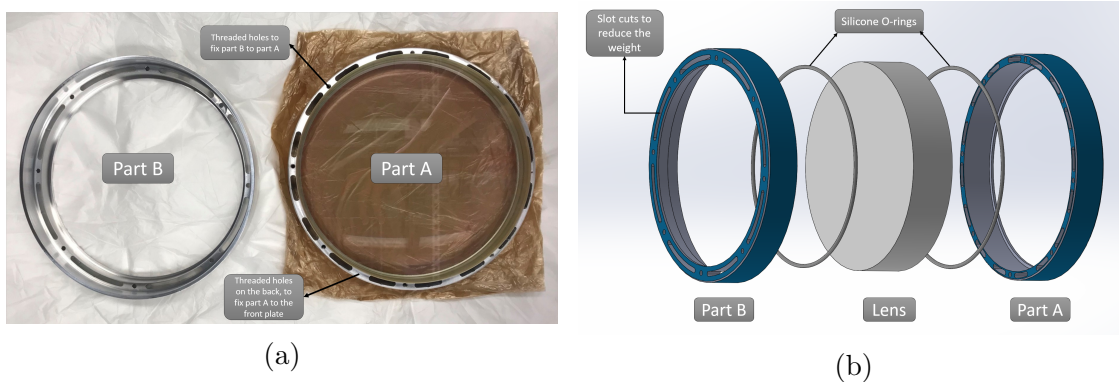
Figure 4.2: (a) The fitting test of the lens cell before anodization. (b) An exploded view of the designed lens cell in Solidworks. The lens is fixed between the two parts of the cell and two soft silicone O-rings.

is worth mentioning that, the lens cell dimensions were also kept to a minimum, since it directly determines the main tube size. However, thin walls especially near the cuts can be problematic. So holes must not be placed too close to the edges to avoid structural failure. As a rule of thumb, a hole fitted for a certain bolt size must have enough clearance to the edge to fit a nut of the corresponding size. Taking this into account, the thickness of the walls and locations of the holes are set.

The inner diameter of the lens cell was machined slightly smaller than the design and then it was fixed after couple of fitting tests, since taking out the material is easier that adding it on, in case of having a loose fit.

4.1.2 Folding Mirrors

Each folding mirror section has three main parts: 1) the mirror, 2) the mirror mount, 3) the mirror base plate. Both flat mirrors have protected silver coating on Zerodur substrate which is a glass ceramic with extremely low Coefficient of Thermal Expansion (CTE) and extremely smooth surface with residual roughness below 1 nm. Protected silver coated mirrors offer the highest reflectivity (R) from 450 nm to 2000 nm with R > 98%, compared with gold or aluminum coating. The purchased mirrors have $\lambda/20$ flatness to minimizes wavefront distortion. Mirror mounts compatible with motorized control were selected to reduce human alignment error. Mounts were purchased off-the-shelf, and the mirror base plates designed and machined in-house, based on the angles from Zemax simulation in

76

(a)

(b)
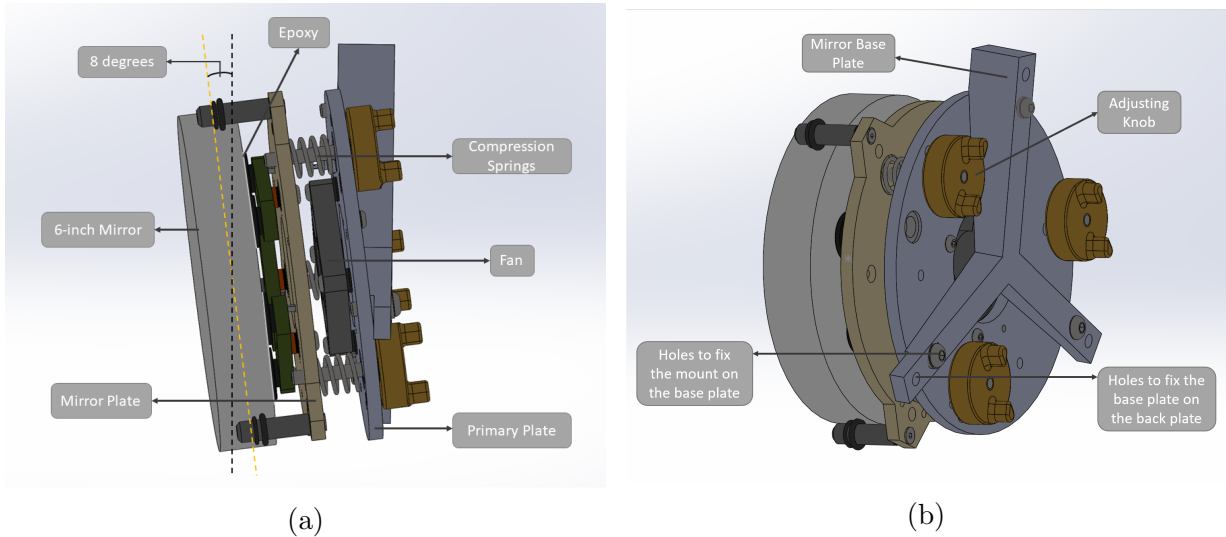
Figure 4.3: 6-inch mirror mount with the angled base plate to provide 8° tilting.

Sec. 3.1. The mirror base plates provide the initial 8° angle required to guide the beam and also to enable using the full tilting range of the mounts.

Mirror 1: Mount and Base Plate

In our search for a motorized 6-inch mirror mount, we did not find any commercial options since they are mostly intended to be used as the cell for the primary mirror of Newtonian telescopes rather that for optics research labs, so they do not have high precision motors and are usually designed to be fixed inside the telescope tube rather than on a plate. Hence, we modified an off-the-shelf mirror mount (AZ-mirror cell of Aurora Precision), replacing its adjusting knobs with high precision motors. Fig. 4.3 is the CAD view of the mount. It consists of two plates held together by compression springs with three adjusting knobs. Each threaded-stud knob goes through a clear hole on the primary plate and screws into the mirror plate to compress the spring and pulls back that part of the mirror. Once the knob rotates counter-clockwise the spring goes back to its rest position, as a result it pushes the mirror to set it at the desired angle. So it is important to keep the springs slightly compressed initially, that it allows the tilting range required. The more the springs get compressed, the harder it gets to rotate the knob. Therefore, in order to replace them with motors, the required high torque must be taken into consideration. A maximum of 4.52 N.m torque was measured for an adjusting knob with a complete compressed spring.

Two of the springs were almost at rest (same stiffness for those 2 knobs) and the third knob was tightened by a torque wrench, to compress the spring as much as possible. Also, to be in the safe side, it is recommended to consider motors with at least twice the torque needed.

For this purpose, piezo motors are lightweight and have high precision, but can only supply torques about 0.018 N.m. However, stepper and servo motors can supply the necessary torque, at the cost of adding considerable weight to the system. As an example, a motor compatible with our system is about 1.5 kg which adds 4.5 kg in total to the weight of the telescope and more importantly on the back plate. A Dynamixel DC Servo motor was the ultimate solution. This motor includes a fully integrated DC Motor, controller, driver, sensor, reduction gear and network, all in a DC servo module which is a robot exclusive smart actuator. It is 33.5×58.5×44 mm and only weighs 165 g despite providing maximum torque of 12.9 N.m. With 4.3 mrad backlash and 1.5 mrad resolution, these motors were a perfect match to replace the adjusting knobs of the mirror mount. They can be controlled by Dynamixel SDK or the Dynamixel software. We used a U2D2 and its power hub board provided by the company to control all 3 motors with Dynamixel software. First, each motor must be connected individually to set its ID number (Each motor is already labelled with a number). Then, they must be wired up serially and connected to the power board. Using Dynamixel Wizard 2.0 software, each motor can be turned on and off separately. It is important to change the operating mode of the motors to "Extended Position Control Mode" before using them since, it allows having multi-turns. The ID number and operating mode are saved in EEPROM area and the modified values get restored as the initial values. In order to change the parameters one can use "Packet Window". More instructions are provided in Robotis "DYNAMIXEL XM540-W270-R Manual" and "DYNAMIXEL Wizard2.0 Manual". In the main screen of the software "Profile Velocity" should be set at 50 to have safe slow revolutions. Now the motors are ready to operate. After turning on the "Torque" of each motor, they can move according to their target position (11.37 position displacement of the motor corresponds to 1° rotation).

Next, the motors must be fixed on the plate, which was quite challenging, since the initial design of the mirror cell required the threaded-stud knob to be normal to the mirror plate and angled with respect to the primary plate. Fixing the motors on the primary plate results in having the shaft perpendicular to both plates which does not allow for the tilting. Since we did not have room for mounting the motors on the mirror plate to solve the tilting problem, we used flexible shaft couplings to mount the motors on the primary plate while tilting the mirror. A threaded shaft goes through the clear hole on the primary plate and is screwed into the mirror plate as it initially was. Then, the end part of the
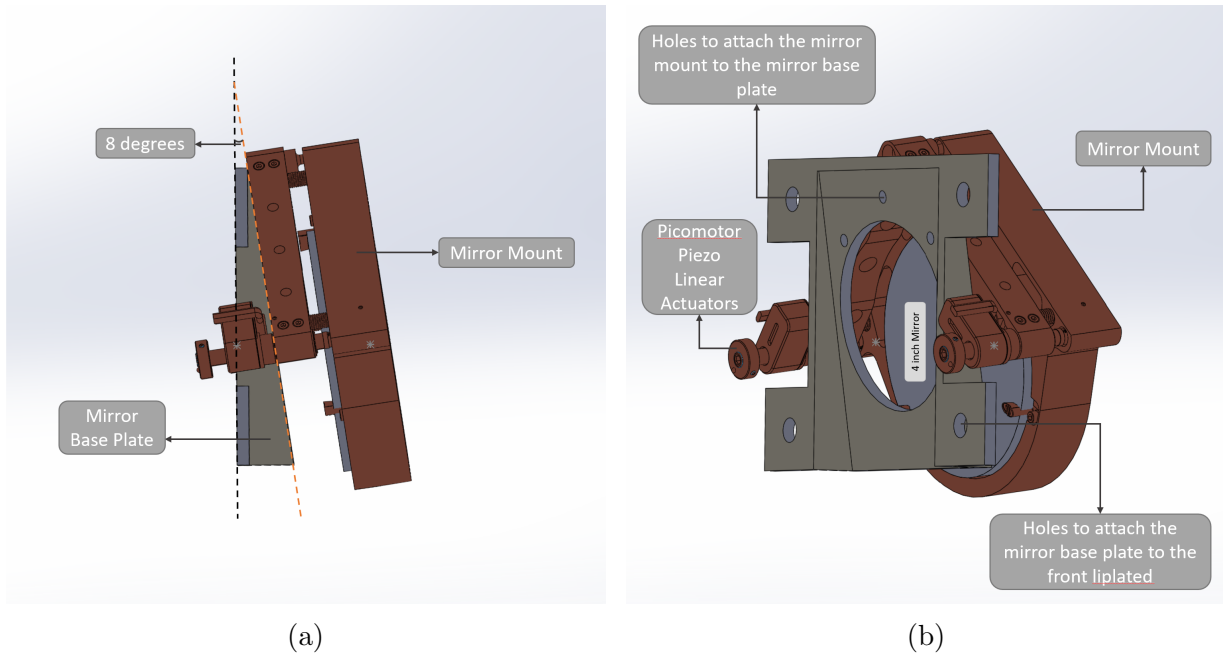
Figure 4.4: 4-inch motorized mirror mount fixed on an angled base plate.

shaft (on the primary plate side) is connected to the shaft of the motor via a flexible shaft coupling which handles up to 5° angular difference between two shafts (Fig. 4.3(a)). Hence, the motors could be fixed on the primary plate using brackets and could push and pull the mirror plate using the shafts and the couplings.

The mirror base plate is basically an adaptor plate which provides the 8° tilting required and it is designed based on the holes and available space on the mount. There are two holes at each end, the clear hole is used to attach the mount to the mirror base plate and the threaded one is used to fix the whole mount on the back plate of the telescope.

Finally, the mirror was glued to the mount as instructed on Aurora Precision website, using "DowSIL-RTV Sealant-732" epoxy. We let it cure for 48h before moving it.

Mirror 2: Mount and Base Plate

The motorized mount of mirror 2 was chosen from the commercial options, since 4-inch mirrors are more common than 6-inch ones to be used in optical research labs. The Picomotor piezo mirror mount of Newport was purchased for this purpose. This mount

79
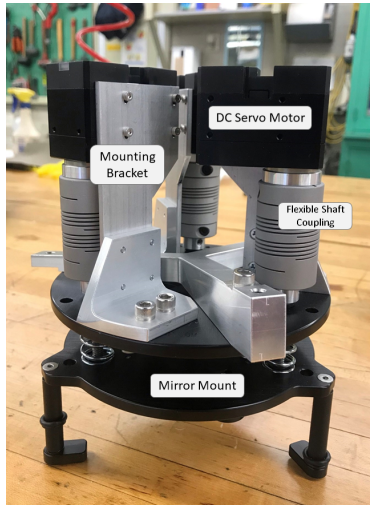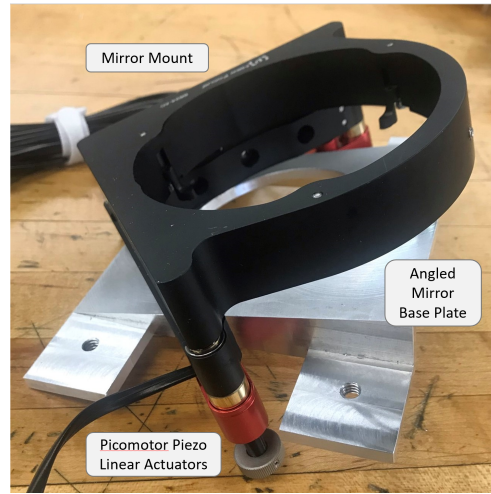
(a)   (b)

Figure 4.5: (a) 6-inch mirror mount with the servo motors replaced with the adjusting knobs, using flexible shaft coupling and brackets. (b) 4-inch motorized mirror mount. (The aluminum parts in the photo are before anodization)

allows tilting around 2 axis with $\pm 3.5°$ angular range and 0.7 μrad resolution. An Open-Loop Picomotor Motion Controller is used to drive the motors. It provides Windows DLL for programming as well as PicomotorApp 2.1.5 software with a user friendly panel to change the acceleration and speed of each motor before moving it to the desired angular position (1° corresponds to about 47,503 steps). Before mounting the mirror on the plate, we set the angles at zero by using 2 pinholes with the same height, one close to the source and one close to the mirror so that the beam goes through both of them and reaches the mirror. Then, the motors were adjusted to detect the reflected beam on the source. If the reflected image falls on the point source, it proves that the mirror was not tilted initially.

The mirror mount is screwed down to its base plate to be parallel to Mirror 1 (8° angled). As shown in Fig. 4.4 the plate is made to be hollow and has a circular cut in the middle to reduce the weight as much as possible. Although the mirror was mechanically fixed inside the mount, we secured it by super glue as well, to avoid any wobbling of the mirror in future. Fig. 4.5 shows both mirror mounts after machining the parts and applying the required modifications.

4.1.3 End-Plates and Rods

The front and back plates of the telescope are 47.62 cm (19-inch) aluminum plates with 6.35 (1/4-inch) thickness, that are fixed inside the tube with 6 brackets. The plates diameter is slightly smaller than the inner diameter of the tube to have sliding fit. Having the plates inside the tube allows to have some space at the front and back of the tube, which acts like a hood to block stray light from entering the lens, as well as to create a traveling range to adjust the distance between the plates. The main challenge of fixing the plates in the tube is having them completely parallel, since any misalignments could result in having an aberrated image. In addition, drilling holes at both ends of the tube with the same spacing and distance from the edges is quite challenging and can not be done with high accuracy in the machine shop. As a solution we used 4 rods with the same lengths to connect the two plates together to approve the parallelism. The rods are fixed at the front plate and then the length of them can be adjusted with the spacers at the back. A set of 25 mm, 15 mm, 5 mm, 3 mm and 1 mm spacers (Fig. 4.6(c)) are used at the end of each rod to create a minimum distance of 88.1 cm and maximum of 92.6 cm between the plates. Hence, rough alignments can be done by adjusting the back plate considering the focal point position. In the initial design the end plates were set to be 88 cm apart with a focal point about 3.8 cm outside of the tube to facilitate the alignments and detection of the focused image.

Since the telescope is going to be stored and used outdoors, the temperature variation during summer and winter can cause damage, such as stress on the lens or bending the plates. if the rods are tightly fixed, the thermal expansion can deform the end plates. Therefore, we decided to loosen the bolts at the end of the rods (on the back plate) and replace one of the spacers inside the tube with a removable one, so that it lets the rod contract or expand without causing extra pressure on other parts (Fig. 4.6(d)). Once the distance between the plates is set by the rods, they get fixed on the tube by six brackets so the rods can be loosened. Removing the rods could also be an option, but we preferred to avoid it since the plates can rest on rods even if they are not secured by their strong grip.

By assuming aligning the telescope inside the lab at 20°C, at extreme temperatures like -20°C and 40°C, aluminum rods have 1.24 mm contraction and 0.42 mm expansion respectively. So having a removable spacer to provide about 1 mm space after taking it out, solves the problem. We added small magnets on the spacer and a small metal bolt on the rod, so the the spacer does not accidentally fall inside the tube while assembling. There is also an option of attaching strings to the spacers and fixing the end of the strings on the plate, so that in case of falling, they can be taken out easily. Fig. 4.6 shows the rod with spacers.
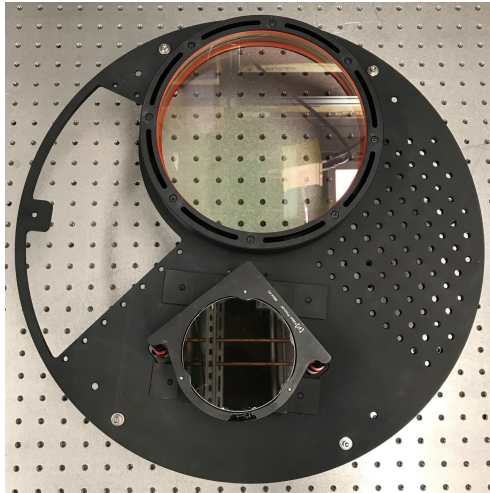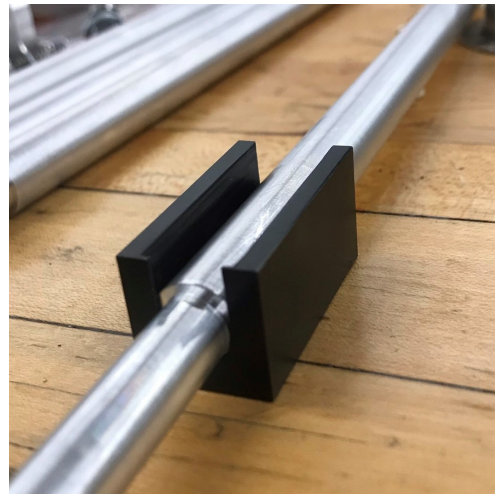
Figure 4.6: (a) Front and (b) back plates of the telescope with the optics mounted on them. The left opening on the front plate and 2 large circular openings on the back plate are meant to allow access to inside the tube. They can be covered by a thin sheet of aluminum later. The smaller circular cut on the back plate is centered at the optical axis of the focal point. (c) Rods and spacers inside the telescope to hold the plates parallel. (d) The removable spacer which creates enough space for thermal expansion after removal.

Front Plate

The front plate is responsible for holding the lens and the 4-inch mirror. As discussed in Sec. 4.2, one part of the cell is screwed into to the plate and the 4-inch mirror base plate is attached under it. Two rectangular openings are considered at the position of the motors to have access to them for manual adjustments. Since other optical setups might be needed near the lens such as the polarization pick-off, we added clear and threaded 1/4-inch holes at one side of the plate and created an opening on the other side to have access to inside the tube. The opening can be covered by a thin sheet of aluminum to block the light and its threaded holes can be used for mounting purposes as well as attaching the sheet to the plate. In addition, there is a pair of small holes under the lens which is perfectly matched with the ones on the back plate. This holes are considered to test the angular mismatch of the plates. If the plates are positioned properly, a beam light sending through one of the holes on the front plate must goes through a hole on the back plate and if using a corner cube and sending it back through the second hole of the back plate, it must be detected on the second hole of the front plate. As a result, one can confirm that the plates are not rotated relative to each other.

Back Plate

The 6-inch mirror mount is attached to the back plate, so there is a circular opening with 16.25 cm diameter at the place of the mount, to create enough room for the motors as well as making them accessible from outside of the tube. The small power hub board of the motors are also mounted near them to avoid having long wires. There is a 6.35 cm (2.5-inch) opening, centered at the optical axis of the focal point, which is used for mounting the focuser and the black tube to block stray-light-blocking tube. Two more openings with 11.17 cm diameter is considered on the plate to allow using both hands inside the tube if needed. The openings are covered with thin sheets of aluminum. Since only 4 of the threaded holes around them are enough to hold the cover, other holes can be used for mounting purposes.

Focuser and Telescope Mounting

As focusers we consider the "Moonlite 2.5-inch motorized focuser" and "Quattro 250 carbon fibre OTA 2-inch linear focuser" to be used with the telescope. Therefore, two different adaptors are designed to mount them on the back plate. To block the stray light near the focal point, a 13.33 long tube with 6.35 inner diameter is built which can be attached
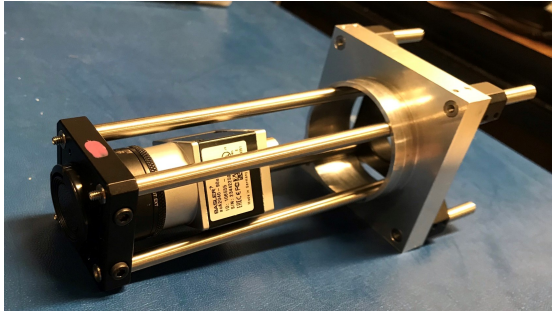
(a)
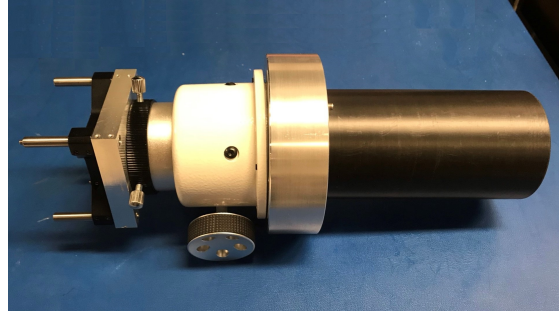
(b)
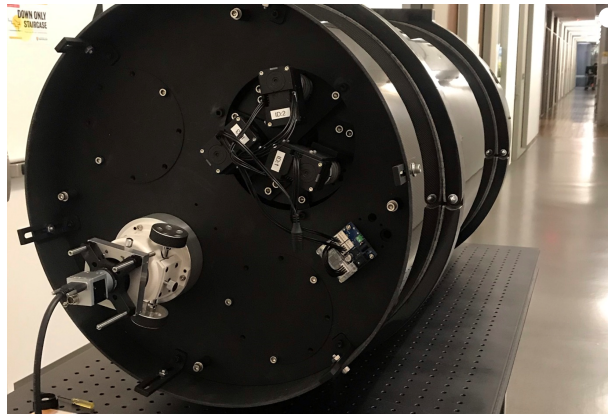
(c)

Figure 4.7: (a) A cage system with an adaptor plate to allow placing either the camera or the fibre at the focal point of the telescope. (b) The two inch linear focuser attached to the black stray-light-blocking tube by the adaptor in between. The aluminum adapter is fixed on the lid from the right side and holds the focuser from the other side. The cage system is fixed inside the focuser tube. (c) Mounting of the focuser with the camera on the back plate of the telescope.

to the focusor adaptors and insert the tube from outside. The Moonlite focuser adaptor flange gets fixed inside the mentioned tube with three set screws and then the tube can be mounted on the plate using three 8-32 bolts. The other focuser adapter has the option to be used with or without the stray-light-blocking tube and can be mounted on the plate using the same three holes. To observe the beam at focal point in star test and for wavefront characterization tests which requires having a fibre at the focal point, we used a cage system to be able to mount either a camera or a fibre inside the focuser tube (Fig. 4.7).

The whole telescope is tightly fixed inside 2 tube rings which have two 1/4" clear holes at one side and three threaded holes at the other side. The rings are mounted on an optical breadboard using the two clear holes, so the threaded ones on the opposite side can be used for mounting purposes. The APT system is also fixed on the breadboard at the back of the telescope using a dovetail and brackets which enables adjusting the APT position and fixing it on the board. "ASA Direct Drive Mount (DDM100 Standard)" with load capacity of 65 kg will be used as the mount of the telescope. Therefore, the breadboard with the telescope and APT system on it, will be fixed on the mount and used for future experiments.

4.2 Coating of Interior Parts

Reflections of the stray light from the interior parts of the telescope can interfere with the quantum and beacon signal and perturb the beam. Therefore, it is crucial to insure the interior parts do not have high reflectivity at visible and NIR wavelengths. An incident beam on a surface can experience absorption, transmission, and reflection. Since the parts are made from aluminium, transmission is negligible and reflection must be minimized. Ideally, the stray light must be absorbed instead of reflected. Moreover, absorption is only possible at specific wavelengths which have the enough energy to cause electronic transitions in the material. Therefore, wavelengths larger than 700 nm can not excite an electron to change its state, and as a result, the light would not be absorbed. Two types of reflection occur to the incident light: specular reflection and diffuse reflection. Specular reflection is a mirror-like reflection that happens to optically smooth surfaces. Diffuse reflection is related to the powdered samples, where the light penetrates through the powder and gets reflected off of the grains' surface. The smaller the particles are, the more reflection happens and the less is absorbed, since scattering coefficient is reversely proportional to the particle size.[24]

The common solution for reducing the reflection induced by stray light is to use oxide coating on the surface of the metal. Visible light (400-700 nm) gets absorbed although IR
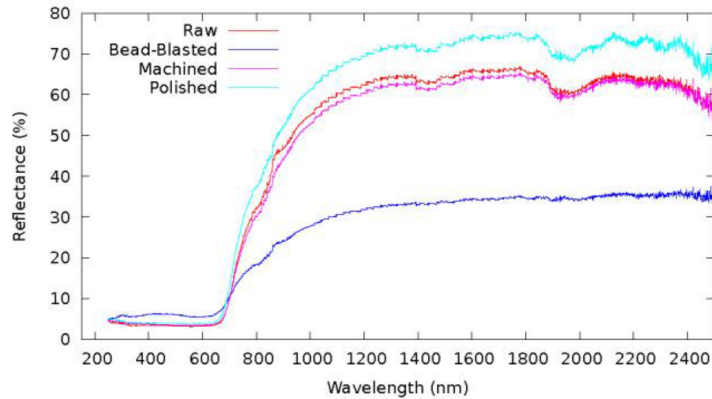
Figure 4.8: Total reflection of black anodized 6061 aluminum [49]

light goes through the coated layer and gets reflected from the metal surface underneath, due to its longer wavelength. Paint can also be used as a coating layer. The pigments of paint define the absorptive and scattering properties of the used color. If there is more absorption of visible light than scattering, then the pigment is seen as a black pigment and the opposite occurs to white pigment. Therefore, a black anodization can be effective in minimizing the reflection of visible light from the metal surfaces and having large grains can mitigate the IR reflection. [24]

Fig. 4.8 is a plot of the total reflection for an aluminum surface with black anodized coating. At visible light wavelengths, the oxide and the black colour pigments result in low reflection while the reflection is increased significantly at NIR. The plot shows the behaviour of different surface types, such as a polished surface or a raw one. The bead-blasted surface has the least reflection at NIR region. The measurements and comparisons done in this paper [49] suggest that having hard-coat (non-dyed) anodization of aluminum is the best surface treatment to reduce the reflection at IR. Moreover, anodization of aluminum increases its durability and makes it resistant to corrosion. Further, raw aluminum does not support dyeing, and anodizing the metal is a simple solution that allows for adding colours.

In conclusion, first we sandblasted [1] all inner parts of the telescope, such as the plates, rods, spacers, mirror base plates, lens cell, and bolts [2]. Then, we used black hard-coat anodization to minimize the reflection at both visible and NIR wavelengths.

---

[1]Sandblasting is similar to bead-blasting, with the difference that it is harsher on the metal surface.

[2]It is recommended not to sandblast the threaded areas. If so, it is important to clean them thoroughly, since particles of sand can be stuck in the threads and damage them.

No.	Parts	Diameter (mm)	Thickness (mm)	Weight (kg)	Material/ Substrate	Coating	Surface irregularity	Model #	Company
OP1	Doublet Lens	210+0/-0.5mm	46±0.4mm	5.24	H-LAF2, H-ZF5	6 layers of Ta_2O_5 and SiO_2	$\lambda/4$	Customized	Hyperion Optics
OP2	Flat Mirror 1	152.40+ 0.0/-1.02mm	25.40±2.0mm	1.95	ZERODUR	Protected Silver	$\lambda/20$	48-119-577	Edmund Optics
OP3	Flat Mirror 2	101.60+0.0/-1.02mm	19.10±1.5mm	0.75	ZERODUR	Protected Silver	$\lambda/20$	48-118-577	Edmund Optics

Table 4.1: List of all the optical parts of the telescope

4.3 Manufactured and Purchased Parts

Optical and mechanical parts of the telescope are designed and optimized for this project. So we tried to find the commercial options as much as possible and designed and built the rest. Fig. 4.1 shows the CAD model of the entire system designed in Solidworks. All the custom-designed mechanical parts were built at the University of Waterloo science machine-shop. The total weight of the telescope is approximately 30 kg which is half the maximum payload of the ASA mount. This amount excludes the weight of APT system and the breadboard used for mounting the telescope.

The purchased parts were carefully chosen from vendors around the world to maximize the performance of the telescope. The total cost was 30k USD which is lower than the price of similar customized telescopes. Table 4.1 and Table 4.2 provide the detailed information on all optical and mechanical parts.

No.	Parts	Features	Material	Weight (kg)	Model #	Company
1	Telescope tube	ID: 476.25mm Wall: 3.81mm Length: 1,041.4mm Flat black interior coating	Carbon fibre	8.84	Customized	Carbon Scope Tubes
2	Front plate	Dia: 476.25mm Thickness: 6.35mm Hard black anodized	Aluminum	1.81	Customized	University machine-shop
3	Back plate	Dia: 476.25mm Thickness: 6.35mm Hard black anodized	Aluminum	2.27	Customized	University machine-shop
4	Rods	Dia:9.52mm Length: 93.83mm Hard black anodized	Aluminum	1.13	Customized	University machine-shop
5	Telescope rings	For 482.6mm OD tubes Two 1/4" clear holes at one side and three threaded holes at the other side	Die-cast aluminum lined with felt	3	Parallax-19" OD Tube Rings (Meade DS16A, 16" Starfinder)	Woodland Hills Camera Telescopes
6	Lens cell	OD:235.20mm ID:209.98mm Hard black anodized	Aluminum	0.76	Customized	University machine-shop
7	Stray light tube	ID:63.5mm Length nside the tube: 133.35mm	Acetal	0.17	Customized	University machine-shop
8	2.5" motorized focuser (Moonlite) adaptor	-	Acetal	0.022	Customized	University machine-shop
9	2" linear focuser adaptor	-	Aluminum	0.374	Customized	University machine-shop

10	Flexible shaft coupling (×3)	Shaft diameter: 5/16" × 5/16" length: 50.8mm (2") Angular misalignment: 5°	Aluminum	0.0865	6208K583	McMASTER-CARR
11	Dynamixel motors (×3)	Dimension: 33.5×58.5×44mm Stall torque: 10.0 N.m (at 11.1 V, 4.2 A) 10.6 N.m (at 12.0 V, 4.4 A) 12.9 N.m (at 14.8 V, 5.5 A) Backlash: 0.25° Resolution: 4096 [puls/rev]	-	0.168	XM540-W270-R	Robotis
12	Dynamixel motors circuit board	U2D2 and its power hub board Dimension: 48×57 Operating voltage: 3.5V-24.0V Max current: 10.0A U2D2 Baud rate: 9600-6Mbps	-	0.350	Dynamixel starter set	Robotis
13	6" mirror mount	Suitable for 6" mirror with 16.51mm to 31.75mm thickness	Black anodized Aluminum	0.784	AZ-6	Aurora precision
14	4" motorized mirror mount	Suitable for 4" (101.6mm) mirror. Resolution: $0.7\mu m$ Angular range: ± 3.5°	Black anodized Aluminum	0.35	8824-AC	Newport
15	Mirror 1 base plate	Hard black anodized	Aluminum	0.165	Customized	University machine-shop
16	Mirror 2 base plate	Hard black anodized	Aluminum	0.200	Customized	University machine-shop
17-22	Other small parts such as, 17) Motor brackets 18) Motors shafts 19) plates' brackets 20) plates' covers 21) Spacers 22) Bolts	Hard black anodized	Aluminum	0.650	Customized	University machine-shop
23	High-temperature soft silicone O-rings	ID: 202.79mm OD: 209.85mm Hardness: Durometer 50A (soft)	Silicone Rubber	-	1173N506	McMASTER-CARR

Table 4.2: List of all the mechanical parts of the telescope
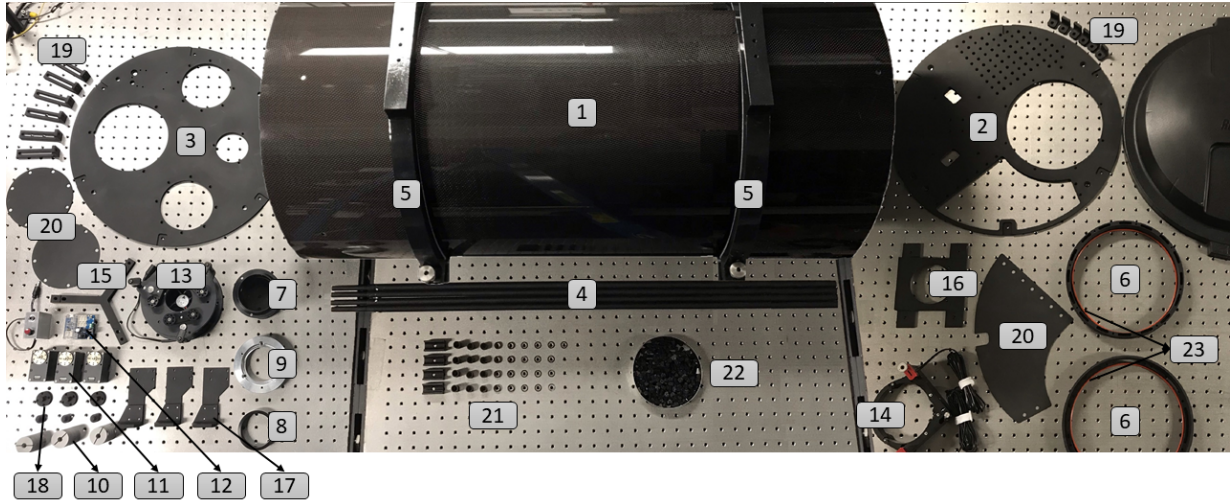
(a)
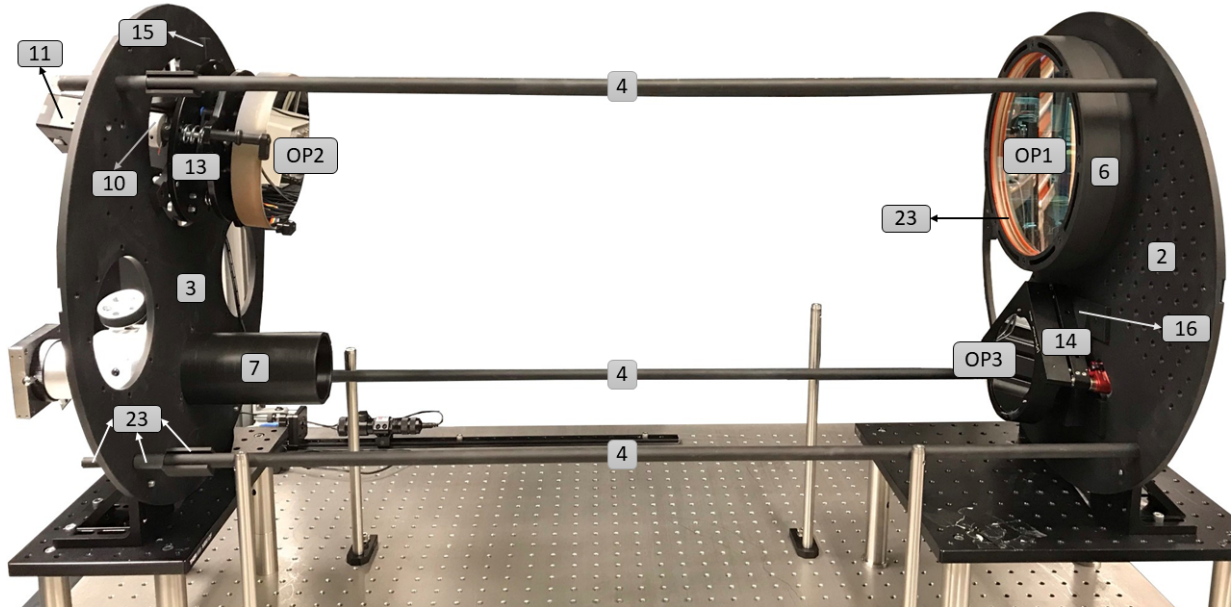
(b)

Figure 4.9: (a) Mechanical parts of the telescope; (b) Assembled telescope outside of its tube for initial alignments. All parts are labelled based on the numbers in Table 4.1 and 4.2.
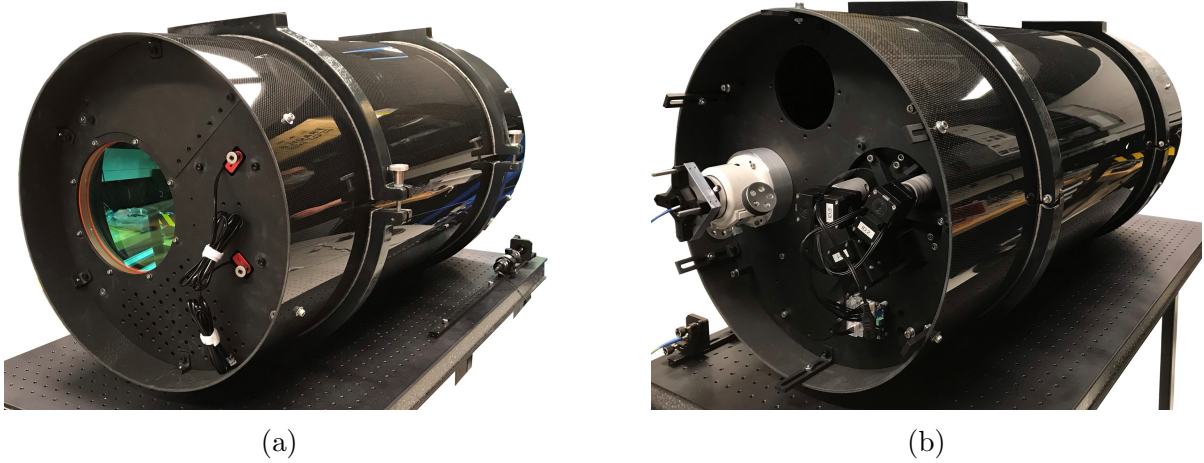
Figure 4.10: (a) Front and (b) back view of the assembled telescope

4.4 Assembly and Alignments

Initially, a 24.13 cm (9.5-inch) tube ring was used to hold the lens for characterization tests discussed in Chapter 5. We used foam inside the ring to secure the lens and screwed the ring to a breadboard to be able to take measurements on the lens. Upon approving the performance of the lens through various tests, as well as having all required parts purchased and built, we began to assemble the telescope.

As previously mentioned, the 6-inch mirror had to be glued to the mirror mount, so first we mounted the Dynamixel motors and the couplings on the mount (as discussed in Section 4.1.2: Mirror 1), then, we added the mirror base plate and used a few spacers to compensate for the 8° tilting. Therefore, the mirror was positioned horizontally on the mount. We applied "DowSIL-RTV Sealant-732" epoxy on the designated areas on the mount. The mirror was carefully placed in a still position for 48 hours to be fully cured. Then the mirror base plate was fixed on the back plate. On the other side the front plate had to be ready before mounting on the tube. To safely add the lens to the plate, we fixed the front plate on the optical table using pillar posts, so that the surface of the lens does not touch the table. Then, part A was screwed into the plate and one of the rubber O-rings was placed inside it. The lens was carefully moved from the ring to the lens cell. Before clamping the lens between two parts, the rubber O-ring was glued to part B using a super glue, to avoid falling or touching the lens. We applied the super glue to the sides of the 4 inch mirror as well, to ensure it is fully secured inside the mount. When the glue was

cured, the 4 inch mirror mount got attached to the plate and then part B of the lens cell was screwed down to part A. While tightening the bolts around the lens, it is crucial to use the same amount of torque on all of them, and also to not over-tighten them to avoid birefringence effects which was later tested and verified by the polarization measurement Sec. 5.3.

After mounting the optical elements on the plates, we connected them by the rods outside of the tube to align the mirrors (Fig. 4.9(b)). To follow a beam and calibrate the angles of the mirrors by tip-tilting, we placed a green laser near the focal point using the 2-inch linear focuser. By observing the beam, it was expected to have the beam at the center of the lens or at least with no horizontal offset, which was corrected later by the mirror 1 motors. Also, by looking at the transmitted beam size at different distances from the lens, we set the fibre approximately at the focal point. As a result, the beam size remained the same as getting further from the telescope. In addition, we added a collimator in front of the fibre to observe a narrow collimated beam on the mirrors and the lens, to center the beam with the optical elements. Due to the mismatch of the fibre f-number and the lens, as well as the low accuracy of the manual alignments, further tests were required to do fine adjustments. Therefore, Wavefront measurement was taken to determine the position of the focal point of the telescope and detect the wavefront error of the transmitted beam. To identify the tilting or centering error of the mirrors, observing the image of an object in the infinity was required which was studied in a star test with an artificial star inside the building. The details of the wavefront measurement test and star test are discussed in Chapter 5.

After assembling the parts outside of the tube to verify the alignments and polarization preservation by wavefront and polarization measurements, the telescope was ready to be assembled inside the tube. Although the plates were built to have a sliding fit to the tube, it was much harder to slide them in a horizontal tube due to friction and tilting of the plate. Therefore, we assembled the parts in an upward position and applied Loctite on the bolts of the lens cell to avoid loosening of the bolts in future.

Since the ASA mount was not available, we used a 100X50 cm optical breadboard on a cart to carry the telescope for different tests. The tube rings screwed to the breadboard were responsible to hold the tube. As a result, the telescope was successfully assembled and safely placed on the cart. As the setup is going to be stored either outside or inside the lab for a long time, it is important to save the optics from contamination. Therefore, we considered a dome shape lid on the tube to protect the lens, as well as, allowing for mounting other optical components on the plate in future. Fig 4.10 shows the fully assembled telescope.

The indoor star test results (Section 5.1) indicated no significant aberrations in the image, so we are looking forward to repeating the test with real stars to escalate the performance of the telescope by more fine adjustments and calibrations. The optimal orientation of the telescope has not been investigated yet which can be determined by Finite Element Analysis (FEA). Moreover, keeping the system thermally stable and having a full grasp of temperature variation impacts on each part is planed as the future work.

Chapter 5

System Characterization

In this chapter we present the results from the performance tests of the lens and the entire telescope assembly. In a star test, we observed the image of a point source to study the optical aberrations that occur due to the lens. This test was repeated for a combination of the lens and folding mirrors, in order to check the alignments of the optical parts. Moreover, we used a collimation test to find the focal point and obtain a collimated beam at the output of the lens. We were able to measure the divergence angle of the beam and characterize the beam wavefront to confirm the surface irregularity determined by the initial design. Finally, we used the polarization test, to verify the polarization maintenance of the lens. Also, we measured the polarization characterization of the folding mirrors under different incident angles and validated our measurement approach by comparing the results with the theory.

5.1 Star Test

Observing the Airy disk of a point object, reveals any distortions that occur to the wavefront due to the optical aberrations of the lens or the turbulent atmosphere. If an object is far enough from an optical element to be effectively considered a *point* source, then the detected image is very close to the diffraction pattern. Since the image must be quite symmetric relative to the optical axis, any asymmetry can indicate an aberration. Considering the on-axis Airy disk, any flared pattern can represent a tilted element in the system, or a cruciform of the image can be a result of axial astigmatism due to index of refraction inhomogeneity or a decentered/tilted element. Moreover the state of correction of the chromatic aberration and spherical aberration can be determined by the image pattern. For

a well-corrected lens, the diffraction pattern does not appear neither in the best focused image nor in the in/out of focus image. However, if the rings show up inside the focus and get blurry outside, it is concluded that the spherical aberration is under-corrected[1]. The reverse corresponds to the over-corrected[2] one. To distinguish a chromatically corrected lens which has a residual secondary spectrum, the image appears yellow-green color in the center with a blue or purple halo around it, while if the chromatic aberration is under-corrected, the focused pattern shows a blue center with a red outer flare. Off-axis patterns are more complicated to be analysed since they are usually a complex combination of several aberrations [78]. Therefore, a star test can be used as a diagnostic tool to study the impacts of optics imperfections, misalignment or the turbulent atmosphere on the detected image.

One approach to performing a star test is using an artificial light source at a certain distance from the telescope. The artificial source is a point like emitter that is stationary, and conventionally allows for controlling the brightness and applying filters to pick a specific wavelength for the test. In addition, since it is fixed on the ground, it does not require tracking and it is much less affected by the atmosphere turbulence. However, because the test is performed on the ground, the telescope needs to point horizontally towards the light source, which might not be convenient for some types of telescope mounts, such as Dobsonian telescopes. Two important variables in using an artificial source are its diameter and the distance of the source from the telescope. A light source can be considered as a *point* source if its diameter is smaller than the resolution of the telescope [82][78]. H. R. Suiter listed the size of a pinhole or a reflective sphere that corresponds to different sizes of reflective telescopes in his book [82]. To obtain the minimum distance required to avoid $\lambda/4$ spherical over-correction (which happens if the light source is close to the telescope), he introduced a parameter as,

$$M = 336\frac{D}{(F)^3}, \tag{5.1}$$

Where D is the telescope aperture diameter in inch and F is the f-number of the telescope. He suggested the distance must be $M \times$ focal length, and recommended to double or even triple it. However, this equation is for Newtonian reflectors with respectively small mirrors but it still can be used as a preliminary estimate for other configurations of reflectors. However, Eq. 5.1 does not work for refractors. Usually 10 or 20 times of the focal length of apochromatic or achromatic refractors can be considered as the minimum distance. [82]

Our custom-designed telescope has an 8-inch aperture with an effective focal length of 2.438 m. Therefore, The minimum distance between the artificial star and our telescope

---

[1]The aberration has a negative sign.
[2]The aberration has a positive sign.

must be $20\times2.438 = 48.76$ m. As recommended in [82], to avoid vignetting from the baffles, 97.52 m must be taken into account. Also, since we are using an optical fibre with NA=0.14 and mode field diameter (MFD) of 5 μm, it fulfills the diameter condition required for a point source. Nonetheless, the maximum distance we could set between the telescope and the point source was about 55 m, which is not yet at the effective infinity for the telescope. However, we were able to compare our measurements by modelling the 5 μm object at 55 m distance from the lens using Zemax. We performed the test first with just the lens held fixed by a ring (Fig. 5.1), and again after assembling the telescope, which included the lens and two folding mirrors.

5.1.1 Lens Star Test

Experimental Setup

Initially, the star test was done only with the lens to verify its quality after it was received from the manufacturer by observing the image of our "artificial star" at the focal point. We fixed the primary lens inside a 9.5-inch tube ring and placed it on a high precision hexapod (HXP50-MECA, Newport) (Fig. 5.1(a)). The hexapod provided six degrees of freedom (x, y, z, pitch, roll, and yaw) which allowed us to move and tilt the lens with 0.2 μm and 0.2 mdeg precision, so that by looking at the image we could determine the best orientation of the lens for the least aberrated image. In addition, we were able to tilt the lens to see the behaviour of the spot within the field of view. Fig. 5.1(b) shows the light source which includes a supercontinuum laser and sets of filters to generate a beam at 780 nm, 980 nm, and 1550 nm separately. The supercontinuum laser covers a broad range of wavelengths so we used a long-pass, a short-pass, and a band-pass filter to attain the desired wavelengths. Moreover, since the output of the supercontinuum laser is a collimated narrow beam, we coupled it to a PM fibre to have a diverging beam, which behaves similarly to a star. The fibre was mounted on 3 translation stages to have the degrees of freedom to move along x, y and z axes. Our point source was located at the furthest distance from the lens, that we could have inside the building. However this was still shorter than the distance required to create the artificial star scenario. It is worth mentioning that to increase the path that the beam is traveling to reach the telescope, one solution is adding folding mirrors so that the object could be considered much further to the lens. Nevertheless, adding extra optics could result in additional wavefront distortion such that we could not isolate the impact of the lens on the beam. Therefore, we had to consider having a point source at a certain distance from the lens and simulate it using Zemax, to compare the results. On the other side of the lens, we had a camera at the focal length to detect the spot. We used NIR-
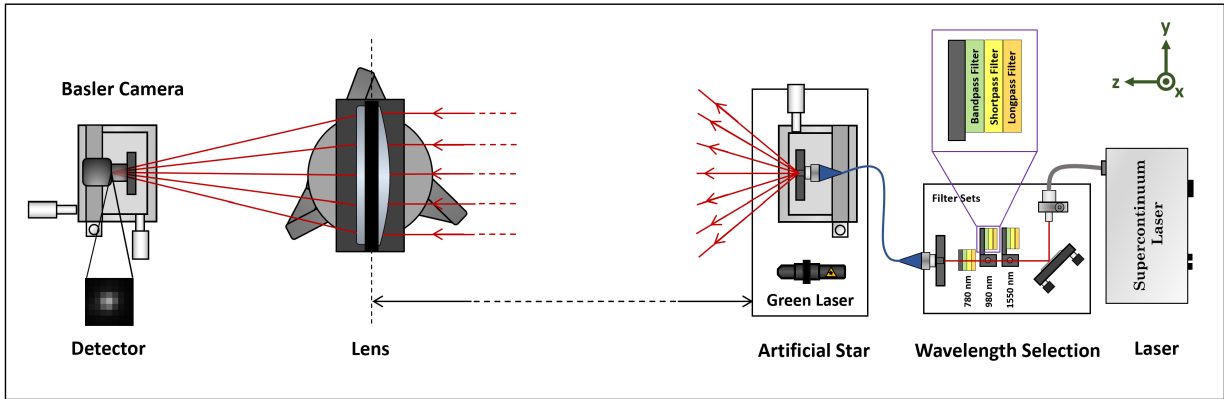
(a)
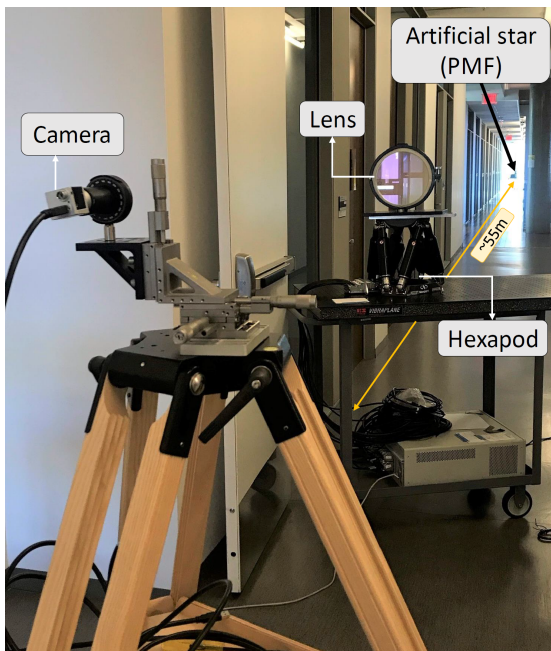
(b)
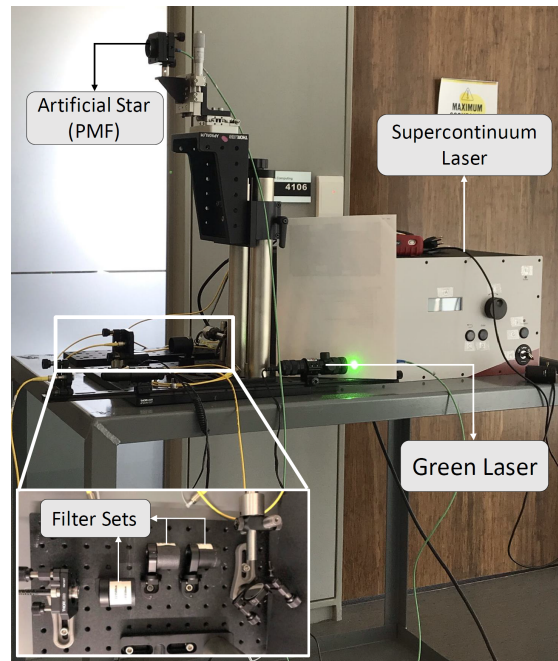
(c)

Figure 5.1: (a) Schematic diagram of the star test experiment; The lens is mounted on a hexapod to allow for small linear and angular alignments. A PM fibre is used as an artificial star, which has one of the 780 nm, 980 nm and 1550 nm wavelengths, based on the selected filter set. If the star is far enough from the lens and the setup is aligned perfectly, it is expected to detect the aberration-free image of the star at the focal point of the lens. (b) and (c) show the experimental setup.

enhanced CMOS Camera (Basler acA2040-90umNIR) to record the spots for 780 nm and 980 nm beam. However, we had to use an InGaAs camera (NIT-WiDy SenS 640M-StE) to detect 1550 nm. Either camera was mounted on a 3-axis translation stage on a tripod to allow smooth translations while maintaining the stability during the test.

Table 5.4 shows the information of all the parts used in this experiment.

Experiment and Results

We performed three tests with the primary lens and studied the spot on the camera:

1. Finding and observing the focused spot at the focal point for the three wavelengths.

2. Testing $\pm 0.1°$ and $\pm 0.2°$ yaw, pitch and roll for 780 nm and 980 nm.

3. Moving the camera for ± 5 mm along the optical axis to observe the through-focus image.

Since our wavelengths are not in the visible range, a green laser was used for visually aligning the source with the lens and camera. we shined the green laser from our source setup which was about 55 m far from the lens, and placed the camera such as the green light's focus falls on its sensor. We then switched to 780 nm light and found the image on the camera. The intensity of the observed image was fluctuating and the centroid was slightly moving around, which could be the result of air turbulence, vibration of the building or fluctuations of the pulsed laser. Therefore, for the analysis each measurement point is an average over 20 frames.

At first, the spot had a coma-shaped pattern which was fixed by tilting the lens in correct directions via the hexapod. Since the manufactured diameter of the lens is 6.79 mm larger than the clear aperture considered in Zemax and also to remove the stray lights we added an 8-inch mask in front of the lens and kept it for the rest of the tests to be consistent with Zemax simulation results. Fig. 5.4a to 5.4d and 5.5e to 5.4h, respectively show the image of the focused spot for 780 nm and 980 nm and contour plots of the intensity after background noise subtraction. The pixel value of Basler camera is linearly dependent on the intensity, so we directly used the pixel values as equivalent samples of the beam intensity for our data analysis. Before each measurement we took 20 frames of dark frames and subtracted the average value from each data frame before plotting. Then we considered 2 cross sections of the beam along the x and y directions and plotted the variation of the intensity. Finally, we fit a Gaussian curve on the intensity profiles, and

determined how close the results represented a Gaussian beam and also determined the $1/e^2$ radius[3] for each spot to compare with the theoretical Airy radius. We reported the average of the x and y results as the Airy diameter of the beam at the focal point.

The Airy diameter $(2 \times 1.22(\lambda f/D))$ is theoretically expected to be 23.9 μm, 30.02 μm and 47.46 μm respectively at 780 nm, 980 nm and 1550 nm for an 8-inch lens as defined by diffraction theory. As summarized in Table 5.1 there is 3.87% relative difference on average between the measured diameters and the theoretical numbers, while the measured distances from the image plane to the lens were in perfect agreement with the numbers obtained using Zemax (less than 1% relative error). Fig. 5.2 shows an example of one of the measurements. At each wavelength the photo of the beam was captured (Fig. 5.2.a) and plotted (Fig. 5.2.b). Then two orthogonal cross sections of the beam were considered to be plotted and fitted with a Gaussian curve to obtain the $1/e^2$ beam waist and also verify the Gaussian behaviour of the beam. In order to detect 1550 nm we changed the camera to InGaAs with a pixel size of 15 μm. Unfortunately, due to the large pixel size, the camera did not have the required subpixel accuracy to resolve the image and we were not able to measure 1550 nm spot size to verify it with the simulations.

Data set	Airy diameter (μm)			Image plane distance (cm)		
	Zemax	Measurement	Error	Zemax	Measurement	Error
780nm	23.90	24.18±0.28	1.17 %	252.37	254.00	0.64%
780nm with mask	23.90	25.76± 0.36	7.78 %	252.37	254.00	0.64%
980nm	30.02	29.08±0.11	3.13 %	251.64	253.40	0.69%
980nm with mask	30.02	31.05± 0.65	3.43 %	251.64	253.40	0.69%
1550nm	47.46	NA	NA	252.19	253.00	0.32%

Table 5.1: Star test results of the lens for the best focused image at 780nm, 980nm and 1550nm.

---

[3]"$1/e^2$ width", refers to the distance between two points on the intensity profile, that their intensity is $1/e^2$ times the maximum value
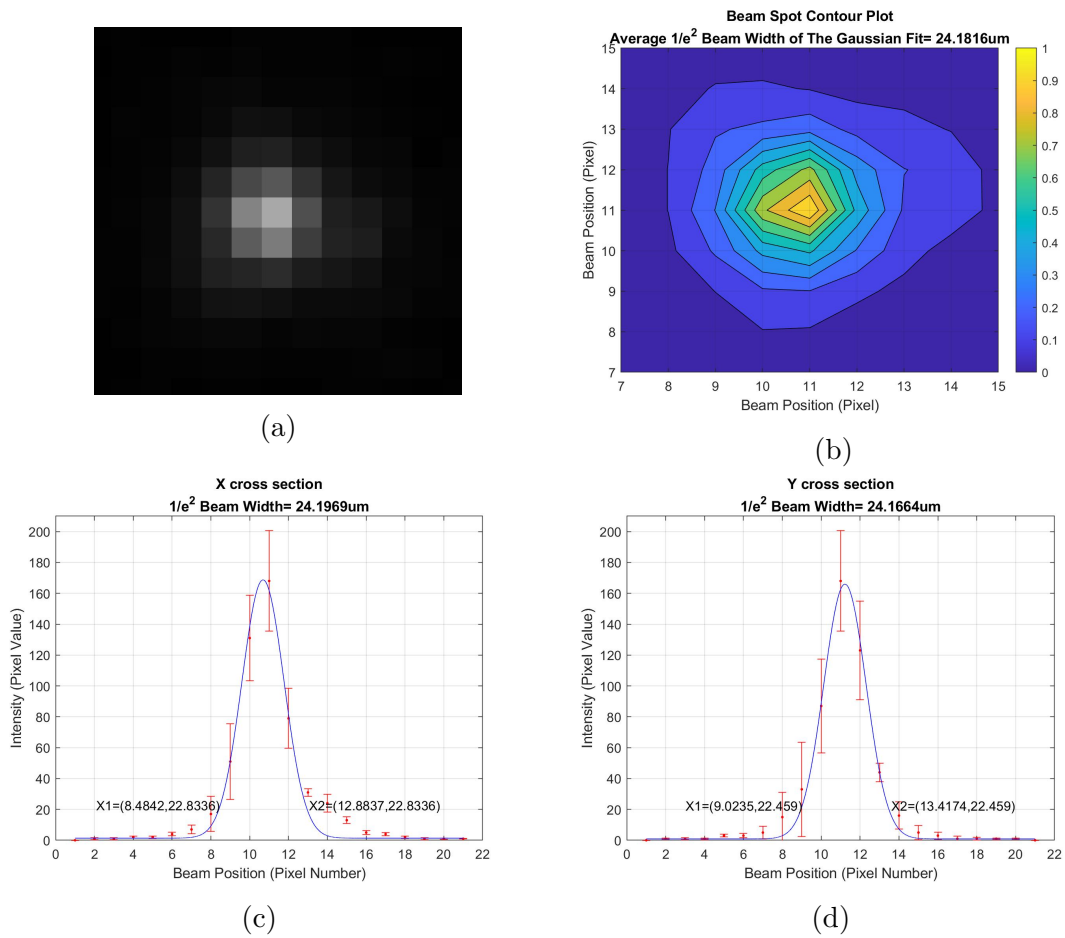
Figure 5.2: Star test of the lens at 780 nm without the 8-inch mask. (a) Image of the focused beam on the camera (pixel size is 5.5 μm). (b) The average beam size and a normalized contour plot of the image. Intensity curve over a cross section of the beam along (c) x and (d) y axis to obtain the $1/e^2$ beam width.

Next step, we looked at the through-focus[4] image to verify the focal point and compare the behaviour of the beam with Zemax spot diagram. Fig. 5.3, Fig. 5.4 and Fig. 5.5 show the spot image traveling for ± 5 mm from the focal point at 3 wavelengths. The results confirmed that the camera was at the focal point to within 1 mm accuracy. However, the distance from the lens was approximated, since the sensor of the camera is not located at the edge of its opening and the location of the sensor had to be estimated. In addition, the through-focus image shows displacement of the spot while moving the camera back and forth, which could be a result of the misalignment between the two axes of each the camera and lens. These systematic errors of the setup had been mitigated after assembling the telescope and repeating the star test.

---

[4]Through-focus image is referred to observing the blurry beam spot that goes to the focus and gets blurry again on the optical axis.
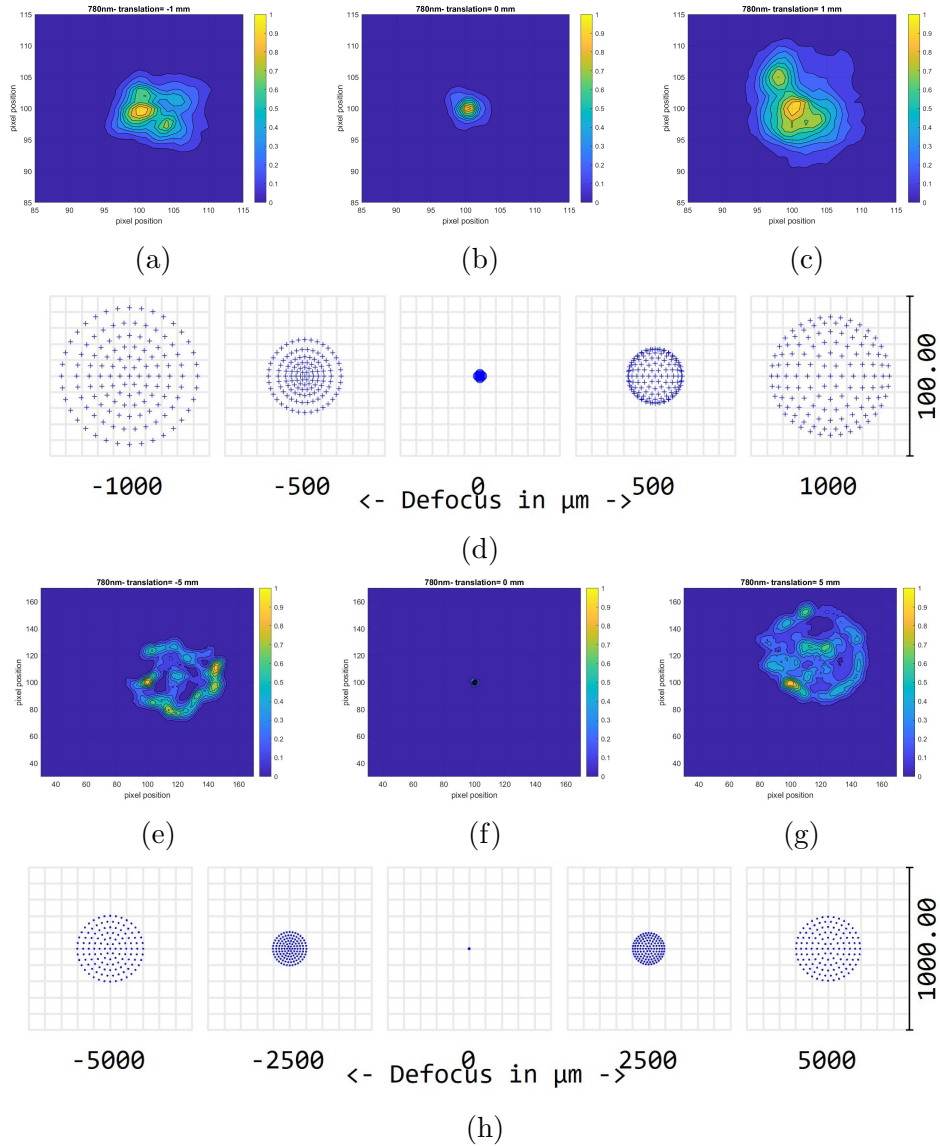
Figure 5.3: Measured through-focus beam spots at 780 nm compared with the spot images modeled with Zemax; (b) and (f) show the focused image. The camera is shifted for 1 mm along the optical axis in opposite directions to obtain the out-of-focus image (a) and (c). Then larger translation of 5 mm was applied to observe the behaviour of the beam ((e) and (g)). (h) and (d) show the Zemax spot diagrams of the beam spot for the related translations. Due to the small size of the Airy disk and poor alignments, the difference in the distribution of the intensity before and after the focal point is not noticeable when compared with simulation results.
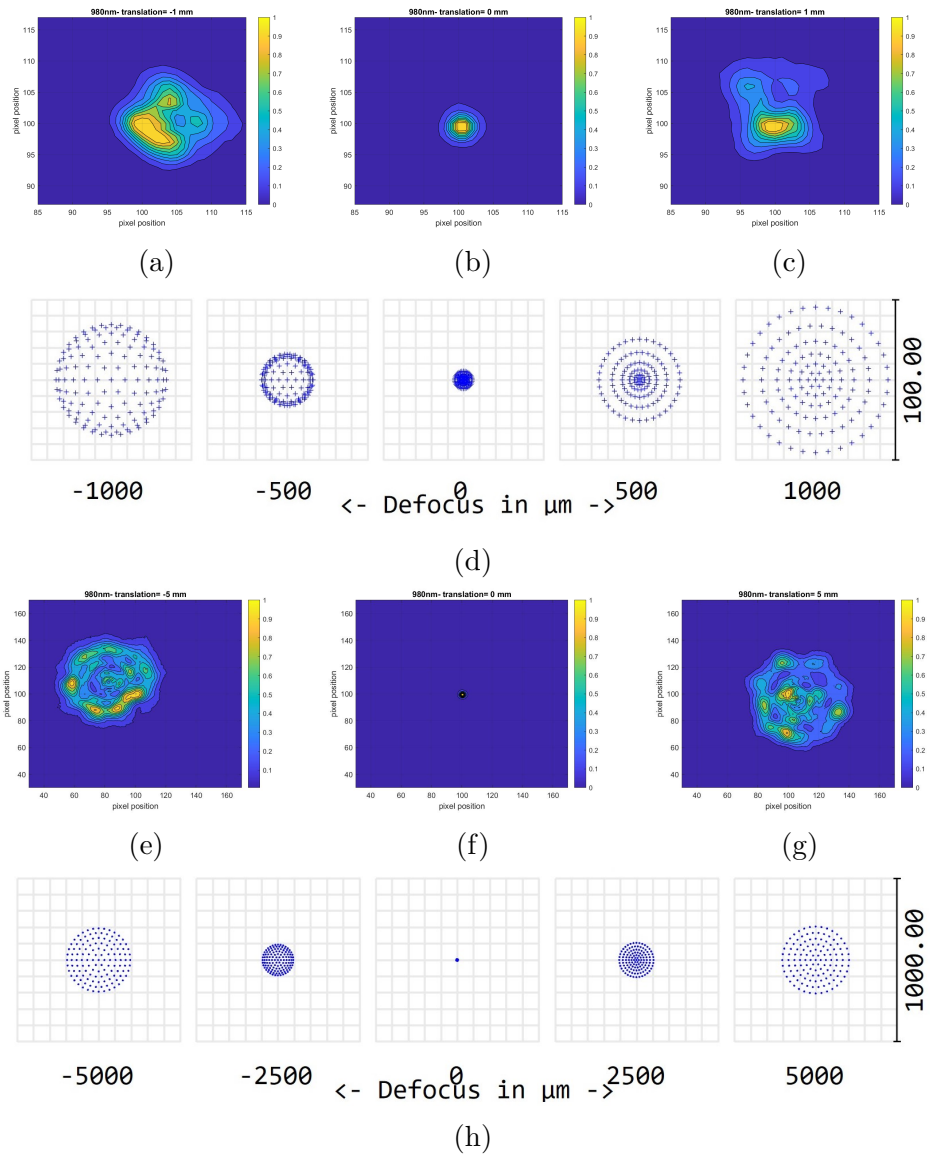
Figure 5.4: Measured through-focus beam spots at 980 nm compared with the spot images modeled with Zemax.; (b) and (f) show the focused image. The camera is shifted for 1 mm along the optical axis in opposite directions to obtain the out-of-focus image (a) and (c). Then larger translation of 5 mm was applied to observe the behaviour of the beam ((e) and (g)). (h) and (d) show the Zemax spot diagrams of the beam spot for the related translations. From -5 mm to +5 mm, the beam keeps its circular shape and the higher intensity moves from the edges to the center of the spot. This pattern can also be detected in the measurements.

103
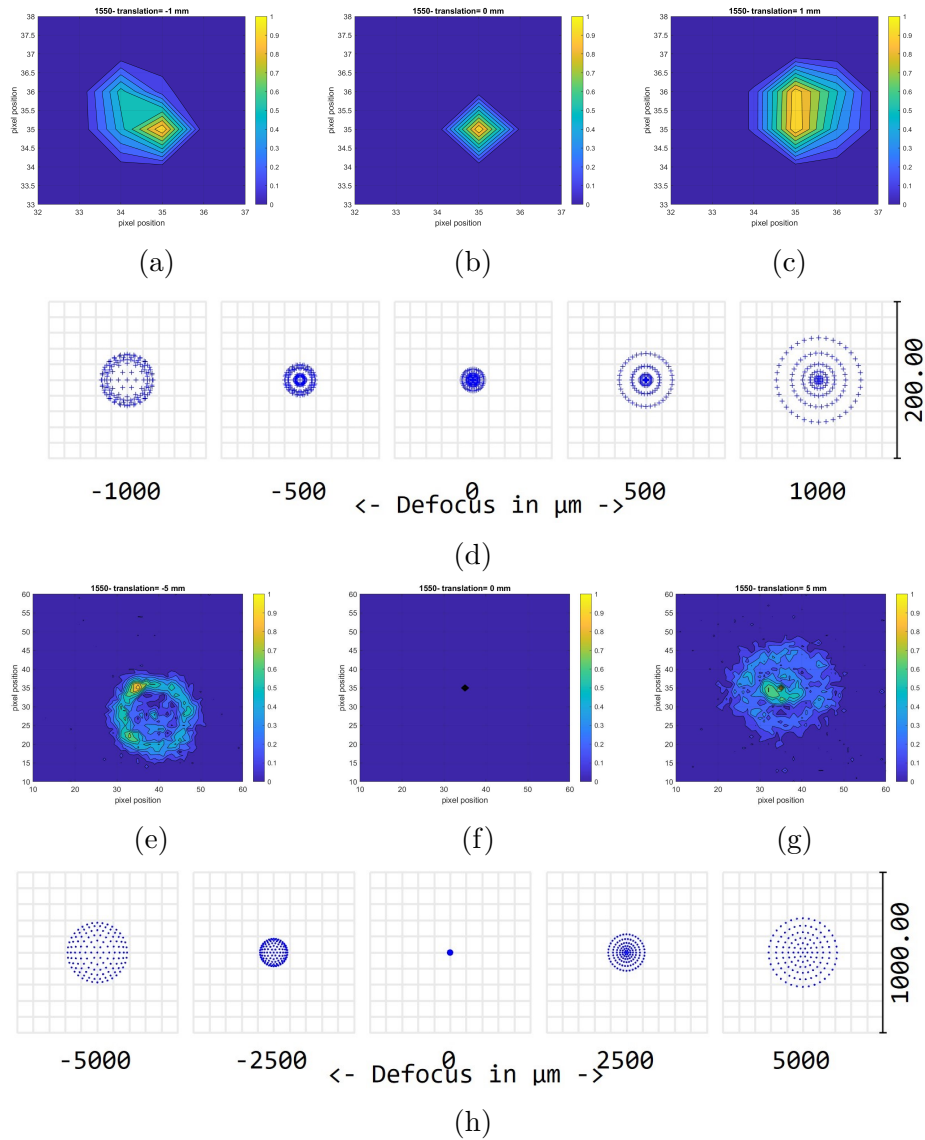
Figure 5.5: Measured through-focus beam spots at 1550 nm compared with the spot images modeled with Zemax.; (b) and (f) show the focused image. The camera is shifted for 1 mm along the optical axis in opposite directions to obtain the out-of-focus image (a) and (c). Then larger translation of 5 mm was applied to observe the behaviour of the beam ((e) and (g)). (h) and (d) show the Zemax spot diagrams of the beam spot for the related translations. The difference in the distribution of the intensity before and after focus is quite noticeable since the Airy disk is larger than the two other wavelengths and the change in the shape of the beam spot can be observed in the measured range. The results are agree well with the Zemax spot diagrams.

The final set of measurement was studying the impacts of a tilted lens on the image. As mentioned before, the field of view of the telescope is ± 470 μrad, so the beam must remain non-aberrated within $\pm 0.057°$. For calibration and alignment purposes, we considered twice this angle and corrected the lens for $\pm 0.1°$ field angle. Fig. 5.6 shows the results of $\pm 0.1°$ tilting around y axis, compared with the point spread function plot from Zemax simulation. In the measurements the lens was tilted, whereas in Zemax the field angle represents the angle of the incident beam. So the results of $+0.1°$ tilt during the experimental measurement corresponds with the results for -0.1° from Zemax. Table 5.2 summarizes the measured spot sizes at $\pm 0.1°$ tilting around the x and y axes at 780 nm and 980 nm. The simulation indicates that within $\pm 0.1°$ field angle, the beam remains non-aberrated, and the centroid is only displaced about 4.45 μm and causes a small reduction in the on-axis Strehl ratio. The measured results show larger spots than the Airy disk, and slightly elongated shape at some angles. However, in all measurements the best focused beam spot is free of major aberrations. Therefore, these observations indicate the system has some misalignment, particularly a tilted lens, which could be due to the many degrees of freedom that existed in the setup. Furthermore, the details of the images could not be fully resolved, because of the cameras' resolution. As a conclusion, the width and shape of the observed focused beam spots at different wavelengths, confirmed the lens performance within the field of view, as expected from the simulation.

Wavelength	780 nm			980 nm		
$1/e^2$ diameter (μm)	x cross-section	y cross-section	Average	x cross-section	y cross-section	Average
-0.1° tilting around x-axis	59.52±2.05	41.42±1.00	50.47±1.52	31.56±0.19	32.13±0.17	31.84±0.18
+0.1° tilting around x-axis	56.56±3.77	61.29±3.59	58.93±3.68	31.05± 0.31	33.98± 0.33	32.51±0.32
-0.1° tilting around y-axis	35.80±2.55	51.04±4.68	43.42±3.62	50.54±0.32	35.08±0.81	42.81±0.56
+0.1° tilting around y-axis	46.91±0.39	38.77±0.67	42.84±0.53	28.99±0.19	37.40±0.21	33.19 ±0.20

Table 5.2: Star test results of the tilted lens at 780nm and 980nm. the lens is tilted ±0.1 around x and y axes.
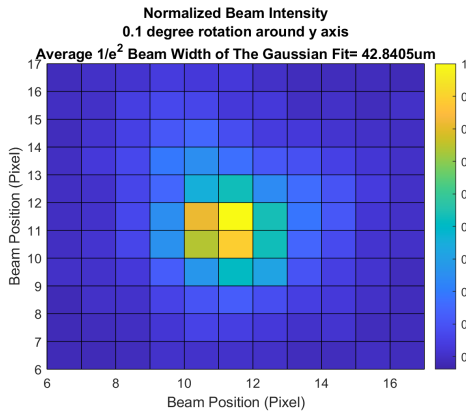
(a)
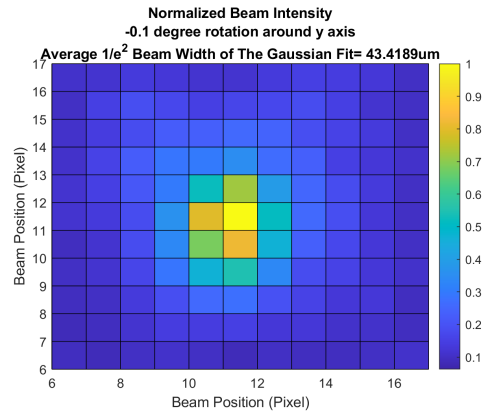
(b)
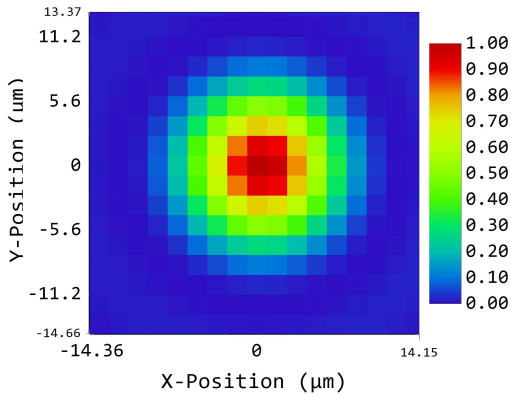
Polychromatic Huygens PSF

2021-04-20
0.7800 to 0.7800 μm at -0.1000, 0.0000 (deg).
Image size is 55.40 μm square.
Strehl ratio: 0.987
Center coordinates : -4.45327681E+00,   0.00000000E+00 Millimeters

(c)

Polychromatic Huygens PSF
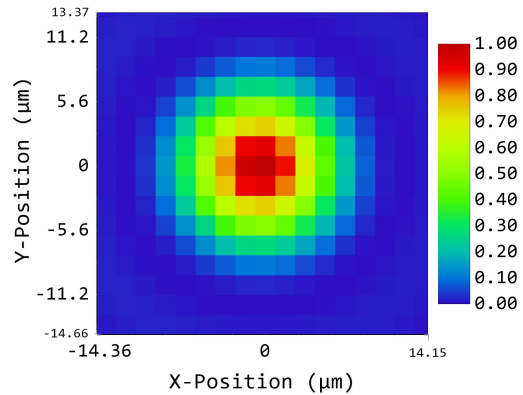
2021-04-20
0.7800 to 0.7800 μm at 0.1000, 0.0000 (deg).
Image size is 55.40 μm square.
Strehl ratio: 0.987
Center coordinates :   4.45327681E+00,   0.00000000E+00 Millimeters

(d)

Figure 5.6: $\pm 0.1°$ Rotation of the lens around y axis at 780 nm; Top: Measured results, Bottom: Huygens point spread function (PSF) plots from Zemax. $+0.1°$ tilting from in the measured data corresponds to $-0.1°$ in the simulated data, since in the star test the lens was tilted, whereas in Zemax the field angle (the incident beam angle) was changed.

5.1.2 Telescope Star Test

Experimental Setup

After assembling the telescope, we aligned the optics (Chapter 4) and found the focal position using our wavefront sensor which is discussed in the next section. Then we repeated the star test for a 780 nm beam.

We used the same method as the lens star test, to take the measurements on the telescope. The source was remained the same, except this time we only used the filters needed for 780 nm and we placed the telescope roughly 55 m far from the source as it was before. In addition, the hexapod was no longer needed, since the telescope was fixed on a cart, allowing it to be portable and stable. We used a focuser to mount the camera and or the fibre at the eyepiece of the telescope. First, we back propagated the green laser from the focal point of the telescope to determine the approximate position of the source. we tried to place our artificial star (the PM fibre) in the middle of the collimated beam coming from the telescope. Then, we replaced the green laser with the camera and used the visible light at the source to detect the spot on the camera. After completing the alignment, we used the supercontinuum laser with a set of filters to implement a point source at 780 nm.

Experiment and Results

By moving the camera back and forth we found the best focused image and averaged over 44 images. As with the lens star test, we could observe fluctuations in the intensity and location of the focused spot (The large error bars in the cross section plots are results of this variation). As mentioned before, natural vibrations of the building or each element, turbulent air between the setups and the fluctuations of the pulsed laser could be the reasons of not observing a fixed spot and intensity on the camera. The lens was mounted in an 8-inch lens cell fixed on the front lid of the telescope. So we were able to compare the results with the measurements on the lens with an 8-inch mask. The Airy diameter was measured as $22.583 \pm 0.13 \mu m$ (Fig. 5.8), which is a better result when compared to our lens test. Previously, the measured value had a 7.78% deviation from the theoretically derived value. However the new test, has reduced the error to 5.52% (1.3 μm smaller than the theoretical value).

Moreover, tests to observe the effects of tilting were also conducted. However, the entire telescope was not tilted. As mentioned above, the telescope was not mounted on a proper telescope tripod, thus the source had to be moved. Due to the limitation of the source's setup, we could only move it 126 mm in one direction which corresponds to $0.13°$
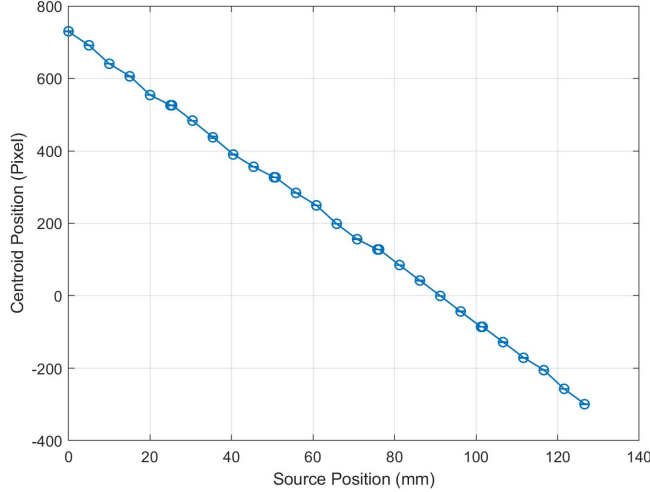
Figure 5.7: Centroid displacement of the focused beam as a function of point source position.

rotation around y axis. At 96 mm (0.1°), the measured Airy disk is 0.2 μm smaller than the theoretical value, while in the lens test the difference was about 20 μm. Therefore, our new alignment using the folding mirrors could reduce the error by 2 orders of magnitude. At 126 mm (0.13°) the error is 2 μm which indicates that beyond 0.1° the image is susceptible to aberrations. Fig. 5.9 shows 0.13° tilting results compared to Zemax PSF and confirms that the measured beam behaved as expected. Furthermore, we observed the centroid displacement over 0.13°. As a result the centroid was moved for 5.662±0.003 mm which is only about 0.2 μm difference from the reported value in the simulation (Fig. 5.7). Table 5.3 summarizes the best focused beam spot data, measured in the star test of the lens and the telescope which clearly indicates the improvement obtained in the telescope results, due to a better alignment.

	Lens results	Telescope results	Zemax
Focused Image	24.18±0.28μm	22.58±0.13μm	23.90μm
0.1° Tilting	42.84±3.68μm	24.09±0.16μm	23.90μm

Table 5.3: Image width resulted from the lens and telescope star tests, compared to the theoretical Airy disk ($1/e^2$ width is considered).
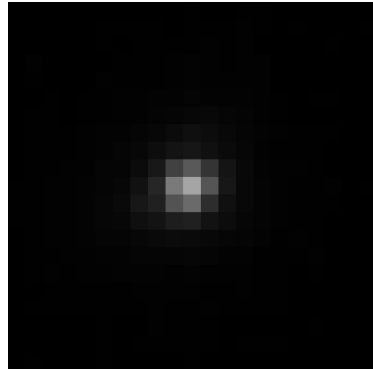
(a)
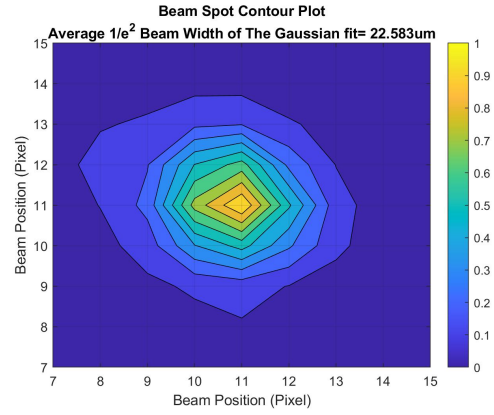
(b)
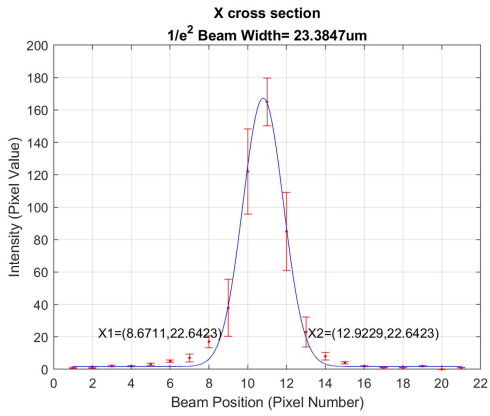
(c)
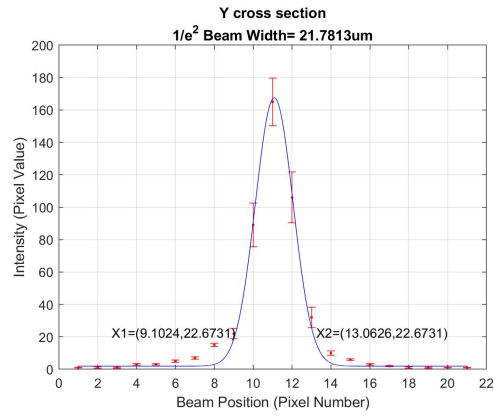
(d)

Figure 5.8: Star test of the telescope for the best focused image at 780 nm. The averaged Airy diameter is $22.58\pm0.13\mu$m which is only 1.3 μm less than the theoretically derived number.
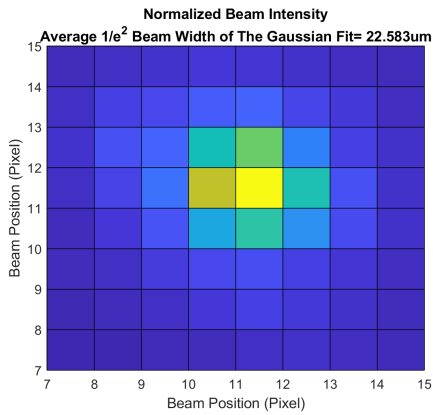
(a)
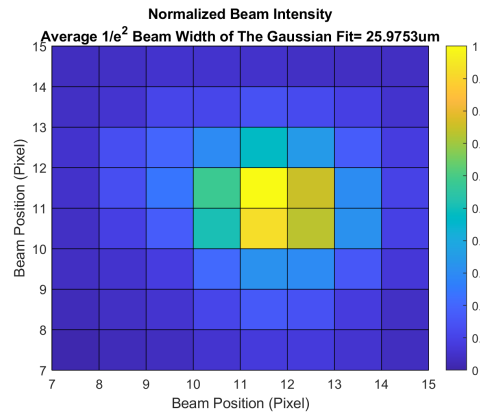
(b)
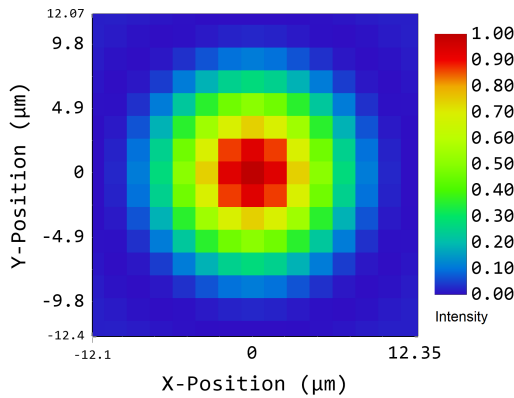
(c)
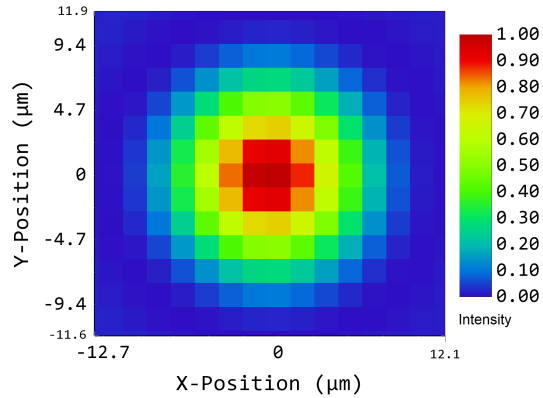
(d)

Figure 5.9: 0.13° tilting of the incident beam on the telescope at 780 nm; The source is moved 126 mm to create the 0.13° angle of the incident beam. The spot diameter is less than 0.2 μm off from the theoretical Airy diameter and the shape of the focused beam is well maintained and agrees with the simulated PSF (point spread function). Top: Measured results, Bottom: Huygens PSF plots from Zemax.

No.	Parts	Features	Model #	Company
1	9.5" Telescope Ring	ID: 9.5" OD: 10.5" One 1/4" threaded hole for mounting	N/A	KW Telescope
2	High Precision Hexapod	Six degrees of freedom: x, y, z, pitch, roll, and yaw Translation accuracy: 0.2, 0.2, 0.1 μm Tilting accuracy: 0.1, 0.1, 0.2 mdeg Centered load capacity: 500 N	HXP50-MECA	Newport
3	Motion Controller	-	HXP200-ELEC-D	Newport
4	Supercontinuum Laser	White light pulsed laser	S/N: KOH3403	NKT Photonics
5	3 Translation Stages	25 mm of travel Precision: >100 μm deviation	462-XYZ-M	Newport
6	Basler Camera	Sensor: CMV4000 CMOS NIR-enhanced Sensor Size: 11.3mm×11.3mm Resolution: 2048px ×2048px (4MP) Pixel Size: 5.5μm × 5.5μm Color: Mono Frame Rate: 90 fps	acA2040-90umNIR	Basler
7	InGaAs Camera	Resolution: 640px×512px Pixel Size: 15μm×15μm	WiDy SenS 640 M-StE	NIT
8	Band-pass Filters	1) Center wavelength: 780nm 2) Center wavelength: 908nm 3) Center wavelength: 1550nm	N/A	Thorlabs
9	Short-pass Filters	1) Cut-on wavelength: 800nm 2) Cut-on wavelength: 1000nm	N/A	Thorlabs
10	Long-pass Lilters	1) Cut-on wavelength: 700nm 2) Cut-on wavelength: 950nm 3) Cut-on wavelength: 1500nm	N/A	Thorlabs

Table 5.4: List of the components used in the Star test

5.2 Wavefront Measurement
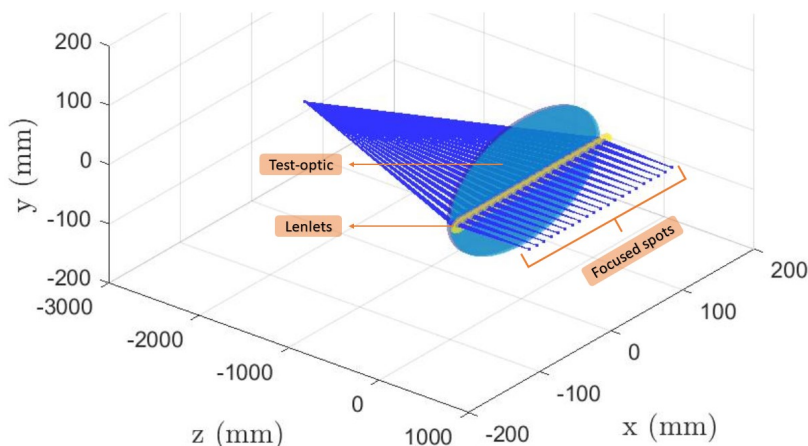
Figure 5.10: A simulation of one dimensional linear Shack-Hartmann method for large optics. Image illustrated by Youn Seok Lee.

In free-space optical communications, including quantum communication, the transmitted signal is prone to wavefront distortions by the atmospheric turbulence and optics imperfections or misalignments. Thus, it is crucial to minimize the wavefront error induced by the optical components to achieve a higher link budget in the presence of turbulence. Free-space quantum transmitters typically have 10 cm to 25 cm apertures that both transmit the quantum signal and receive the satellite tracking beacon. To attain a stable quantum channel, the transmitter telescope should be able to point at the satellite receiver aperture. This is achieved by tracking the satellite and correcting any small deviations via a series of optical elements [61]. However, since any optical element can affect the wavefront, each should be characterized individually and then, the the beam transmitted by the telescope must be measured to indicate the performance of the entire system.

Shack-Hartmann (Fig. 5.10) is the most popular wavefront sensor nowadays. It consists of an array of lenses (lenslets) with the same focal length which focus the uniformly distributed beam on a sensor [60]. Therefore, the centroid variations of the focused spots determines whether the incident beam is well collimated or not. Nonetheless, the major limitation of this method is the small size of the lenslets when it comes to large optics, particularly telescopes and large transmitters. Scanning laterally and stitching the measured wavefronts followed by post-processing and extra calibrations is one solution to this

issue [65][38]. Reducing the pupil size of the optic by adding a series of lenses and mirrors, [52][27] or using the sensor at the eyepiece of a telescope and considering a star as a point source to take multiple long measurements, are other approaches that can be used for wavefront characterization of large optics. However they require customized optics to minimize the aberration impact, which makes the project quite costly.

We developed a mobile wavefront measurement system for large optics and optical terminals which can be used as a collimation test of telescopes with large apertures [88] particularly the transmitters used for free-space quantum communication. Furthermore, this technique can be used for topographic measurement of curved [81][2] and flat large mirrors [94][64] as well as wafers [29]. We used a scanning pentaprism technique, which allows accurate slope measurements of the incident beam's wavefront. By scanning a horizontal diameter of the test optic and analysing the slope of the detected centroids, one can obtain the divergence angle of the transmitted beam. To achieve the wavefront slope, S, we consider f as the focal length of each lenslets, then in case of a diverging/converging beam, the incident angle of light θ is converted to the centroid displacement by $\Delta = f \tan(\theta)$. Therefore, S which implies the ray variation relative to x axis, can be written as:

$$S = \frac{\partial W(x,y)}{\partial x} = \tan(\theta) = \frac{\Delta}{f} \tag{5.2}$$

Furthermore, the transmitted wavefront is reconstructed by a basic numerical integration of the measured slopes over the scanning range by conventional least-squares method [79][45][47],

$$S_i = \frac{W_{i+1} - W_i}{h}, \tag{5.3}$$

where h is the spacing between the pentaprism positions. Therefore, $\vec{S}$ can be achieved by multiplying A by the wavefront ($\vec{W}$), where A is an N by N+1 matrix with diagonal elements of -1/h and the next element is 1/h,

$$A = \frac{1}{h} \begin{pmatrix} -1 & 1 & 0 & \cdots & 0 \\ 0 & -1 & 1 & \cdots & 0 \\ \vdots & \vdots & \vdots & \cdots & \vdots \\ 0 & \cdots & 0 & -1 & 1 \end{pmatrix}_{N,N+1}. \tag{5.4}$$

Now to reconstruct the transmitted wavefront from the slope measurement, both sides of the equation must be multiplied by the transpose of the matrix A. Since $A^T A$ is singular, A can be replaced by an extended matrix A_e, which has one additional row of ones,

$$A_e = \frac{1}{h} \begin{pmatrix} -1 & 1 & 0 & \cdots & 0 \\ 0 & -1 & 1 & \cdots & 0 \\ \vdots & \vdots & \vdots & \cdots & \vdots \\ 0 & \cdots & 0 & -1 & 1 \\ 1 & \cdots & 1 & 1 & 1 \end{pmatrix}_{N+1,N+1} . \tag{5.5}$$

Hence, by having $\vec{W} = (A_e^T A_e)^{-1} A^T \vec{S}$ the wavefront is calculated as below:

$$
\begin{pmatrix} W_1 \\ W_2 \\ \vdots \\ W_N \\ W_{N+1} \end{pmatrix} = \frac{1}{h^2} \left(\begin{pmatrix} -1 & 0 & 0 & \cdots & 1 \\ 1 & -1 & 0 & \cdots & 1 \\ 0 & 1 & -1 & \cdots & 1 \\ \vdots & \vdots & \vdots & \cdots & \vdots \\ 0 & \cdots & 0 & 1 & 1 \end{pmatrix} \begin{pmatrix} -1 & 1 & 0 & \cdots & 0 \\ 0 & -1 & 1 & \cdots & 0 \\ 0 & 0 & -1 & \cdots & 0 \\ \vdots & \vdots & \vdots & \cdots & \vdots \\ 1 & \cdots & 1 & 1 & 1 \end{pmatrix} \right)^{-1}
$$
$$
\times \frac{1}{h} \begin{pmatrix} -1 & 0 & \cdots & 0 \\ 1 & -1 & \cdots & 0 \\ 0 & 1 & \cdots & 0 \\ \vdots & \vdots & \cdots & \vdots \\ 0 & \cdots & 0 & 1 \end{pmatrix} \times \frac{1}{f} \begin{pmatrix} \Delta_1 \\ \Delta_2 \\ \vdots \\ \Delta_N \end{pmatrix} . \tag{5.6}
$$

We used this approach to investigate the properties of the transmitted beam of the lens and then of the assembled telescope. Wavefront measurements were done at different source positions to characterize the system. Moreover, the measurements helped with confirming the focal position of the lens with the simulation and aligning the optical elements in the assembly process.

5.2.1 Experimental Setup

Our wavefront sensor is based on a scanning pentaprism with a 4mm iris mounted on a motorized linear stage with straightness of 0.085 mm and travel range of 40 cm which is controlled by a stepper motor. The incident beam is generated by an external cavity diode laser (DLpro) with continuous-wave mode at 785 nm, coupled to a single mode fibre which is fixed on a 3-axis translation stage to facilitate alignment. The beam coming from the lens, must be detected by the pentaprism and be reflected to the retroreflector. Then, the
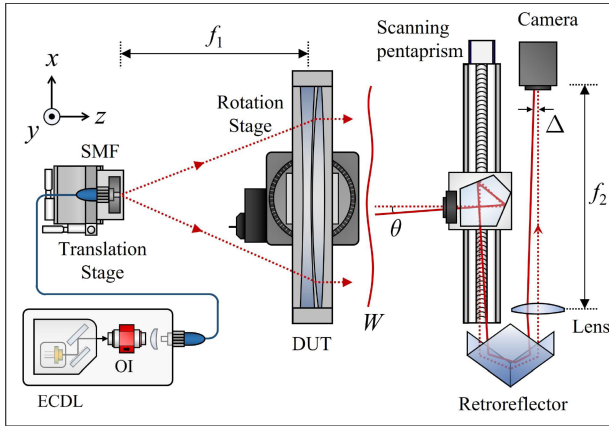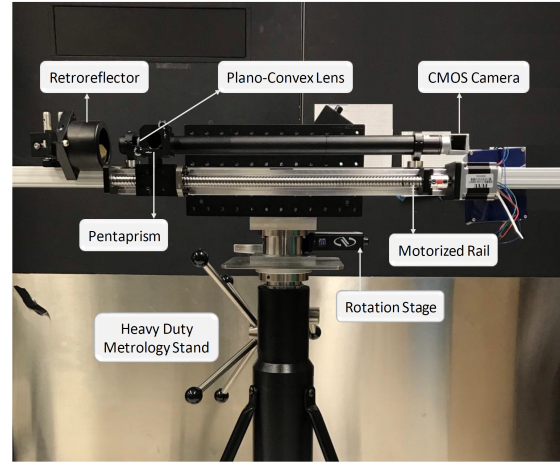
Figure 5.11: (a) Schematic diagram of the experimental setup for wavefront measurement. ECDL, external cavity diode laser; SMF, single-mode fibre; OI, optical isolator. A pentaprism mounted on a motorized linear stage, performs one dimensional scan across the lens. It deflects the incident light by 90° to get focused on the camera via the convex lens (Lens 2). Image created by Youn Seok Lee [47]. (b) A photo of the scanning pentaprism system.

retroreflector folds the beam and sends it to a plano-convex lens (Lens2) with f2 =500 mm, which focuses the spot on the sensor of a CMOS camera. Considering the long focal length of the focusing lens (Lens2), the retroreflector helps keep the total length of the setup shorter. The lens is fixed on a rotation stage with an accuracy of less than 0.010° which allows us to rotate the lens around the y axis. The entire system is mounted on a height-adjustable heavy duty metrology stand to maintain the stability during the tests (Fig. 5.11). The components used in this experiment are listed in Table 5.5.

Prior to conducting the measurements, we used back propagation of a visible green laser to find the approximate focal position. Although this method helps with detecting the focal point in x-y plane, it can not be a precise test for z-axis (light propagates along z axis). Then, the fibre is switched to 785 nm for the measurements and illuminates the lens from the approximate focal point. The pentaprism moves along the linear stage to scan across a diameter of the lens and collect the incoming beam. The advantage of using the pentaprism is that the centroid in the xz-plane is essentially unaffected by the pentaprism rotation angle to the first-order. We investigated the impacts of tilting the pentaprism in higher orders. The simulation results, revealed that rotation around x-axis affects the slope measurement noticeably. The characterization of the setup has been discussed in

details in [47]. The camera sensor is 11.3 mm × 7.1 mm and with having $f_2 = 500$ mm, the peak-to-valley dynamic range of the system is found to be larger than 50λ with step size of 2 mm. By taking the paraxial approximation into account, a spot of 240 μm is detected on the camera which covers about 40 pixels (pixel size = 5.86 μm) and if the centroid precision is considered 1/10 of the pixel size [29], then the accuracy of the slope measurement is considered to be about 1 μrad.

The camera controls the intensity of the incoming light via a developed exposure time control which avoids saturation and keeps the signal to noise ratio at about 10. For this purpose, a thread parallel to the main thread has been defined to constantly check the intensity and keep it at the desired pixel value that is initially determined by the user. A PID loop has been implemented in this thread, so that by changing the gain values, the intensity can be stabilized at the setpoint within a short time. PID controller uses 3 gains: Proportional gain, Integration gain and Derivative gain. It takes the difference between the setpoint and the current value as the error e(t) and tries to make it zero by having proper gain values. Proportional gain increases the error ($K_p \times e(t)$) to make the system more responsive to it, so having a high proportional gain can make the system unstable. Then the integration gain, integrates the error value ($K_i \times \int_0^t e(t)dt$) until it gets zero and stabilizes at the desired value. Derivative gain predicts the error and it is dependent on the rate that the error is changing ($K_d \times \frac{de(t)}{dt}$). In order to control the exposure time of the camera and avoid saturation, we considered 200 as the setpoint and set the integration gain at 50. Our PID controller, only needs the integration part to see the error and make it zero, so its value was determined by perturbing the system and observing how fast it could recover and stabilize.

Before running the test, the camera and the motor are needed to be connected and initialized individually. Once the camera is connected and it starts a live view window. The beam must be detected on the screen, if not, the height of the metrology stand has to be changed or the rail must be rotated around y axis to find the beam image. It is recommended to keep the PID controller off during the alignment and avoid high exposure times in order not to burn any pixels. Once the spot is detected, the PID controller must be performed immediately to optimize the exposure time.

To have a one dimensional measurement on the wavefront, minimum and maximum positions of the pentaprism must be defined. We considered grabbing 20 photos at each position and repeating the whole test 5 times. So that we could report the results in form of the mean value and consider the standard deviation as the measurement error. For each photo the centroid variation is estimated by subpixel centroid algorithms [1] and the results are saved in an excel file for post processing purposes. The entire measurement takes about 30 minutes for collecting 100 centroids at one line across an 8-inch lens. Tests
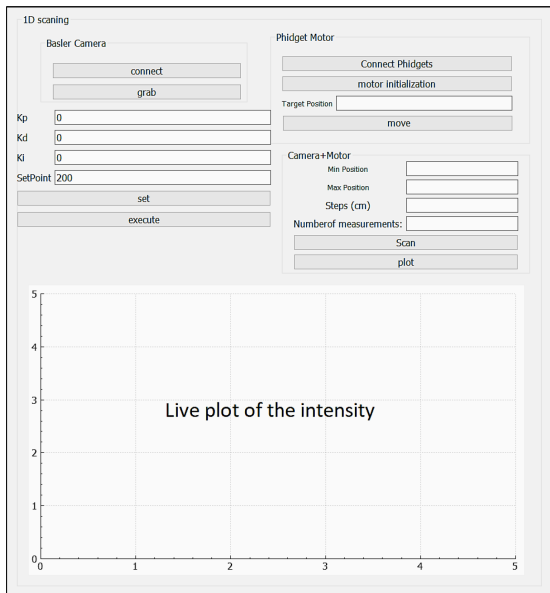
Figure 5.12: Graphical user interface (GUI) of wavefront measurement.
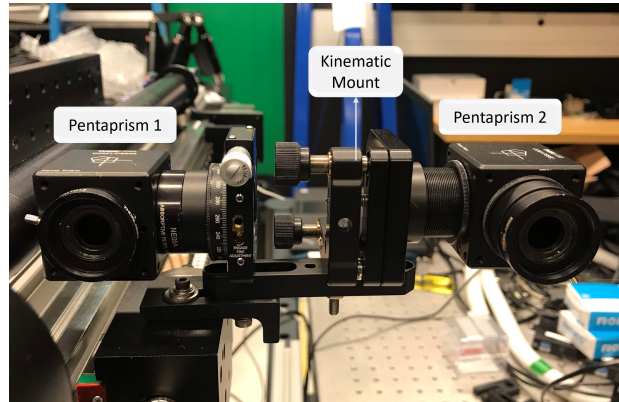
Figure 5.13: The second pentaprism attached to the kinematic mount is added to correct any potential tiling of the first pentaprism.

done on different diameters of the lens can result in different wavefront errors since the lens does not have the same quality across its surface. This difference was noticed in the tests on the telescope and the lens separately. A two-dimensional scanning system, that is the future work, could overcome this issue and provide a precise map of the wavefront. In addition, the focal length of the lens was measured using this method, to be confirmed with the design. Fig. 5.14 and Fig. 5.12 show the flowchart and graphical user interface of the wavefront measurement process done by our one dimensional wavefront characterization setup.

Figure 5.14: Slope Measurement Process

119
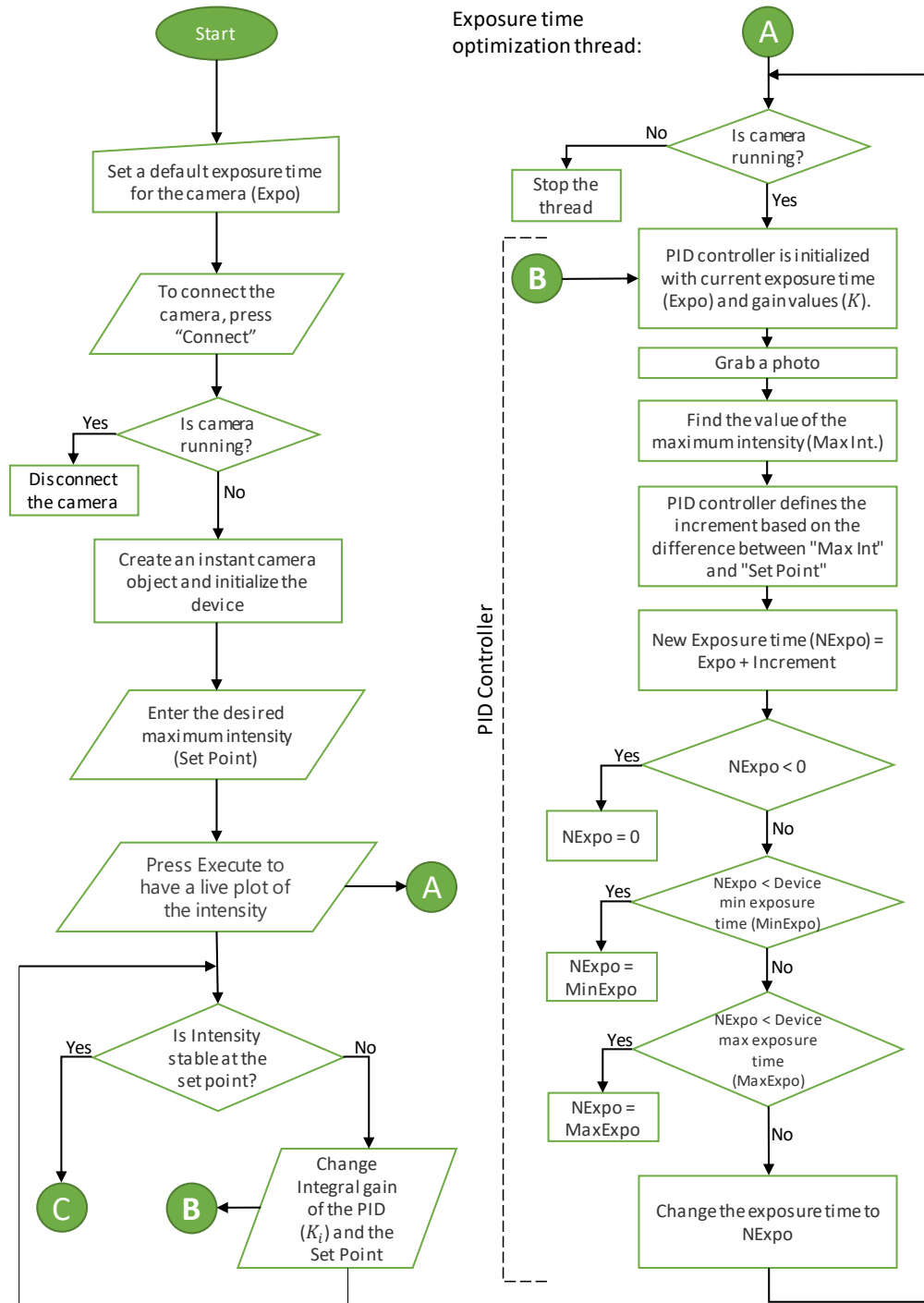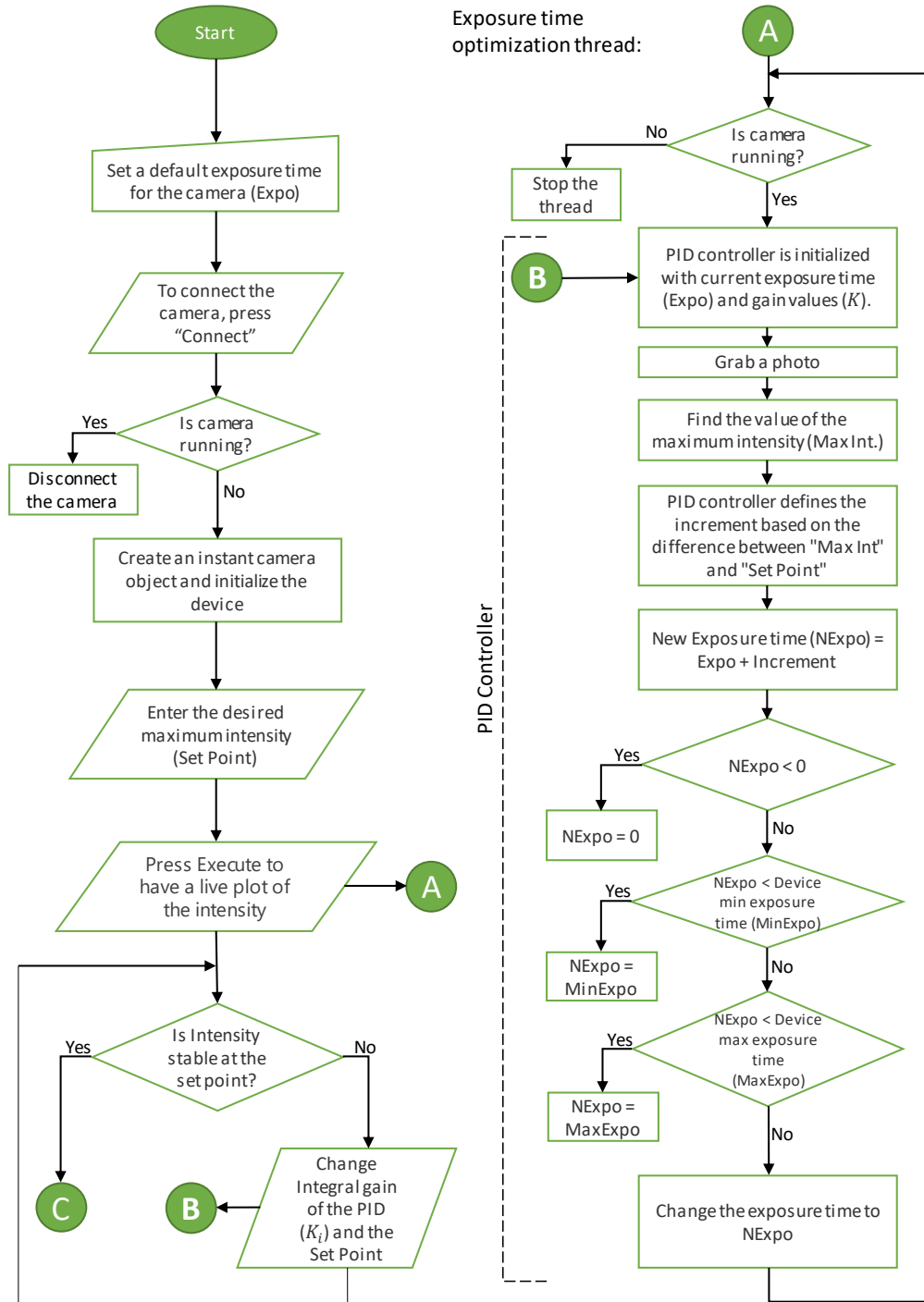
5.2.2 Lens Wavefront Measurement

To measure the wavefront error induced by the surface irregularity of the lens, it is required to make sure the transmitted beam is perfectly collimated. Therefore, after adjusting the focal point on the x-z plane by back-propagation of the green laser, we moved the fibre in z the direction to obtain the minimum slope which represents the smallest divergence angle. Fig. 5.15(a) shows the slope measurement at 8 different positions of the fibre. $z = 7$ mm has the least slope which indicates that the fibre is at the focal point. One approach to derive the exact position is plotting the slope of each measurement versus fibre positions and interpolate the minimum of the curve. We obtained $z = 6.95$ mm as the optimal position of the fibre. 5.15(b) is the reconstructed wavefront of the beam for different z positions. The wavefront error is critically sensitive to the divergence of the beam. As illustrated, the PV wavefront error increases to 0.5λ by only 1 mm shifting of the source.

5.15(a) shows some wiggles on the right end of the plots, which could be either the error induced by the measurement device or the irregularities of the lens surface. One possible systematic error could be the straightness of the rail. So we repeated the test by having the pentaprism moving close to the other end of the rail. However, the pattern was still observed. Therefore, we decided to characterize the setup individually first. We used a second pentaprism attached to a kinematic mount to correct any potential tiling of the first pentaprism. Then the fibre was located on the metrology stand to send the beam parallel to the rail (Fig. 5.13). This was to show that in case the wiggles were caused by the unsteadiness of the stand we were expecting to have them eliminated from the plot and if it was induced by the motor or the rail, the same pattern had to be observed. In addition, if the pentaprism was tilted it had to be corrected by the second pentaprism. Nevertheless, having too many degrees of freedom in the alignment, did not help with detecting the problem. Thus, a future plan is to glue two pentaprisms on a flat plate and then mount it on the rail to eliminate the tilting factor and then repeat the test to discover the flaws of the other mechanical parts.

The second batch of measurements were done on the impact of a tilted lens. We rotated the lens around y axis to align its optical axis with z direction and achieve the minimum divergence angle. Fig. 5.15(c) displays the slope measurement on $\pm1.5°$ rotation of the lens around y axis. The reconstructed wavefront plot (Fig. 5.15(d)) implies that the wavefront error is less sensitive to the tilting of the lens, since the PV wavefront error is remained less than 0.25λ within $\pm0.5°$.

To characterize the uniformity of the beam over the scanning range of the pentaprism and also to optimize the position of Lens2, we repeated the slope measurement for translation of the fibre in the x-direction (Fig. 5.16). Any movements of the fibre in the x

(a)

(b)

(c)

(d)
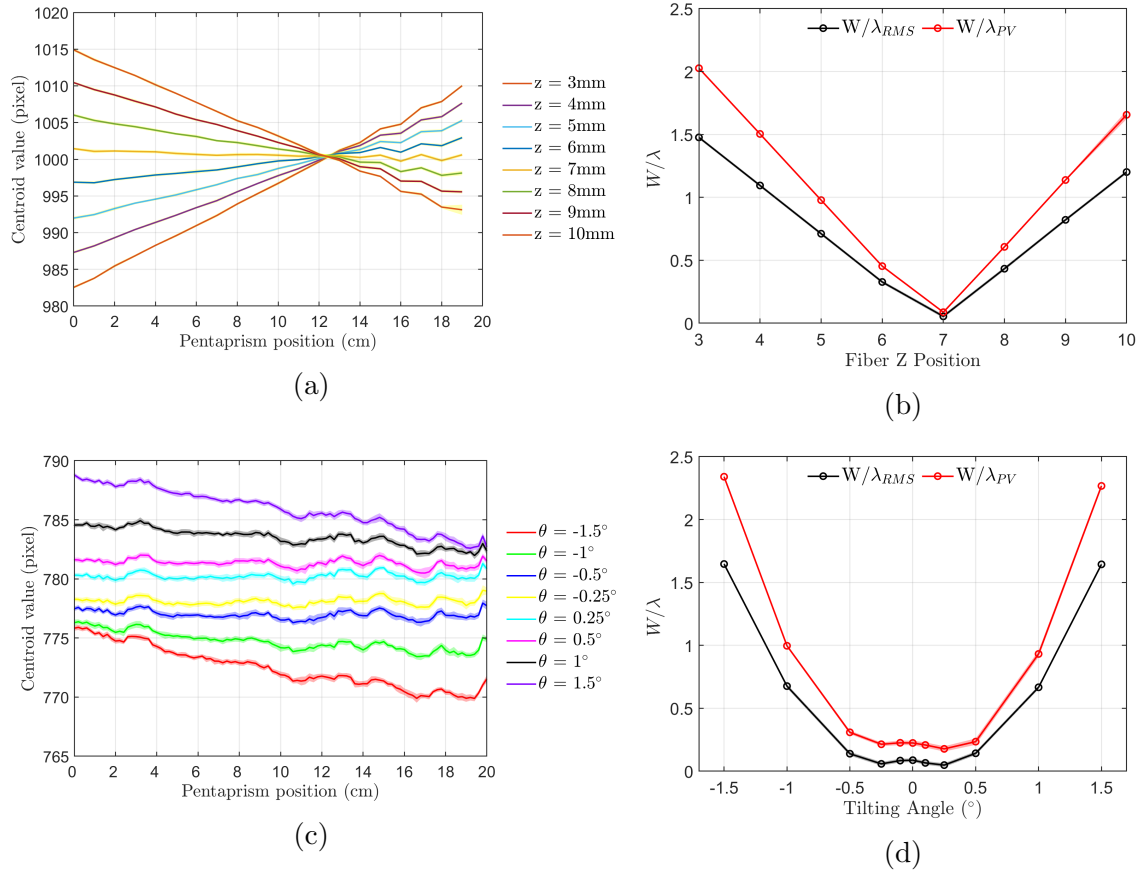
Figure 5.15: (a) Slope measurement and (b) wavefront error of the transmitted beam for different positions of the fibre on the optical axis (out of focus). (c) Slope measurement and (d) wavefront error of the beam at different tilting angles of the lens. The PV wavefront error is determined to be less than 0.25λ at $\pm0.5°$ tilting angles. However, the wavefront is quite sensitive to the fibre position and only 1 mm translation increases the wavefront error by 0.5λ.
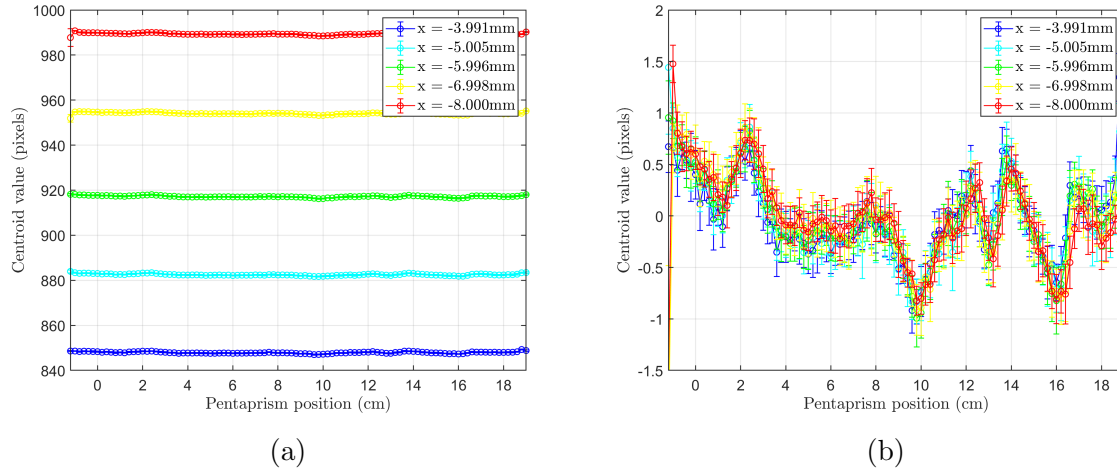
Figure 5.16: wavefront slope measurement as a function of the pentaprism position for translations in the x direction. (a) The spacing between each measurement is equal and proportional to the x-translation value. By applying a proper offset, all slope measurement graphs for different x values must overlap, which is confirmed in (b). It also shows the repeatability of our setup.

direction is directly related to the displacement of the centroid along the x-axis of the camera. Therefore, it was expected to observe the same slope measurement results for all x values, but shifted vertically with equal spacing. Fig. 5.16(a) confirms this approach and suggests that plotting the x-centroid versus fibre positions, must result in a line with unity slope. Hence, by having the focal length of Lens1 and considering the unity slope multiplied by the focal ratio, the focal length of Lens2 can be determined. The averaged mean slope value is calculated -1.000±0.003 with averaged standard deviation of 0.009. This accuracy implies that the centroids can be defined with precision of less than 1%. Moreover, comparing the results with the ray-tracing model of a tilted lens revealed 0.26λ and 0.48λ as the norm of residuals for $+1.5°$ and $-1.5°$ respectively [47]. The quantitative and qualitative agreement of the experimental data and the theory proves the validation of our wavefront measurement setup with the scanning pentaprism.

Finally, after determining the optimal position of the fibre along the z axis and setting the lens perpendicular to it, we ran the measurement 5 times and the averaged data indicated less than a pixel variation of the centroid and hence, less than 2.5 μrad divergence angle of the beam. In addition, the focal length of the lens was measured and the result agrees well with the lens design. The peak-to-valley wavefront error of the reconstructed wavefront, was obtained to be 0.223λ which matches our initial design and manufacturer report (0.25λ). Fig. 5.17(a) and (b) show the slope measurement and wavefront error of

123

the lens at 780 nm. The 0.007λ uncertainty of this wavefront characterization approach suggests the excellent repeatability and stability of the system and emphasises its high precision comparing to the 0.02λ to 0.1λ accuracy of other similar methods [52][27][38].

(a)

(b)

(c)

(d)
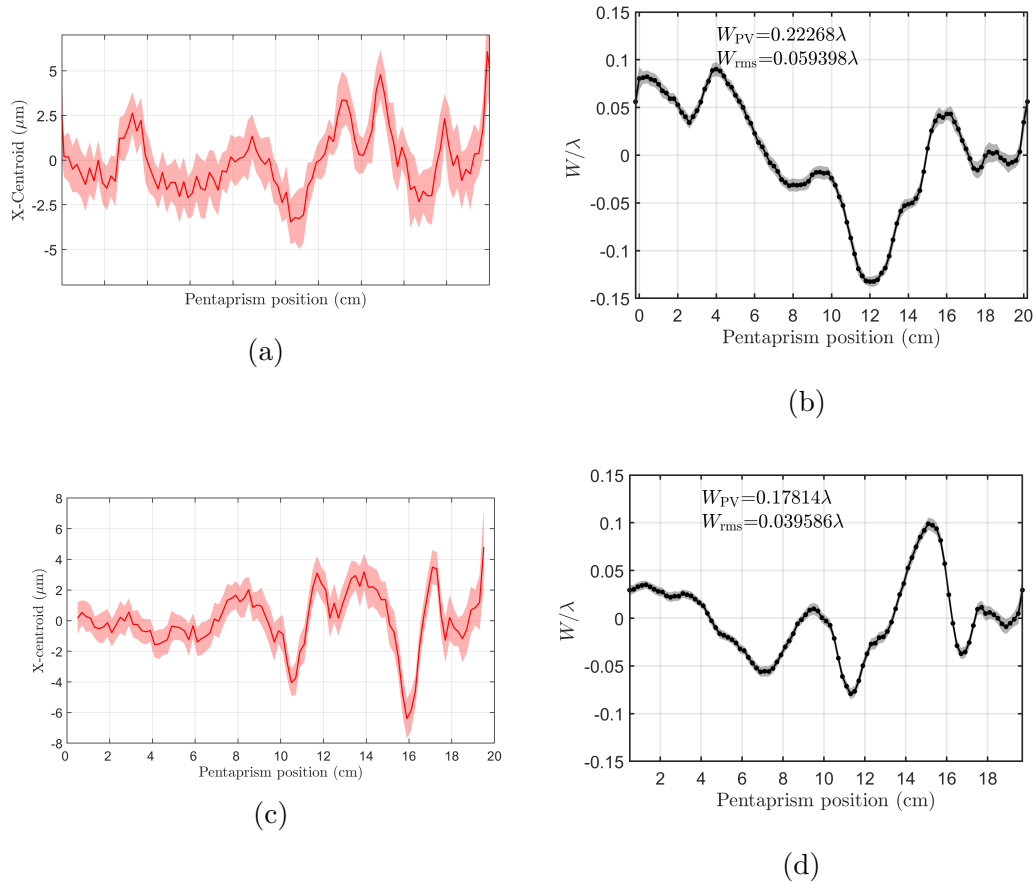
Figure 5.17: (a) and (b): Slope measurement and wavefront error of a beam transmitted through the lens by a fibre at the focal point. The same measurement was performed on the telescope and resulted in (c) and (d). Both measurements indicate less than $\lambda/4$ PV wavefront error. (Since each test was done on a different diameter of the lens, the obtained plots are slightly different.)

5.2.3 Telescope Wavefront Measurement

After Assembling the telescope, it was critical to repeat the collimation test to align the mirrors and find the focal point. As discussed in Chapter 4, after a rough alignment of

No	Parts	Features	Model #	Company
1	Pentaprism	Surface Flatness: $> \lambda/10$ at 633nm Reflective Beam Angle: 90°±20 arcmin Reflective Coating: Aluminum with Inconel and black paint overcoat Assembly Dimension: 38.1mm×38.1mm×38.1mm Clear Aperture: 12 mm	CCM1-PS932	Thorlabs
2	Motorized Linear Stage	Straightness: 0.085 mm Travel range: 40 cm	FSL40	FUYU
3	External Cavity Diode Laser	Wavelength: 785nm Power range: 10-300mW	DLpro	Toptica photonics
4	plano-convex lens	Focal length: 500 mm	N/A	N/A
5	CMOS Camera	Sensor: IMX249CMOS Sensor Size: 11.3mm×7.1mm Resolution: 1920px×1200px (2.3 MP) Pixel Size: $5.86\mu m \times 5.8\mu m$ Color: Mono Frame Rate: 41 fps	acA1920-40um	Basler
6	Rotation Stage	Angular Range: 360° Min Increment Motion: 1.0mdeg Max Torque: 2N.m Centered Load Capacity: 900N Accuracy: ±7.0mdeg	RVS80CC	Newport
7	Heavy Duty Metrology Stand	Min Height: 940mm Max Height: 1,435mm Max Load: 68.2kg	233 Series	BRUNSON

Table 5.5: List of the components used in the wavefront measurement

the folding mirrors by propagating the green light, we used 785 nm laser at the eyepiece of the telescope. Since the approximate position of focal point was already determined, by moving the focuser in the z direction and measuring the centroid values as a function of the pentaprism position, we achieved a collimated output beam with almost the same divergence angle as measured for the lens (Fig. 5.17 (c)). Then we reconstructed the wavefront, to detect the wavefront error. The peak-to-valley wavefront error was attained 0.178λ (Fig. 5.17 (d)). This number is less than the lens measurements results. The main reason of this difference, is scanning a different diameter of the lens comparing to the tests that were done before assembling the telescope.

5.3 Polarization Measurement

Because we are working towards polarization-based quantum communication, we require highly pure polarization photonic states to be exchanged between the transmitter and the receiver, so preserving the polarization is crucial in order to avoid any systemic errors. However, manufacturing imperfections, birefringent property of the optics materials, stress, bending, temperature variations or polarization rotations can change the polarization states of a transmitted beam. Moreover, since the lens is fixed in a 2-piece lens cell, exerting high torque on the screws, could potentially cause stress induced birefringent patterns on the lens which can be detected in the polarization test. If the lens was under stress, then the areas near the edges could induce a polarization rotation that will result in a low state fidelity. Therefore, it is important to perform more polarization tests after assembling the telescope, in addition to the measurements on the lens separately, to not only study the polarization preservation of the mirrors and lens together, but also check the stress induced degradation of the state fidelity.

Polarization characterization is performed by preparing highly pure polarization states and sending them through the test-optic and measuring the output. Variations of the of beam size and incident angle on the optics or their specific configurations can impact the polarization preservation. Thereby, several sets of measurements are required to characterize the entire assembly with high precision, which is quite challenging. The QPL group developed an in-house polarization measurement set-up to characterize the optics at different sizes and configurations with high repeatability and accuracy. We used a 6-joint collaborative robot arm that holds a polarimeter and moves it on any trajectories needed to scan the test-optic. Then the data is collected and analysed by the computer. The entire process is automated to minimize the measurement error.

The polarization measurement process is based on preparing initial pure states of $|H\rangle$ (horizontal), $|V\rangle$ (vertical), $|D\rangle$ (diagonal, 45°), or $|A\rangle$ (antidiagonal, −45°) and measuring the output power by a polarimeter after projecting them onto $|H\rangle$, $|V\rangle$, $|A\rangle$, $|D\rangle$, $|R\rangle$ (right circular) and $|L\rangle$ (left circular) states, using waveplates. Stokes parameters can be used to define the polarization state of a beam. A Stokes vector has four elements, representing the total power (I), $|H\rangle$ an d $|V\rangle$ states (Q), $|A\rangle$ and $|D\rangle$ states (U), $|R\rangle$ and $|L\rangle$ states (V):

$$\vec{S} = \begin{pmatrix} S_0 \\ S_1 \\ S_2 \\ S_3 \end{pmatrix} = \begin{pmatrix} I \\ Q \\ U \\ V \end{pmatrix}. \tag{5.7}$$

Each of the Stokes parameters can represent the normalized difference between the measured powers at each of the 2 orthogonal polarization states. $S_i \in \{Q/I, U/I, V/I\}$, where S_i is obtained from,

$$S_i = \frac{P_{e,i} - P_{o,i}}{P_{total}}. \tag{5.8}$$

$P_{e(o),i}$ is the power measured at i-th waveplate for the extraordinary (ordinary) light. At the polarimeter, the Mueller matrix is used to model the polarizer, QWP and HWP [45][46]:

$$M(\theta_P, \theta_H, \theta_Q; \phi_H, \phi_Q) = M_P(\theta_P) M_H(\theta_H; \phi_H) M_Q(\theta_Q; \phi_Q), \tag{5.9}$$

where, θ and ϕ refer to the rotation angle and phase retardance of the waveplates respectively. M_P, M_Q and M_H are the linear polarizer, QWP and, HWP Mueller matrices.

$$M_{\text{H(Q)}}(\theta; \phi) = \begin{bmatrix} 1 & 0 & 0 & 0 \\ 0 & \cos(2\theta)^2 + \sin(2\theta)^2 \cos\phi & \cos(2\theta)\sin(2\theta)(1 - \cos\phi) & -\sin(2\theta)\sin\phi \\ 0 & \cos(2\theta)\sin(2\theta)(1 - \cos\phi) & \cos(2\theta)^2 \cos\phi + \sin(2\theta)^2 & \cos(2\theta)\sin\phi \\ 0 & \sin(2\theta)\sin\phi & -\cos(2\theta)\sin\phi & \cos\phi \end{bmatrix},$$

$$M_{\text{P}}(\theta) = \begin{bmatrix} 1 & e\cos(2\theta) & e\sin(2\theta) & 0 \\ e\cos(2\theta) & e\cos(2\theta)^2 & e\cos(2\theta)\sin(2\theta) & 0 \\ e\sin(2\theta) & e\cos(2\theta)\sin(2\theta) & e\sin(2\theta)^2 & 0 \\ 0 & 0 & 0 & 0 \end{bmatrix}$$

$$\tag{5.10}$$

Since the extinction ratio of the polarizers in both polarimeters are very high, the degree of polarization is considered as unity ($e = 1$). The phase-retardance (ϕ) of HWP and QWP are ideally set at π and $\pi/2$ respectively. Hence, to generate the 6 polarization states, angle of the polarizer is considered at either $0°$ or $90°$, and the angle of the waveplates change according to the measurement basis as listed below.

- H/V : $\theta_H = 0°$, $\theta_Q = 0°$.

- A/D : $\theta_H = 22.5°$, $\theta_Q = 45°$.

- R/L : $\theta_H = 0°$, $\theta_Q = 45°$.

127

The first row of the Mueller matrix represents the power and since we need 6 measurements for all states, we can take use of an *Instrument Matrix*, $A = [\vec{M}^{(H)}, \vec{M}^{(V)}, \vec{M}^{(D)}, \vec{M}^{(A)}, \vec{M}^{(R)}, \vec{M}^{(L)}]^T$. So the power measurement can be related to the incident Stokes parameters by $\vec{P}_{mea} = A.\vec{S}_{in} + P_d$, where P_d is responsible for random fluctuations of the power due to the background noise. Then the measured Stokes vectors can be achieved by multiplying the pseudo-inverse matrix of the instrument matrix, $W = (A^\top.A)^{-1}.A^\top$.

$$\vec{S}_{out} = W.\vec{P}_{mea} \tag{5.11}$$

The obtained Stokes vectors can be used to reconstruct the density matrix for the measured polarization state:

$$\hat{\rho} = \frac{1}{2}[\mathbb{I} + \frac{Q}{I}\hat{\sigma}_z + \frac{U}{I}\hat{\sigma}_x + \frac{V}{I}\hat{\sigma}_y] \tag{5.12}$$

Finally, the results are used to indicate,

- Purity:
  The state's degree of pureness : $Tr(\rho^2)$.

- Fidelity:
  The closeness of the measured state (ρ) to the input state (σ): $\left[Tr\sqrt{\sqrt{\rho}\sigma\sqrt{\rho}}\right]^2$.

- QBER:
  Quantum Bit Error Rate: $\text{QBER}_{H(V,A,D)} = \frac{P_{V(H,D,A)}}{P_{H(V,A,D)} + P_{V(H,D,A)}}$.

QBER depends on the protocol and the implementation method used in the experiment. For example, the QBER tolerance of BB84 has been increased from 11% to 18.9% by improving the error correction and privacy amplification of the protocol [30]. Furthermore, in a decoy state implementation of QKD ([58]), the QBER limit for successful QKD is mentioned as 7%. In a recent work by QPL group [10], an average of 3.5% QBER was obtained in a laboratory study, by modifying the protocol. The measured QBER in this experiment varied from 1.94% to 6.06%, and because the maximally allowed 7% error can be caused by different components of the link, the QBER induced by the transceiver must be minimized to allow for other inevitable errors.

5.3.1 Experimental Setup

We characterized the polarization preservation of the optical components of the telescope via a 6-joint robot arm carrying the polarimeter and automated by developing software kits
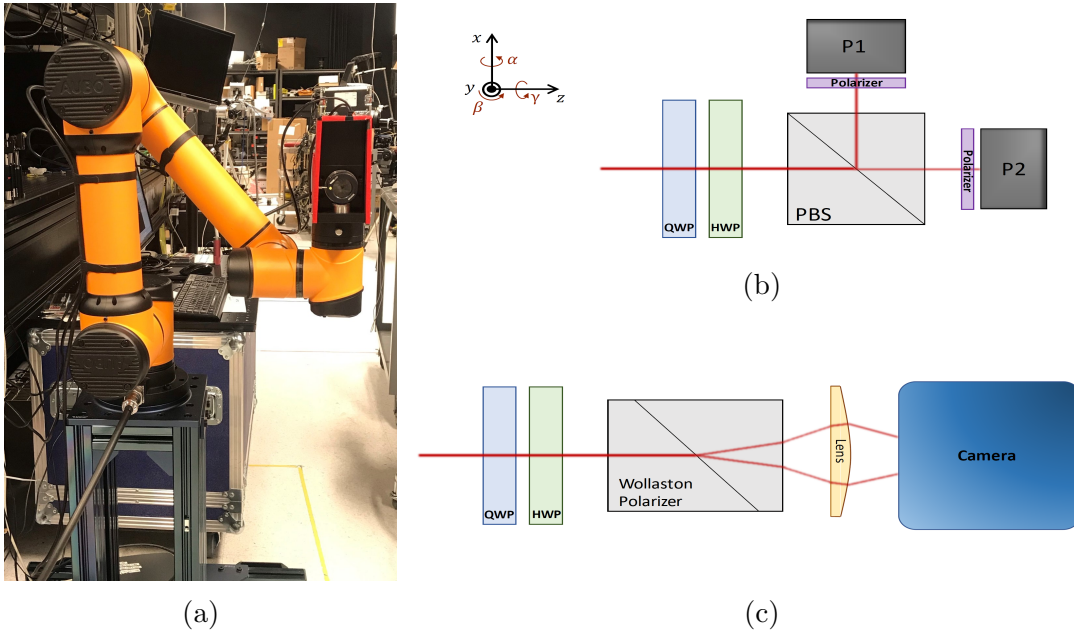
Figure 5.18: Polarization measurement setup; (a) Robotic manipulator with the camera-based polarimeter; (b) Schematic diagram of the old polarimeter with a polarizing beam splitter (PBS) and two power meters (P1 and P2); (c) The new camera-based polarimeter consists of a Wollaston polarizer and a camera.

in C++. For each input state, the robot scans a defined trajectory and performs the power measurement at each of the six polarization states. After the completion of this process, a polarization tomography[5] is applied on the measurement to reconstruct the states and determine the fidelity, purity and QBER. The set-up includes 3 main parts: light source, polarimeter and robot arm.

Light Source We used an external cavity diode laser (DLpro) to generate continuous-wave mode at 785 nm. Then the input polarization is prepared in an optical isolator and coupled to a polarization maintaining fibre which sends the light with a single spatial mode through a linear film polarizer. The fibre and the polarizer are mounted on a rotation stage to define the 4 input polarization states with an accuracy of $\pm 0.025°$.

Polarimeter Two generations of polarimeters were used in these measurements. The first generation includes a polarized beam splitter (PBS) and two power meters to directly

---

[5]Tomography is the reconstruction of the input states based on the remeasured states. Please see *"Photonic State Tomography",Altepeter, J.B., Jeffrey, E.R. and Kwiat, Paul* for detailed explanation of polarization-based photonic tomogragray. [3]

read the intensity of the transmitted beam (Fig. 5.18(b)). The extinction ratio of a PBS is typically about 1,000:1, so we improved the ratio by adding a linear film polarizer (up to 100,000:1) in front of each power meter. The beam goes through a quarter-waveplate (QWP) and a half-waveplate (HWP) that are mounted on motorized rotation stages and project the input states onto 6 tomographically complete[6] polarization states $(|H\rangle, |V\rangle, |A\rangle, |D\rangle, |R\rangle, |L\rangle)$ and then the orthogonal states of each basis get split by the PBS to be measured by the power meters.

The new polarimeter consists of the QWP, HWP, a Wollaston polarizer, a convex lens (f=30 mm) and a 16-bit CMOS camera (PCO) (Fig. 5.18(c)). The Wollaston polarizer spatially separates the extraordinary and ordinary light. Both beams are focused on the camera by a convex lens. The detected beams appear on the camera as two separate spots with varying brightness, depending on the rotation angle of the waveplates. So each frame captured by the camera contains the information on both states. Then, by performing a centroid calculation to determine the exact position of the spots and subtracting the background noise, the intensity can be achieved to calculate the power and reconstruct the output states. The intensity of the light on the imaging camera is controlled by an automated exposure-time controller to avoid pixel saturation. The camera is characterized initially to confirm the average pixel value is linearly related to the exposure time and to determine the dynamic range of the camera which is 21,500:1 (An order of magnitude smaller than the extinction ratio of the linear film polarizers). In addition, a pixel value of 200 is considered to be the noise level of the system which is due to the shot noise, the dark count and the read-out noise. With characterizing the camera and controlling the exposure time between 0.200 ms to 500 ms, extinction ratio of 100,000:1 can be achieved.

This new polarimeter has the benefit of reducing the measurement time almost by half, since it records both states at the same time. In addition, it provides more accuracy due the centroid calculations and SNR optimizations comparing to reading the received powers by the power meters. However, since the intensity received by the camera is limited to the maximum pixel value, the dynamic range is typically smaller than the power meter's which results in having larger error bars and larger QBER in the measurements.

Robot Arm A geared servo-motor with absolute encoder at each joint allows the robot arm (AUBO-i5, AUBO Robotics) to move at any arbitrary trajectory (Fig. 5.18(a)). The arm reaches 0.924 m and has a payload capacity of 5 kg. As claimed by the manufacturer, it has 0.02 mm position repeatability, 2 mm position accuracy, 0.004° averaged orientation

---

[6]Tomographically complete measurements is defined as having the positive-operator valued measurements (POVM) that form an operator basis on the Hilbert space of the quantum system, which provides the entire information about the state. [54]
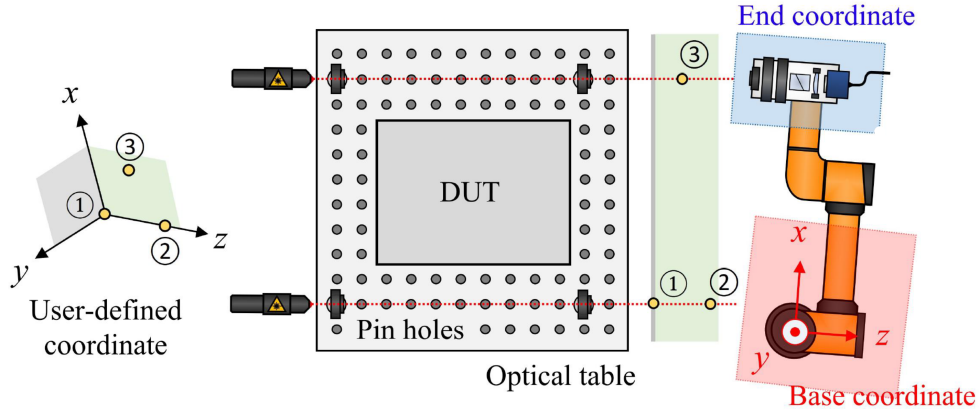
Figure 5.19: User coordinate calibration; We used three points: Point1 at the origin, Point2 on the z axis and Point3 on xz plane to define the user coordinate system. The procedure is explained in the main text. DUT: Device Under Test; The diagram is adapted from [46], illustrated by Youn Seok Lee.

repeatability and 0.05° accuracy. Before performing the measurement it is crucial to choose and calibrate the practical coordinate system required for the experiment. This is discussed in 5.3.2

After calibration of the polarimeter and the robot arm, the polarization measurements were performed on different test optics. The first generation polarimeter was used to characterize the polarization maintenance of a prototype telescope built by Honeywell and its primary mirror. Next, with modifying the polarimeter to the new camera-based one, the measurement was done on the custom-designed lens and the folding mirrors under different incident angles to characterize the optics used in the telescope individually. Finally, the polarization preservation of the assembled telescope was tested to confirm its performance for polarization-based QKD.

5.3.2   Calibration

To scan the surface of the large optics, it is crucial to have the robot arm move on the correct trajectory relative to the optical system under test. This robotic manipulator uses three different coordinates: Base coordinate (the absolute positions: x, y, z), End coordinate (the orientations: α, β, γ) and a user-defined coordinate, which requires 3 orthogonal axes to be defined. So a combination of 3 different points (2 vectors) are needed to obtain the

(a)   (b)
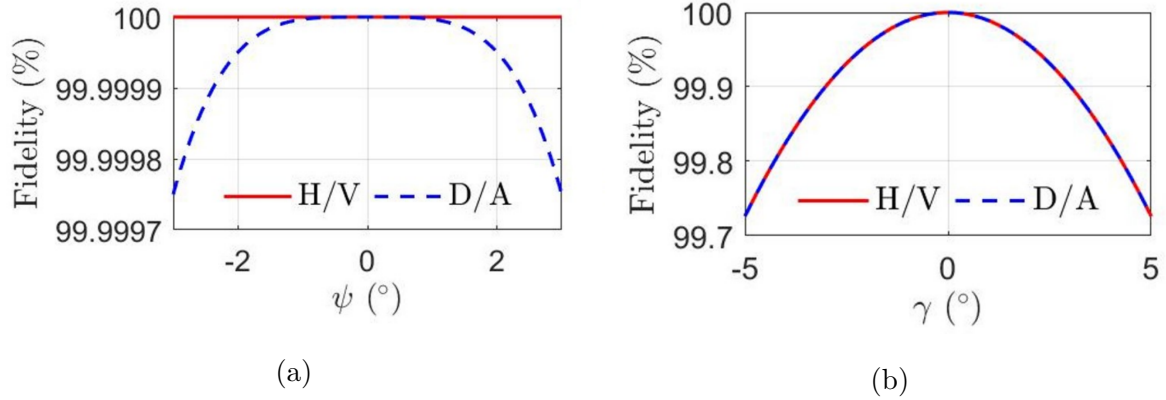
Figure 5.20: Impact of a tilted polarimeter on the fidelity of the measured output states calculated by a theoretical model. [46][45]

desired coordinate. In this work, we picked 2 points on a plane, parallel to the optical table (that the optics were mounted on), and one point on the light propagation axis. First, we mounted two pairs of pinholes on each side of optical table such that, at each side, one pinhole is close to the laser and the other one is at the nearest position to the robot arm. All four pinholes have the same height, so that if the light gets detected by the polarimeter at each side, it indicates that the light is propagating in a plane parallel to the table. To create the user-defined coordinate, we moved the robot arm to observe the beam going through one set of pinholes and recorded the position as Point1 (the origin). Then, we moved it back along the z axis and made sure that the beam is still detectable on the polarimeter, to find Point2. The third point was set by moving the robot arm to the other set of the pinholes and saving the position at where the spot was observed (Fig. 5.19). As a result, the desired coordinate is set and regarding the tilting angles, α and β are adjusted in the process of detecting the beam. Finally, γ is calibrated with the vertical axis of the polarized input light (Fig. 5.18). When the beam is horizontally polarized, the polarimeter γ must be adjusted to record the minimum intensity/power for the vertical state. Hence, the user-defined coordinate is successfully created, and by adding the dimensions of the optic under the test, and other required parameters such as the start/end positions and step size of the scanning, the trajectory can be defined by the user.

Moreover, before measuring the polarization properties of the test-optics, It is essential to be aware of the errors induced by rotation of the polarimeter fixed on the robot arm and systematic errors due to the misalignments or the imperfections of each element. As illustrated in Fig. 5.18, γ rotation can be interpreted as an addition to the azimuth angle

132

of all components, since they all rotate together, $\theta'_{P(Q,H)} = \theta_{P(Q,H)} + \gamma$. Tilting of the waveplates in α and β can be expressed as $\psi = \cos^{-1}(\cos(\alpha)\cos(\beta))$. Then, the phase-retardance of the waveplates can be defined as,

$$\phi(\theta, \psi) = \frac{2\pi}{\lambda} d \left(\sqrt{n_e^2 - \frac{n_e^2 \cos^2(\theta) + n_o^2 \sin^2(\theta)}{n_o^2} \sin^2(\psi)} - \sqrt{n_o^2 - \sin^2(\psi)} \right), \qquad (5.13)$$

Where λ is the incident light wavelength, $n_{o(e)}$ is the ordinary (extraordinary) refractive index and d is the thickness of the waveplate. For simplicity we considered a single-crystal waveplate. We assumed horizontal and diagonal input polarizations, and calculated the fidelity as a function of γ and ψ as shown in Fig. 5.20. As a result we observed that γ rotation degrades fidelity quadratically, whereas ψ rotation impact is negligible. Since the robot arm has rotation error of 1°, the polarization error gets less than 0.2% [45][46].

Finally, to estimate the systematic errors of the waveplates, we performed a conventional calibration of the polarimeter with $|H\rangle$ input state. We measured the optical power at both $|H\rangle$, $|V\rangle$ states as a function of the rotation of the waveplates in 3 configurations:

1. Without the QWP, the HWP was rotated to find its principal axis.

2. The HWP was aligned to the input horizontal polarization and the QWP was rotated 45° with respect to the incident polarization direction.

3. QWP was set at 45° while HWP had a 2π rotation.

From the power measurements, we could correct the instrument matrix we initially had and calibrate the polarimeters. By performing Monte-Carlo simulation, the final uncertainty of fidelity and QBER is determined to be 0.01% and 0.05% respectively. [46]

5.3.3 Honeywell Telescope

Honeywell Aerospace catadioptric telescope was tested for its polarization maintenance with our first generation polarimeter [61]. The telescope has a 26 cm spherical primary mirror with a hyperbolic secondary mirror mounted on a spider and an aspherical singlet lens to widen the field of view up to ±0.3°. In this measurement (both the telescope and the primary mirror) the test optics are place on an optical table inside a blackout enclosure
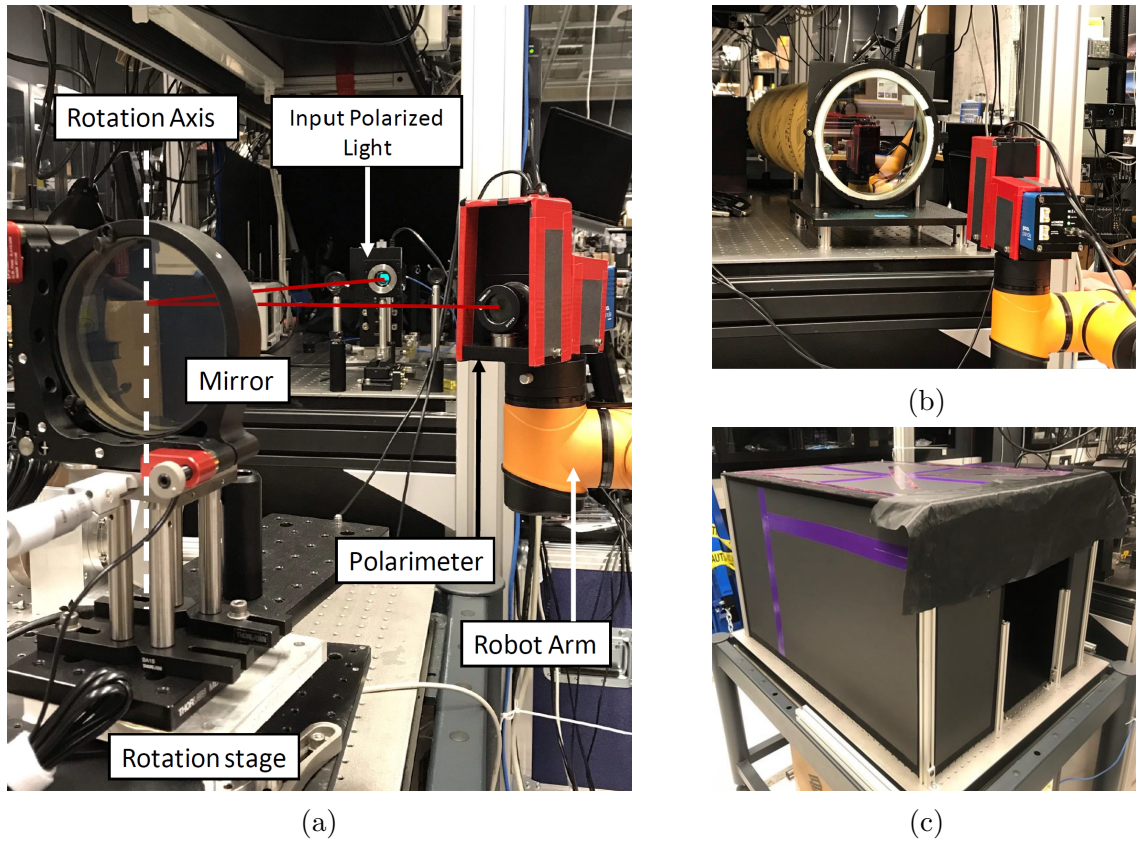
Figure 5.21: (a) Polarization measurement of a protected silver-coated mirror, at different incident angles; (b) Polarization measurement of the custom-designed lens; The tube and the mask are used to block the stray light. (c) Blackout enclosure used for the polarization measurement of the Honeywell optics, to remove the background noise.

to remove the background noise (Fig. 5.21(c)). The enclosure is 61cm×105cm×76cm and it is built with black thick cardboard with black felt paper covering the interior walls to enhance the stray light absorption. The front side has an adjustable opening for the measurements.

In the telescope polarization test, the light source (fibre, polarizer and the rotation stage as discussed above) is fixed in the middle of the primary mirror to send the light to the secondary mirror and to obtain a collimated beam after reflecting from the primary mirror. Two pinholes with the same height are fixed on the table at the two opposite edges of the telescope to check if the output beam is propagating along the optical axis of the mirror, by measuring the power at these two points. The wavefront measurement was also
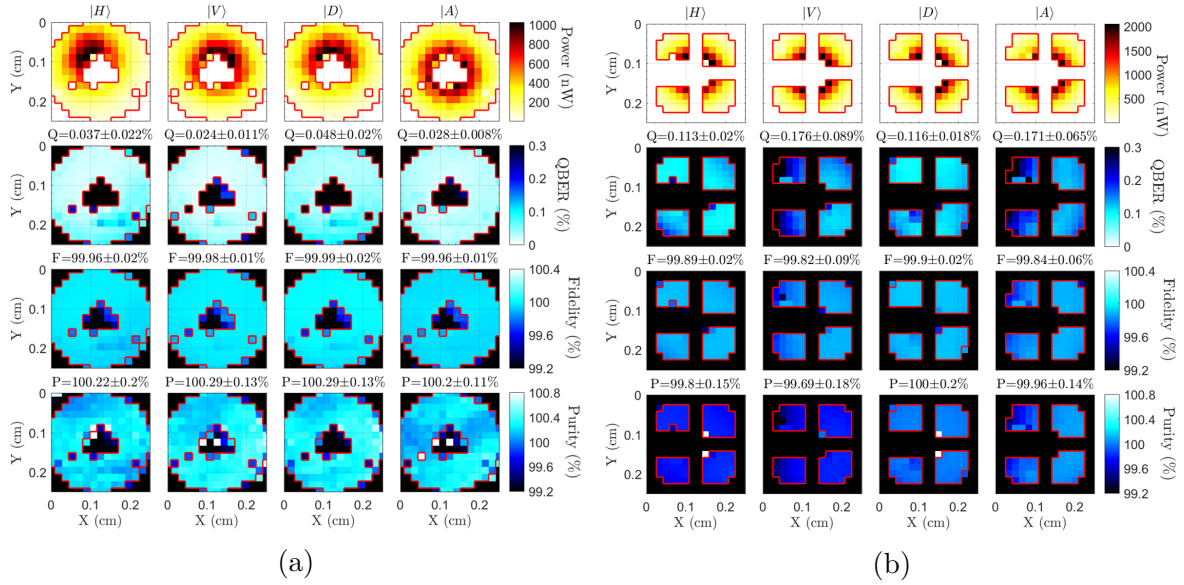
Figure 5.22: (a) Polarization test results of (a) Honeywell prototype telescope and (b) the primary mirror. The colormaps show the measured power, QBER, fidelity and purity of the output beam. The black areas are the parts blocked by the secondary mirror/fibre holder, and the corners of which are not receiving light. The measurement on the primary mirror was performed on four squares across the mirror that to save time by only scanning the areas that are not blocked by the fibre and waveplates.

applied on the beam to check its divergence and to adjust the fibre position to achieve a collimated beam in the output. Then, after characterizing the polarization of the input states, the robot arm moves on an 15×15 grid to measure the output polarization. At each point the polarimeter measures 6 states (H/V, A/D and R/L) and then the robot arm moves to the next position. The entire test repeats 4 times to measure the output states for all 4 polarized input states (H/V and A/D). Scanning is done on a square path, so the corners and the middle part of the mirror which is blocked by the secondary mirror and the spider, do not reflect the beam and appear as black spots in the measurement, so they are ignored in the analysis.

The same test was repeated on the primary mirror, after being removed from the telescope. The fibre fixed inside the rotation stage is placed at the focal point of the mirror. The same calibrations and characterizations were repeated. However, this time we only measured four squares instead of scanning the whole surface (to reduce the measurement time and avoid the parts blocked by the fibre and waveplates at the source.). After col-

lecting the data, Post processing was done to calculate the purity, fidelity and QBER of the measured states.

Fig. 5.22 shows the measurement results. The results for the telescope indicate that it has more than 99.9% fidelity and less than 0.05% QBER on average with a standard deviation of less than 0.03%. The measurements on the primary mirror resulted in an average purity, fidelity and QBER of 99.86±0.09%, 99.86±0.03% and 0.14±0.03% respectively. In the latter test, the results are slightly reduced comparing to the telescope results, which could be due to the background noise in the field of view of the mirror. Overall, our analysis indicates that this method to characterize the polarization maintenance of optics has a high accuracy and confirms the polarization preservation of the Honeywell telescope. However, the long measurement times is a drawback of this approach, which motivated the modification of the polarimeter.

The following measurements are taken with our new polarimeter.

5.3.4 Silver-Coated Folding Mirrors

The two flat silver-coated folding mirrors (48-118-557, Edmund Optics) of the telescope can effect the polarization preservation of the system due to their coating properties and the angle of incident of the beam. Therefore, we measured the reflected polarization states at different incident angles. Since both mirrors have the same coating and substrate, we considered only the 4-inch one as our test-optic and mounted it on a rotation stage (PR50PP, Newport) with ±25 mdeg accuracy to change the reflection angle from 5° to 52.5°. A collimated 4 mm width beam was used as the light source and it was aligned to be incident on the rotation axis of the motor, so that the beam spot on the mirror remains still, during the rotations. Then we defined an arced trajectory centered at the rotation axis of the mirror, so that the robot arm follows the reflected beam at each step. We measured twenty frames at each angle and repeated the test for all four input states (Fig. 5.18(a)).

Fig. 5.23 declares that the H and V states are well aligned to the S and P polarizations of the mirror, since the averaged fidelity and purity are obtained to be greater than 99%. The polarization-dependent reflectivity of the mirror was modeled (black lines in Fig. 5.23) by the multilayered coating calculations [87][45] and compared with the measured results. The average error of fidelity for the D and A states were found to be less than 0.29% and 0.26% respectively. Fig. 5.23 shows a purity of more than 1 which is a result of intensity fluctuations. We used a 4 mm beam and had a 2 mm wide pin hole at the polarimeter, so any instability in the source can cause intensity variation. Unless, we increase the diameter

136
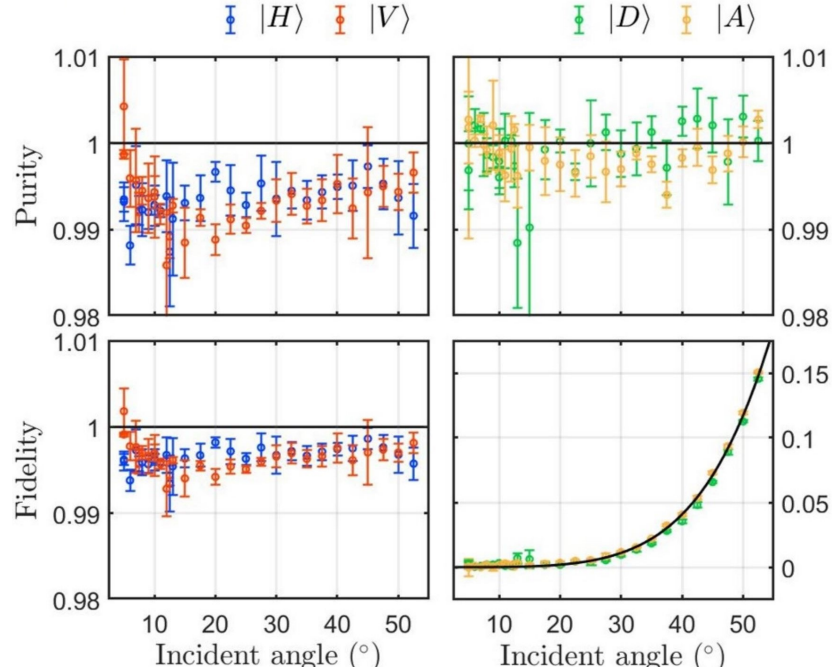
Figure 5.23: Angle-dependent polarization characterization of the silver-coated folding mirror. The solid black line is obtained from the simulation to be compared with the measured values. [45][46]

of the pin hole or use other tomography methods such as a maximal-likelihood estimation method [3].

5.3.5   Custom-Designed 8-inch Lens

In order to perform the polarization characterization on our custom-designed lens, we used a single-mode fibre at the focal position of the lens which was previously measured by the collimation test. We ensured that the transmitted light has a divergence angle of less than ± 10 μrad and is well collimated. As shown in Fig. 5.21(b) we added an 8 inch mask and a tube in front of the lens to crop out the portion of the beam going through the lens as well as blocking the stray light, since the numerical aperture of the fibre was larger than the f-number of the lens. The robot arm then scanned the entire aperture in an even 15×15 grid. The measurement was taken 4 times for each input state. According to Fig. 5.24 it can be claimed that the polarization preservation in terms of fidelity more than 99% and

Input States	Fidelity (%)		Purity (%)		QBER (%)	
	Lens	Telescope	Lens	Telescope	Lens	Telescope
$|H\rangle$	99.19 ± 0.89	99.34 ± 0.63	99.63 ± 0.15	99.67 ± 0.13	0.81 ± 0.88	0.66 ± 0.63
$|V\rangle$	99.25 ± 0.91	99.37 ± 0.69	99.69 ± 0.46	99.71 ± 0.53	0.75 ± 0.91	0.63 ± 0.69
$|D\rangle$	99.15 ± 0.84	99.27 ± 0.62	99.43 ± 0.21	99.45 ± 0.33	0.75 ± 0.84	0.65 ± 0.58
$|A\rangle$	99.15 ± 0.79	99.23 ± 0.68	99.39 ± 0.22	99.56 ± 0.33	0.80 ± 0.80	0.62 ± 0.62

Table 5.6: polarization characterization of the custom-designed lens and the assembled telescope

QBER less than 1% is achieved. Table 5.6 lists the average results of the measured purity, fidelity and QBER of the lens.

In Fig. 5.24 a region on the high-fidelity parts is observed , which changes shape from a "+" at H/V base to a "x" at A/D base. Since the input polarization is prepared by rotating the fibre and the polarizer, this shape could be the result of the imperfection of our source which causes nonuniform input polarization states across the lens aperture. This effect will be investigated in future.

5.3.6 Telescope

The telescope's polarization preservation was measured using the same techniques and assembly as the lens measurements. A single mode fibre was placed at the focal point of the telescope that was determined by the collimation test. The polarimeter moved on a 15×15 grid and measured the transmitted polarization for all four input states. We obtained results of an averaged fidelity and QBER of 99.30±0.65% and 0.64±0.63%, respectively. Table 5.6 summarizes the fidelity, purity and QBER of four measured state of the lens by itself, and after its final assembly into the telescope.

5.4 Conclusion

The star test of the lens, verified its quality comparing to the design in Zemax. The best focused image diameter and the measured focal length agreed with the simulation with less
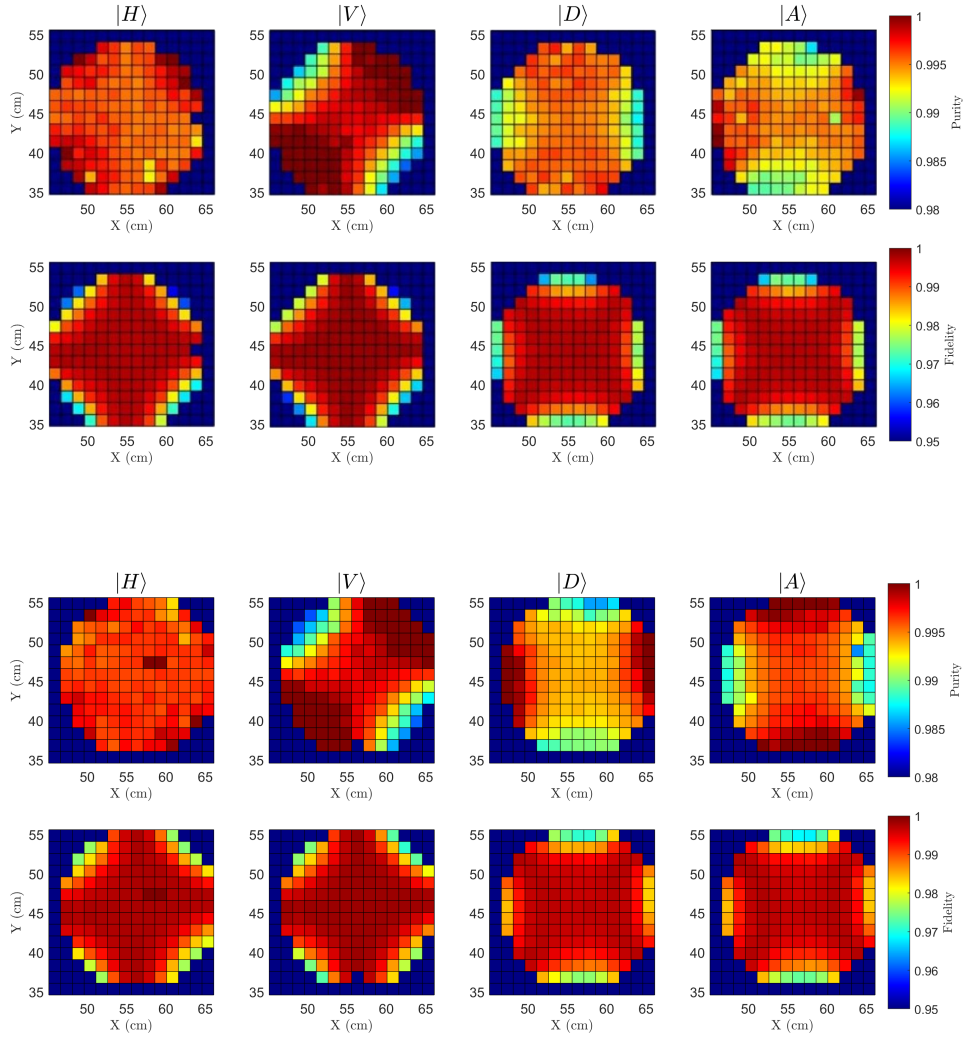
Figure 5.24: Top row: Polarization measurement of the lens. Lower row: Polarization measurement of the telescope. More than 99% fidelity and purity are achieved for both the telescope and the lens. Relatively large error bars and QBER is due to the limited dynamic range of the polarimeter.

than 3.5% error. However, the measurements revealed misalignments in adjusting the lens on the hexapod and aligning all setups together. We repeated the test one more time after assembling the telescope. The lens was fixed on the telescope front lid and the mirrors angles and locations had been determined by the wavefront measurement test. So the new focused image showed a better result with less than 2 μm deviation from the theoretical value. The improvement in the results of tilting effect was noticeable, since the error was reduced by two orders of magnitude. Moreover, the movement of the centroid of the spot in response to 0.13° tilting, was perfectly matched with the Zemax model. Nonetheless, we are looking forward to repeating the star test with real stars that are at infinity relative to the telescope, so that we will be able to do fine alignments and calibrate the telescope.

Furthermore, we presented our home-made wavefront measurement device which was used to determine the focal point of the lens and the assembled telescope, as well as measuring the divergence angle of the beam. As a result, we obtained about $\pm 2.5 \mu$rad divergence angle and an averaged 0.20λ PV wavefront error which is in well agreement with the initial design. However, a 2-dimensional scanning system is required to have a concrete map of the transmitted wavefront. Moreover, by characterizing the system and comparing the results with a 3-dimensional ray-tracing, we could validate our collimation setup as a wavefront measurement tool with high repeatability and accuracy for large optics [47].

Finally, we introduced our polarization measurement setup which uses a polarimeter mounted on a 6-joint robot arm to scan test optics at different dimensions. We presented two generations of polarimeters: Power meter based and camera based. The polarization characterization of a Honeywell designed telescope was performed using the power meter based method inside a blackout enclosure to reduce the background noise. Then we modified the polarimeter by using a camera and a Wollaston prism, which helped with decreasing the measurement time noticeably. In addition, the centroid calculation was effective in enhancing the accuracy of the measurement. The new polarimeter was used to characterize the polarization property of the folding mirrors, the custom-designed lens and telescope. The silver-coated mirrors polarization preservation agreed well with the simulation and the results were promising under 5° to 50° tilting. For the lens and telescope, we achieved more than 99% fidelity and purity for each individually. However, large error bars and QBER were observed in the tests with the new polarimeter, which is due to the limited dynamic range of the camera. In summary, the results confirm that our custom-designed telescope has a very good beam quality accross the desired field of view (0.1 degrees), and also can very well preserve the polarization properties of the transmitted beam which is an asset in polarization-based quantum communication, thus making it suitable as the transmitter in our upcoming free-space experiments.

Chapter 6

Conclusion

In this thesis, a design and build of a transceiver telescope has been presented to be used as the quantum optical ground station for QKD demonstrations as a part of the QEYSSat mission. The telescope is designed and optimized to have minimum link loss and wavefront distortion in an uplink configuration and its aperture was chosen with regard to atmospheric effects and optical properties of the lens. The telescope is also conceived as a refractor system, because the lack of secondary obstruction is very beneficial for an optimal ground to satellite uplink.

In Chapter 2, we studied the impacts of atmosphere on a free space ground-to-satellite channel to estimate the signal loss due to the turbulence and diffraction. By considering the effective aperture diameter in minimizing free space link attenuation and manufacturing costs, we concluded the optimal lens diameter to be 8 inches. In Chapter 3, the design and optimization of the lens was found to achieve the highest performance at our quantum and beacon wavelengths, 780 nm and 980 nm or 1550 nm, respectively. By choosing the correct curvature, thickness and material of the lens, Seidel aberrations were corrected to minimize the wavefront distortion and preserve the polarization, to aid with gaining a higher key rate in free-space QKD experiments. Due to the limitations of optics manufacturers, especially on the surface specifications, we conducted a link analysis to model the atmospheric turbulence and the aberrations of the lens using Zernike polynomials and study the far-field beam to learn about the minimum surface quality required. Hence, an 8-inch doublet lens, corrected for Seidel aberrations at 780 nm, 980 nm and 1550 nm wavelengths, with scratch/dig number of 60/40 and $\lambda/4$ surface irregularity was designed in QPL group and built by Hyperion Optics.

In Chapter 4, we described the design and configuration of mechanical parts of the

telescope assembly. Two motorized folding mirrors were considered in the telescope to help with the alignments and calibrations. The positions of the mirrors were initially verified by the simulation and implemented accordingly in the mechanical parts design. Moreover, the mechanical stability of the structure and impact of temperature gradients was taken into account to minimize any possible stress on the system. However, further research is needed to better understand thermal variation effects. The custom-designed parts were build by University of Waterloo Science Machine Shop and assembled by the QPL group.

After assembling the parts and aligning the optical parts, we performed a star test, a wavefront measurement and a polarization measurement to characterize the telescope, which were discussed in Chapter 5. The star test confirmed having aberration free images within the field of view, for which the measured beam diameters, and focal length were consistent with the Zemax simulation. Next, the wavefront measurement was taken to indicate the divergence angle ($\pm 2.5 \mu m$) and wavefront error (about 0.2λ) of the transmitted beam. Since polarization-based QKD requires high preservation of the polarization states, a polarized beam transmitted through the lens was studied to investigate the fidelity, purity and QBER of the measured states. Achieving averaged state fidelity of 99.30±0.65%, purity of 99.60±0.33% and QBER of 0.64±0.63% meet the requirements for free space quantum communications based on photons polarization.

In near future, we are planning to fix the telescope on the mount inside a dome, to have sky observations and investigate the impact of the gravity on the alignments. Therefore, we are going to repeat the start test with real stars and align the mirrors more precisely to minimize the aberrations induced by the new orientation of the telescope as well as the tilting angle of each mirror. Moreover, studying the starlight received from various elevation angles can inform us of the impacts of the atmosphere and light pollution on the wavefront, which helps to determine the limitations of our ground station. Finally, the telescope needs to be calibrated by multiple stars to reduce the pointing error and facilitate satellite tracking.

In order to gain more insight to the link budget of the quantum signal, we are looking into improving our current link model by considering the imperfections of the detectors on the satellite as well as the fibre coupling efficiencies at both ends. We are eager to expand our analysis to model downlink configuration and achieve an accurate model for the satellite-ground links. Furthermore, thermal characterization of the telescope is required to avoid the extra stress or misalignments caused by temperature gradients during different seasons or different times of a day. Although, some considerations in the mechanical design have already been taken into account to manage the contractions and expansions within -20° to 40°. Using a space blanket, a warmer or a temperature controller to stabilize the

temperature, might be considered in future, to maintain the alignments under extreme temperatures.

Overall, the measured performance of the custom telescope assembly is very impressive, with high beam quality, very good polarization preservation and a good optical throughput. Therefore, this system outperforms any COTS telescopes, and once the initial tracking tests and calibrations are done, the QPL transceiver telescope will be ready to expand the horizons of free space quantum communications by performing QKD experiments in uplink configuration, as soon as the QEYSSat microsatellite is placed in the orbit.
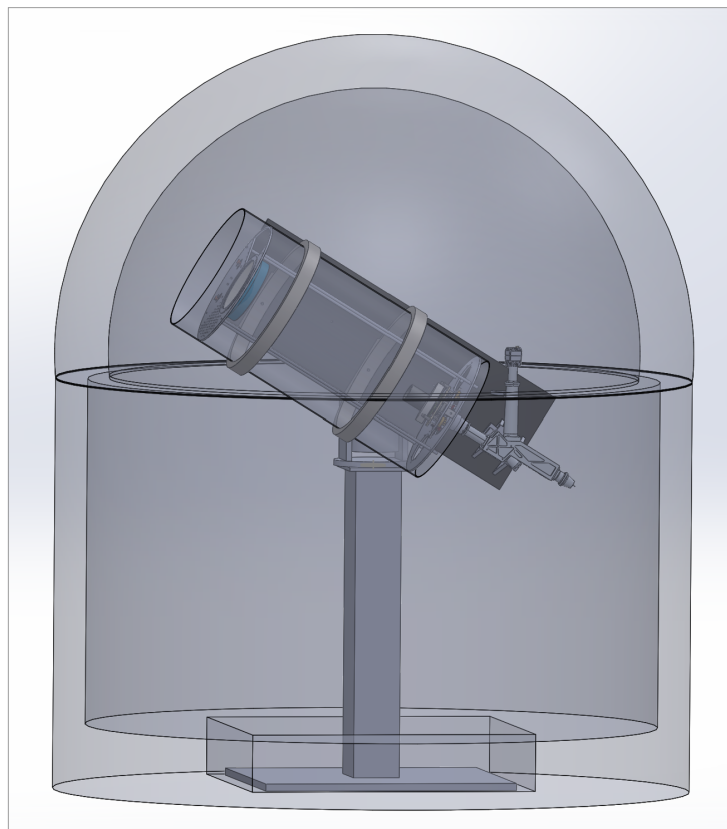
Figure 6.1: CAD model of the telescope mounted on the ASA mount on a pier, placed inside a dome.

References

[1] B. F. Alexander and K. Ng. Elimination of systematic error in subpixel accuracy centroid estimation. *Optical Engineering*, 30, 1991.

[2] Richard Allen, Peng Su, James Burge, Brian Cuerden, and Hubert Martin. Scanning pentaprism test for the gmt 8.4-m off-axis segments. 7739, 2010.

[3] J.B. Altepeter, E.R. Jeffrey, and Paul Kwiat. Photonic state tomography. *Advances In Atomic, Molecular, and Optical Physics*, 2005.

[4] Larry C. Andrews. *Field Guide to Atmospheric Optics*. SPIE., second edition, 2019.

[5] M. Aspelmeyer, Thomas Jennewein, M. Pfennigbauer, Leeb Walter, and A. Zeilinger. Long-distance quantum communication with entangled photons using satellites. *Selected Topics in Quantum Electronics, IEEE Journal of*, 9, 2003.

[6] Charles H. Bennett, François Bessette, Gilles Brassard, Louis Salvail, and John Smolin. Experimental quantum cryptography. *Journal of Cryptology*, 5, 1992.

[7] Charles H. Bennett and Gilles Brassard. Quantum cryptography: Public key distribution and coin tossing. *Theoretical Computer Science*, 2014.

[8] Alberto Boaron, Gianluca Boso, Davide Rusca, Cédric Vulliez, Claire Autebert, Misael Caloz, Matthieu Perrenoud, Gaëtan Gras, Félix Bussières, Ming-Jun Li, D.A. Nolan, Anthony Martin, and Hugo Zbinden. Secure quantum key distribution over 421 km of optical fiber. *Physical Review Letters*, 121, 2018.

[9] J-P Bourgoin, Evan Meyer-Scott, B. Higgins, B. Helou, Chris Erven, Hannes Hübel, B. Kumar, D. Hudson, I. D'Souza, R. Girard, R. Laflamme, and Thomas Jennewein. A comprehensive design and performance analysis of leo satellite quantum communication. *New Journal of Physics*, 15, 11 2012.

[10] Jean-Philippe Bourgoin, Nikolay Gigov, Brendon Higgins, Zhizhong Yan, Evan Meyer-Scott, Amir Khandani, Norbert Lütkenhaus, and Thomas Jennewein. Experimental quantum key distribution with simulated ground-to-satellite photon losses and processing limitations. *Physical Review A*, 92, 2015.

[11] Jean-Philippe Bourgoin, Brendon L. Higgins, Nikolay Gigov, Catherine Holloway, Christopher J. Pugh, Sarah Kaiser, Miles Cranmer, and Thomas Jennewein. Free-space quantum key distribution to a moving receiver. *Opt. Express*, 23(26), 2015.

[12] Jean-Philippe Bourgoin, Brendon L. Higgins, Nikolay Gigov, Catherine Holloway, Christopher J. Pugh, Sarah Kaiser, Miles Cranmer, and Thomas Jennewein. Free-space quantum key distribution to a moving receiver. *Opt. Express*, 23, 2015.

[13] G. Brassard and L. Salvail. *Secret-Key Reconciliation by Public Discussion*. 1993.

[14] Liesl Burger, Igor Litvin, and Andrew Forbes. Simulating atmospheric turbulence using a phase-only spatial light modulator. *South African Journal of Science*, 104, 2008.

[15] A-R. Camboulives, M-T. Velluet, S. Poulenard, L. Saint-Antonin, and V. Michau. Optical ground station optimization for future optical geostationary satellite feeder uplinks. 2017.

[16] Joseph Caniou. *Passive infrared detection, theory and applications - Theory and applications*. SPRINGER SCIENCE+BUSINESS MEDIA, LLC.

[17] L. Carter and M. Wegman. Universal classes of hash functions (extended abstract). 1977.

[18] Poompong Chaiwongkhot, Katanya B. Kuntz, Yanbao Zhang, Anqi Huang, Jean-Philippe Bourgoin, Shihan Sajeed, Norbert Lütkenhaus, Thomas Jennewein, and Vadim Makarov. Eavesdropper's ability to attack a free-space quantum-key-distribution receiver in atmospheric turbulence. *Phys. Rev. A*, 99, 2019.

[19] Jiu-Peng Chen, Chi Zhang, Yang Liu, Cong Jiang, Weijun Zhang, Xiao-Long Hu, Jian-Yu Guan, Zong-Wen Yu, Hai Xu, Jin Lin, and et al. Sending-or-not-sending with independent lasers: Secure twin-field quantum key distribution over 509 km. *Physical Review Letters*, 124, 2020.

[20] Yu-Ao Chen, Qiang Zhang, Teng Chen, Wen-Qi Cai, Liao Shengkai, Jun Zhang, Kai Chen, Juan Yin, Jianyu Wang, Zhu Chen, Sheng-Long Han, Qing Yu, Ken Liang, Fei

Zhou, Xiao Yuan, Mei-Sheng Zhao, Tian-Yin Wang, Xiao Jiang, Liang Zhang, and Jian-Wei Pan. An integrated space-to-ground quantum communication network over 4,600 kilometres. *Nature*, 589, 2021.

[21] D. Dieks. Communication by epr devices. *Physics Letters A*, 92, 1982.

[22] R.M. Neal D.J.C. MacKay. Near shannon limit performance of low density parity check codes. *Electronics Letters*, 33, 1997.

[23] Artur K. Ekert. Quantum cryptography based on bell's theorem. *Phys. Rev. Lett.*, 67, 1991.

[24] V. Fang, J. Kennedy, J. Futter, and J. Manning. A review of near infrared reflectance properties of metal oxide nanostructures. 2013.

[25] Xiao-Tian Fang, Pei Zeng, Hui Liu, Mi Zou, Weijie Wu, Yan-Lin Tang, Ying-Jie Sheng, Yao Xiang, Weijun Zhang, Hao Li, Zhen Wang, Lixing You, Ming-Jun Li, Hao Chen, Yu-Ao Chen, Qiang Zhang, Cheng-Zhi Peng, Xiongfeng Ma, Teng Chen, and Jian-Wei Pan. Implementation of quantum key distribution surpassing the linear rate-transmittance bound. *Nature Photonics*, 14, 2020.

[26] Alejandro Rodrıguez Federico Dios, Juan Antonio Rubio and Adolfo Comeron. Scintillation and beam-wander analysis in an optical ground station–satellite uplink. 2004.

[27] Craig R. Forest, Claude R. Canizares, Daniel R. Neal, Michael McGuirk, and Mark Lee Schattenburg. Metrology of thin transparent optics using Shack-Hartmann wavefront sensing. *Optical Engineering*, 43, 2004.

[28] R. Gallager. Low-density parity-check codes. *IRE Transactions on Information Theory*, 8, 1962.

[29] Ralf Geckeler and Ingolf Weingaertner. Sub-nm topography measurement of large flats: an ultra-precise flatness standard for semiconductor industry. *Proceedings of SPIE - The International Society for Optical Engineering*, 4779, 2002.

[30] D. Gottesman and Hoi-Kwong Lo. Proof of security of quantum key distribution with two-way classical communications. *IEEE Transactions on Information Theory*, 49(2), 2003.

[31] D. Gottesman, Hoi-Kwong Lo, N. Lütkenhaus, and J. Preskill. Security of quantum key distribution with imperfect devices. *Quantum Information and Computation*, 4, 2004.

[32] W. Heisenberg. Über den anschaulichen inhalt der quantentheoretischen kinematik und mechanik. *Zeitschrift für Physik*, 43.

[33] Brendon Higgins, Jean-Philippe Bourgoin, Nikolay Gigov, Evan Meyer-Scott, Zhizhong Yan, and Thomas Jennewein. Detailed performance analysis of the proposed qeyssat quantum receiver satellite. *Conference on Lasers and Electro-Optics 2012*, 2012.

[34] Yin hua Lei, Teng Chen, Z.-W Yu, Hui Liu, L. You, Yi-Heng Zhou, Si-Jing Chen, Ming-Qi Huang, Weijun Zhang, Hao Chen, Ming-Jun Li, D.A. Nolan, Fei Zhou, Xiao Jiang, Zhen Wang, Qiang Zhang, Xiang-Bin Wang, and Jian-Wei Pan. Measurement device independent quantum key distribution over 404 km optical fibre. *Physical Review Letters*, 117, 2016.

[35] Thomas Jennewein, J. Bourgoin, B. Higgins, C. Holloway, Evan Meyer-Scott, Chris Erven, Bettina Heim, Zhizhong Yan, Hannes Hübel, Gregor Weihs, E. Choi, I. D'Souza, D. Hudson, and R. Laflamme. Qeyssat: A mission proposal for a quantum receiver in space. *Proceedings of SPIE - The International Society for Optical Engineering*, 2014.

[36] Thomas Jennewein, J. P. Bourgoin, Brendon L. Higgins, Catherine Holloway, Evan Meyer-Scott, Chris Erven, B. Heim, Zhizhong Yan, Hannes Hübel, Gregor Weihs, Eric Choi, I. D'Souza, Danya Hudson, and Raymond Laflamme. Qeyssat: a mission proposal for a quantum receiver in space. *Advances in Photonics of Quantum Computing, Memory, and Communication VII*, 8997, 2014.

[37] Michael J. Kidger. *Fundamental Optical Design*. SPIE Press.

[38] Craig Kiikka, Daniel R. Neal, John Kincade, Robert Bernier, Tony Hull, David Chaney, Steve Farrer, John Dixson, Avery Causey, and Steve Strohl. The JWST infrared Scanning Shack Hartman System: a new in-process way to measure large mirrors during optical fabrication at Tinsley. In *Space Telescopes and Instrumentation I: Optical, Infrared, and Millimeter*, volume 6265. SPIE, 2006.

[39] Michael A. Krainak, Anthony W. Yu, Guangning Yang, Steven X. Li, and Xiaoli Sun. Photon-counting detectors for space-based laser receivers. 7608, 2010.

[40] Christian Kurtsiefer, Sonja Mayer, Patrick Zarda, and Harald Weinfurter. Stable solid-state source of single photons. *Phys. Rev. Lett.*, 85, 2000.

[41] T. D. Ladd, F. Jelezko, R. Laflamme, Y. Nakamura, C. Monroe, and J. L. O'Brien. Quantum computers. *Nature*, 464, 2010.

[42] Richard J. Sasiela Larry C. Andrews, Ronald L. Phillips and Ronald R. Parenti. Strehl ratio and scintillation theory for uplink gaussian-beam waves: beam wander effects. 2006.

[43] Ronald L. Phillips Larry C. Andrews. *Laser Beam Propagation through Random Media*. SPIE Press, Second Edition.

[44] Andrews L.C. *In Field Guide to Atmospheric Optics*. SPIE Optical Engineering Press, (2004).

[45] Youn S. Lee. *Devices for satellite-assisted quantum networks*. PhD thesis, University Of Waterloo, 2021.

[46] Youn Seok Lee, Kimia Mohammadi, Lindsay Babcock, Brendon Higgins, Hugh Podmore, and Thomas Jennewein. Robotized polarization-characterization platform for free-space quantum communications. 2021. arXiv:2109.01984 [quant-ph].

[47] Youn Seok Lee, Kimia Mohammadi, and Thomas Jennewein. Practical wavefront measurements with scanning pentaprism for optical terminals in free-space quantum communication. 2021. Manuscript in preparation.

[48] Sheng-Kai Liao, Wen-Qi Cai, Wei-Yue Liu, Liang Zhang, Yang Li, Ji-Gang Ren, Juan Yin, Qi Shen, Yuan Cao, Zheng-Ping Li, and et al. Satellite-to-ground quantum key distribution. *Nature*, 549, 2017.

[49] Jennifer L. Marshall, Patrick Williams, Jean-Philippe Rheault, Travis Prochaska, Richard D. Allen, and D. L. DePoy. Characterization of the reflectivity of various black materials. 9147, 2014.

[50] Øystein Marøy, Magne Gudmundsen, Lars Lydersen, and Johannes Skaar. Error estimation, error correction and verification in quantum key distribution. *IET Information Security*, 8, 2014.

[51] Gláucia Murta, Filip Rozpedek, Jérémy Ribeiro, David Elkouss, and Stephanie Wehner. Key rates for quantum key distribution protocols with asymmetric noise. 02 2020.

[52] Daniel R. Neal, Paul Pulaski, Thomas D. Raymond, David A. Neal, Quandou Wang, and Ulf Griesmann. Testing highly aberrated large optics with a Shack-Hartmann wavefront sensor. 5162, 2003.

[53] Igor Nesterenko. The initial approximations for achromatic doublets of the xviii century. 02 2018.

[54] M.A. Nielsen, I.L. Chuang, and I.L. Chuang. *Quantum Computation and Quantum Information*. Cambridge Series on Information and the Natural Sciences. Cambridge University Press, 2000.

[55] Robert J. Noll. Zernike polynomials and atmospheric turbulence∗. *J. Opt. Soc. Am.*, 66, 1976.

[56] A Ling O Lee, T Vergoossen. An updated analysis of satellite quantum-key distribution missions. 2019.

[57] James L. Park. The concept of transition in quantum mechanics. *Foundations of Physics*, 1, 1970.

[58] Cheng-Zhi Peng, Jun Zhang, Dong Yang, Weibo Gao, Huai-Xin Ma, Hao Yin, He-Ping Zeng, Tao Yang, Xiang-Bin Wang, and Jian-Wei Pan. Experimental long-distance decoy-state quantum key distribution based on polarization encoding. *Physical review letters*, 98, 2007.

[59] Xuan Han; Hai-Lin Yong; Ping Xu; Wei-Yang; Wang Kui-Xing Yang; Hua-Jian Xue; Wen-Qi Cai; Ji-Gang Ren; Cheng-Zhi Peng and Jian-Wei Pan. Point-ahead demonstration of a transmitting antenna for satellite quantum communication.

[60] Ben C Platt and Roland Shack. History and principles of shack-hartmann wavefront sensing. *Journal of Refractive Surgery*, 17, 2001.

[61] Hugh Podmore, Ian D'Souza, Danya Hudson, Thomas Jennewin, Jeff Cain, Brendon Higgins, Calvin Midwinter, Alan Scott, Ashley McColgan, Dwight Caldwell, and Sheng Hai Zheng. Optical terminal for canada's quantum encryption and science satellite (qeyssat). 2019.

[62] Christopher J Pugh, Sarah Kaiser, Jean-Philippe Bourgoin, Jeongwan Jin, Nigar Sultana, Sascha Agne, Elena Anisimova, Vadim Makarov, Eric Choi, Brendon L Higgins, and et al. Airborne demonstration of a quantum key distribution receiver payload. *Quantum Science and Technology*, 2, 2017.

[63] Christopher J. Pugh, Sarah Kaiser, Jean-Philippe Bourgoin, Jeongwan Jin, Nigar Sultana, Sascha Agne, Elena Anisimova, Vadim Makarov, Eric Choi, Brendon L. Higgins,

and Thomas Jennewein. Airborne demonstration of a quantum key distribution receiver payload. *2017 European Conference on Lasers and Electro-Optics and European Quantum Electronics Conference*, 2017.

[64] Erhui Qi, Haixiang Hu, and Xiao Luo. Study on low-order aberration measurements of large-aperture flats based on scanning pentaprism technology. *Applied optics*, 58, 2019.

[65] Thomas Raymond, Daniel Neal, Daniel Topa, Wavefront Sciences, and Tony Schmitz. High-speed, non-interferometric nanotopographic characterization of si wafer surfaces. *Proceedings of SPIE - The International Society for Optical Engineering*, 2002.

[66] Holli Riebeek. *Catalog of Earth Satellite Orbits*. www.earthobservatory.nasa.gov, 2009.

[67] Danna Rosenberg, Jim Harrington, Patrick Rice, Philip Hiskett, Charles Peterson, Richard Hughes, Adriana Lita, Sae Nam, and Jane Nordholt. Long-distance decoy-state quantum key distribution in optical fiber. *Physical review letters*, 98, 2007.

[68] Bahaa Saleh and Malvin Teich. *Fundamentals of Photonics, 3rd Edition*. 2019.

[69] David Voelz Santasri Basu and Deva K. Borah. Fade statistics of a ground-to-satellite optical link in the presence of lead-ahead and aperture mismatch. 2009.

[70] Valerio Scarani, Helle Bechmann-Pasquinucci, Nicolas J. Cerf, Miloslav Dušek, Norbert Lütkenhaus, and Momtchil Peev. The security of practical quantum key distribution. *Reviews of Modern Physics*, 81, 2009.

[71] Valerio Scarani, Sofyan Iblisdir, Nicolas Gisin, and Antonio Acín. Quantum cloning. *Rev. Mod. Phys.*, 77, Nov 2005.

[72] C. E. Shannon. Communication theory of secrecy systems. *The Bell System Technical Journal*, 28, 1949.

[73] Vishal Sharma and Subhashish Banerjee. Analysis of atmospheric effects on satellite based quantum communication: A comparative study. *Quantum Information Processing*, 18, 2019.

[74] Banerjee S. Sharma V. Analysis of atmospheric effects on satellite-based quantum communication: a comparative study. 2019.

[75] Shor and Preskill. Simple proof of security of the bb84 quantum key distribution protocol. *Physical review letters*, 2000.

[76] Anthony E. Siegman. *Lasers.* ISBN 0-935702-11-5.

[77] Fritz Bekkadal Simon Plass, Federico Clazzer. Current situation and future innovations in arctic communications. 2015.

[78] Warren J. Smith. *Modern Optical Engineering: The Design of Optical Systems.* SPIE Press, ISBN 0-07-136360-2.

[79] W.H. Southwell. Wave-front estimation from wave-front slope measurements. *J. Opt. Soc. Am.*, 70, 1980.

[80] Larry B. Stotts and Larry C. Andrews. Adaptive optics model characterizing turbulence mitigation for free space optical communications link budgets. *Opt. Express*, 29, 2021.

[81] Peng Su, James H. Burge, Brian Cuerden, Jose Sasian, and Hubert M. Martin. Scanning pentaprism measurements of off-axis aspherics. *Frontiers in Optics 2008/Laser Science XXIV/Plasmonics and Metamaterials/Optical Fabrication and Testing*, 2008.

[82] Harold Richard Suiter. *Star testing astronomical telescopes*, volume Second edition. ISBN 978-0-943396-90-3.

[83] R. Tyson. *Principles of Adaptive Optics, 3rd edition.* CRC Press, 2010.

[84] R. Ursin, F. Tiefenbacher, T. Schmitt-Manderbach, H. Weier, T. Scheidl, M. Lindenthal, B. Blauensteiner, T. Jennewein, J. Perdigues, P. Trojek, B. Oemer, M. Fuerst, M. Meyenburg, J. Rarity, Z. Sodnik, C. Barbieri, H. Weinfurter, and A. Zeilinger. Free-space distribution of entanglement and single photons over 144 km. *Nature Physics*, 2007.

[85] M.P. Varnham, D.N. Payne, R.D. Birch, and E.J. Tarbox. Single-polarisation operation of highly birefringent bow-tie fibres. *Electronics Letters*, 19, 1983.

[86] G. S. Vernam. Cipher printing telegraph systems for secret wire and radio telegraphic communications. *Transactions of the American Institute of Electrical Engineers*, XLV, 1926.

[87] W. Weinstein. Computations in thin film optics. *Vacuum*, 4, 1954.

[88] Robert N. Wilson. 'matching error' (spherical aberration) in the hubble space telescope (hst) - some technical comments. 1990.

[89] W. K. Wootters and W. H. Zurek. A single quantum cannot be cloned. *Nature*, 299, 1982.

[90] www.edmundoptics.com. understanding-optical-specifications.

[91] www.esa.int. Types of orbits.

[92] www.newport.com. optical-surfaces.

[93] James Wyant and Katherine Creath. Basic wavefront aberration theory for optical metrology. *Appl Optics Optical Eng*, 11, 01 1992.

[94] Julius Yellowhair and James H. Burge. Analysis of a scanning pentaprism system for measurements of large flat mirrors. *Appl. Opt.*, 46, 2007.

[95] H. T. Yura. Optimum truncation of a gaussian beam for propagation through atmospheric turbulence. *Appl. Opt.*, 34, May 1995.

APPENDICES

Appendix A

Manufacturing Aspects of Lens Fabrication

In our search for finding the best manufacturer, to fabricate our custom-designed lens, we contacted over 20 in different countries such as Canada, the USA, China, Germany and Italy, to investigate the fabrication process and enhance the performance of our lens. These optical manufacturers are: Hyperion Optics, Shanghai Optics, KreateOptics, Global Precision Optics, INO, BMV Optical Technologies, Knight Optical, Opto Sigma, Argyle Optics, APM telescope, istar Optics, Esco Optics, Asphericon, Lens Optics, Optimax, Tecnottica Consonni, Optical Guidance Systems, Aistana, BRD Optical, Jenoptik, Light Path, Nu-Tek Precision Optical Corporation, Special Optics, Comar Optics, Edmund Optics. The size of the lens and the project timeline were the main factors that narrowed down this list. Lead-times of 7 weeks to 20 weeks were suggested by these manufacturers, and the quoted cost was different, ranging from 14k USD to 73k USD. Hence, It was critical to consider all the available options and prepare the detailed specifications of the lens, before selecting a manufacturer. After we initially designed the lens, the design had changed multiple times based on the manufacturers' recommendations. The many conversations we had with the optical engineers, not only provided invaluable insight into the industrial and manufactural aspects of the project, but also helped us with refining the design and improving the performance of the lens. The following is a summary of the lessons we learnt along the way.

1. All the suggested materials by Zemax were not commercially available. We started with N-FK51A and N-SF66 as our initial materials but we had to change them based on the available glass types by the manufacturers. Also, if the material is a rare find,

it can increase the price, so one can find the replacement for the material by knowing its glass type cross-reference. The suggested materials by the manufacturers are:

- CDGM glass: H-LAF2 and H-ZF5,
- SCHOTT: N-FK5 and SF57,
- CGDM glass: ZF52 and H-QK3L,
- Ohara glass: S-FPL53 and SCHOTT glass: SF2,
- NHG glass: HQF6A and H-FK61B,
- SCHOTT glass: N-KZFS4 and N-PK52A.

2. Some glasses were not available in the required dimensions. For instance,

- N-SF66 was available in strips with 160mm width and 30mm thickness.
- N-FK-51A was available in strips with 100mm width and 40mm thickness.

One solution to fix this problem is melting the glass and reshaping it so that it fits the target dimension. This process is known as "Annealing and Reslumping". However, this process increases the impurities and imperfections such as bubbles and inclusions, in the optical element.

3. Thermal specifications of the glasses must match each other. Also, it is recommended to avoid thermal glasses. our initial materials (N-FK51A and N-SF66) had high thermal sensitivity, so we had to replace them with two materials that are more compatible with each other. Also, N-FK51 is reported to be too thermal, which manufacturers typically avoid, since it can be fragile especially in large diameters.

4. In case, the entire surface of an optic is not used in the experiments, one can reduce the costs by defining a *clear aperture* smaller than the physical diameter of the optic so that the surface is only polished and prepared for the required area.

5. In Optics design it is conventional to report the numbers in mm. Therefore, if the design shows numbers in cm, it is likely to cause a misunderstanding by the manufacturer.

6. Some manufacturers were only able to fabricate air-spaced doublet lenses. The elements of these doublets are fixed inside their lens cells at a particular distance from each other, which makes the system sensitive to any disturbance from the environment. On the other hand, a cemented doublet has higher stability at the cost of

using more glass instead of air, which increases its thickness and weight as well as the price. Since maintaining the alignments of the telescope during experiments is crucial to us, we were only interested in cemented doublets.

7. There was a limit on the focal shift of the three wavelengths, due to the design of our current APT. However, since either 980 nm or 1550 nm (beacon signals) will be used with 785 nm (quantum signal), we did not need a perfect correction for all three wavelengths. As long as, the focal shift of the beacon signal and the quantum signal is less than 10 mm, the APT can be functional. Also, The doublet can only eliminate two spot aberrations effectively, so the focal shift can only be reduced by increasing the refractive index of glass materials. However, high refractive index materials are not typically in large dimensions and if so, they are more expensive and more difficult to process.

8. Surface irregularity can reach $\lambda/10$ to $\lambda/15$ by ion beam polishing, which can increase the costs and the project timeline. However, the manufacturer we selected could get to $\lambda/4$ to $\lambda/5$ with in-house polishing. Hence it is important to determine the minimum required surface specifications before proceeding with the fabrication.

9. To achieve the surface irregularity of $\lambda/4$ and lower, the optical element needs to have a thickness that leaves some room for surface finishing. The thinner the optic is, the harder it gets.

10. Enhancing the surface specifications of our lens from 1λ surface irregularity to $\lambda/4$ and changing the materials for better performance, changed the price from 5k USD to 14k USD. Initially, 50 mm diameter test plates for 3 spherical surfaces were required to achieve 5λ power rings and 1λ irregularity at 633 nm (the wavelength used by the manufacturer), whereas, at least 160mm test plates are needed for in-process accuracy testing to attain 2.5/0.25 (waves) at 633 nm. In addition, one entire set of extra moulded blanks has to be prepared for a potential recovery plan, so that it secures the in-time delivery of one good quality lens.

Finally, we selected Hyperion Optics to fabricate our custom-designed lens. They fabricated the lens according to the specifications provided, within two months. This project had four main phases. The first phase was studying and analyzing the requirements of building a new telescope. Next, the optical and mechanical parts were designed accordingly. In the third phase, the lens had been fabricated by *Hyperion Optics* and the mechanical parts had been constricted by the U*university of Waterloo science machine shop* and anodized by *Waterloo electroplating and metal finishing Incorporation.* After the manufacturing phase,

We had all parts to assemble the telescope and characterize it via various measurements. Since the first day, we started designing the telescope, it took about one year to get all parts constructed and assembled. Despite the COVID-19 pandemic and the global lockdowns that had slowed this project, the telescope was built within a reasonable time and its performance was approved by our group.

Appendix B

Surface Specifications Table

Manufacturing specifications of a Spherical lens at different precision levels, are provided in the table below.

	Commercial	Precision	High Precision
Diameter	$4 - 200$mm	$4 - 200$mm	$4 - 200$mm
Diameter Tolerance	+0/-0.100mm	+0/-0.025mm	+0/-0.010mm
Thickness	±0.100mm	±0.050mm	±0.010mm
Surface Sag	±0.050mm	±0.025mm	±0.010mm
Clear Aperture	80%	90%	90%
Radius	±0.3%	±0.1%	Fix to Test Plate
Power (PV)	3.0λ	1.5λ	$\lambda/2$
Irregularity (PV)	1.0λ	$\lambda/4$	$\lambda/20$
Centering (Beam Deviation)	3 arcmin	1 arcmin	0.5 arcmin
Bevel (Face width at 45 degrees)	<1.0mm	<0.5mm	<0.25mm
Surface Quality	80-50	40-20	10-5

Table B.1: Spherical Lens Manufacturing Specifications [90]

Appendix C

Optics Design Data

The Zemax prescription data of the telescope optics, which includes the custom-designed lens and the two folding mirrors, is provided below. (The surface specifications of the fabricated lens and the commercial mirrors are not considered in the following report.)

```
GENERAL LENS DATA:

Surfaces                   :                    10
Stop                       :                     1
System Aperture            :   Image Space F/# =   12
Fast Semi-Diameters        : On
Field Unpolarized          : On
Convert thin film phase to ray equivalent : On
J/E Conversion Method      : X Axis Reference
Glass Catalogs             :   NHG20190819
Ray Aiming                 : Paraxial Reference, Cache On
X Pupil Shift              :                     0
Y Pupil Shift              :                     0
Z Pupil Shift              :                     0
X Pupil Compress           :                     0
Y Pupil Compress           :                     0
Apodization                :   Uniform, factor =     0.00000E+00
Reference OPD              : Exit Pupil
Paraxial Rays Setting      : Ignore Coordinate Breaks
Method to Compute F/#      : Tracing Rays
```

```
Method to Compute Huygens Integral   : Auto
Print Coordinate Breaks : On
Multi-Threading         : On
OPD Modulo 2 Pi         : Off
Temperature (C)         :      2.00000E+01
Pressure (ATM)          :      1.00000E+00
Adjust Index Data To Environment  : Off
Effective Focal Length  :             2438 (in air at system temperature
                                           and pressure)
Effective Focal Length  :             2438 (in image space)
Back Focal Length       :        873.2123
Total Track             :         876.541
Image Space F/#         :              12
Paraxial Working F/#    :              12
Working F/#             :        12.00038
Image Space NA          :      0.04163054
Object Space NA         :    1.015833e-08
Stop Radius             :        101.5833
Paraxial Image Height   :        4.255117
Paraxial Magnification  :               0
Entrance Pupil Diameter :        203.1667
Entrance Pupil Position :               0
Exit Pupil Diameter     :        203.0869
Exit Pupil Position     :       -2437.212
Field Type              : Angle in degrees
Maximum Radial Field    :             0.1
Primary Wavelength [m]  :           0.785
Angular Magnification   :        1.000393
Lens Units              :    Millimeters
Source Units            :    Watts
Analysis Units          :    Watts/cm^2
Afocal Mode Units       :    milliradians
MTF Units               :    cycles/millimeter
Include Calculated Data in Session File  : On
Include Calculated Data in Session File  : On

Fields          : 3
Field Type              : Angle in degrees
```

```
#       X-Value           Y-Value           Weight
1        0.000000          0.000000          1.000000
2        0.000000         -0.100000          1.000000
3        0.000000          0.100000          1.000000


Vignetting Factors
#       VDX        VDY        VCX        VCY        VAN
1    0.000000   0.000000   0.000000   0.000000   0.000000
2    0.000000   0.000000   0.000000   0.000000   0.000000
3    0.000000   0.000000   0.000000   0.000000   0.000000


Wavelengths    : 1
Units: m
#       Value             Weight
1        0.785000          1.000000


Predicted coordinate ABCD matrix:
A =            2438
B =               0
C =               0
D =            2438


SURFACE DATA SUMMARY:

Surf    Type        Radius      Thickness   Glass    Clear Diam  Conic
 OBJ    STANDARD    Infinity    Infinity             0           0
 STO    STANDARD    1622.225    26          H-LAF2   203.1667    0
   2    STANDARD    -639.67     20          H-ZF5    202.4302    0
   3    STANDARD    Infinity    760                  201.1299    0
   4    COORDBRK    -           0                    -           -
   5    STANDARD    Infinity    -777        MIRROR   143.76      0
   6    COORDBRK    -           0                    -           -
   7    COORDBRK    -           0                    -           -
   8    STANDARD    Infinity    0           MIRROR   78.28       0
   9    COORDBRK    -           847.541              -           -
 IMA    STANDARD    Infinity                         267.5708    0
```

```
SURFACE DATA DETAIL:

Surface OBJ STANDARD

Surface STO STANDARD

Surface   2 STANDARD

Surface   3 STANDARD

Surface   4 COORDBRK
Decenter X               :                0
Decenter Y               :                0
Tilt About X             :                8
Tilt About Y             :                0
Tilt About Z             :                0
Order                    : Decenter then tilt

Surface   5 STANDARD
Mirror Substrate         : Curved, Thickness = 2.87520E+00
Aperture                 : Floating Aperture
Maximum Radius           :            71.88

Surface   6 COORDBRK
Decenter X               :                0
Decenter Y               :                0
Tilt About X             :                8
Tilt About Y             :                0
Tilt About Z             :                0
Order                    : Decenter then tilt

Surface   7 COORDBRK
Decenter X               :                0
Decenter Y               :                0
Tilt About X             :               -8
Tilt About Y             :                0
Tilt About Z             :                0
```

```
Order                      : Decenter then tilt

Surface   8 STANDARD
Mirror Substrate           : Curved, Thickness = 1.56560E+00
Tilt/Decenter              : Decenter X, Decenter Y, Tilt X, Tilt Y, Tilt Z    Order
Before surface             : 0          120        0        0       0 Decenter,Tilt
After surface              : 0          120        0        0       0 Decenter,Tilt
Aperture                   : Floating Aperture
Maximum Radius             :            39.14

Surface   9 COORDBRK
Decenter X                 :                 0
Decenter Y                 :                 0
Tilt About X               :                -8
Tilt About Y               :                 0
Tilt About Z               :                 0
Order                      : Decenter then tilt

Surface IMA STANDARD

EDGE THICKNESS DATA:

Surf         X-Edge            Y-Edge
 STO       14.757912         14.757912
   2       28.058402         28.058402
   3      760.000000        760.000000
   4        0.000000          0.000000
   5     -777.000000       -777.000000
   6        0.000000          0.000000
   7        0.000000          0.000000
   8        0.000000          0.000000
   9      847.541031        847.541031
 IMA        0.000000          0.000000

SOLVE AND VARIABLE DATA:

 Semi Diameter   5      : Fixed
 Parameter  3 Surf   6  : Variable
```

```
 Semi Diameter   8       : Fixed
 Thickness of   9        : Variable


INDEX OF REFRACTION DATA:


System Temperature:   20.0000 Celsius
System Pressure   :    1.0000 Atmospheres
Absolute air index:    1.000270 at wavelength 0.785000 m
Index data is relative to air at the system temperature and pressure.
Wavelengths are measured in air at the system temperature and pressure.


Surf         Glass     Temp     Pres     0.785
  0                    20.00  1.00   1.000
  1      H-LAF2        20.00  1.00   1.706  environmentally improved optical glass
  2      H-ZF5         20.00  1.00   1.723  environmentally improved optical glass
  3                    20.00  1.00   1.000
  4      <CRD BRK>                   1.000
  5      MIRROR        20.00  1.00   1.000
  6      <CRD BRK>                   1.000
  7      <CRD BRK>                   1.000
  8      MIRROR        20.00  1.00   1.000
  9      <CRD BRK>                   1.000
 10                    20.00  1.00   1.000


THERMAL COEFFICIENT OF EXPANSION DATA:


Surf         Glass       TCE * 10E-6
  0                       0.000
  1      H-LAF2           7.300  environmentally improved optical glass
  2      H-ZF5            8.600  environmentally improved optical glass
  3                       0.000
  4      <CRD BRK>        0.000
  5      MIRROR           0.000
  6      <CRD BRK>        0.000
  7      <CRD BRK>        0.000
  8      MIRROR           0.000
  9      <CRD BRK>        0.000
 10                       0.000
```

```
GLOBAL VERTEX COORDINATES, ORIENTATIONS, AND ROTATION/OFFSET MATRICES:
Reference Surface: 5

Surf    R11          R12          R13          X            Tilt X
        R21          R22          R23          Y            Tilt Y
        R31          R32          R33          Z            Tilt Z

  1     1.000    0.000    0.000    0.000E+00   -8.000E+00
        0.000    0.990    0.139   -1.121E+02    0.000E+00
        0.000   -0.139    0.990   -7.981E+02    0.000E+00


  2     1.000    0.000    0.000    0.000E+00   -8.000E+00
        0.000    0.990    0.139   -1.085E+02    0.000E+00
        0.000   -0.139    0.990   -7.724E+02    0.000E+00


  3     1.000    0.000    0.000    0.000E+00   -8.000E+00
        0.000    0.990    0.139   -1.057E+02    0.000E+00
        0.000   -0.139    0.990   -7.526E+02    0.000E+00


  4     1.000    0.000    0.000    0.000E+00    0.000E+00
        0.000    1.000    0.000    0.000E+00    0.000E+00
        0.000    0.000    1.000    0.000E+00    0.000E+00


  5     1.000    0.000    0.000    0.000E+00    0.000E+00
        0.000    1.000    0.000    0.000E+00    0.000E+00
        0.000    0.000    1.000    0.000E+00    0.000E+00


  6     1.000    0.000    0.000    0.000E+00    8.000E+00
        0.000    0.990   -0.139    0.000E+00    0.000E+00
        0.000    0.139    0.990   -7.770E+02    0.000E+00


  7     1.000    0.000    0.000    0.000E+00    0.000E+00
        0.000    1.000    0.000    0.000E+00    0.000E+00
        0.000    0.000    1.000   -7.770E+02    0.000E+00


  8     1.000    0.000    0.000    0.000E+00    0.000E+00
        0.000    1.000    0.000    1.200E+02    0.000E+00
```

```
          0.000     0.000     1.000    -7.770E+02     0.000E+00

  9       1.000     0.000     0.000     0.000E+00    -8.000E+00
          0.000     0.990     0.139     2.400E+02     0.000E+00
          0.000    -0.139     0.990    -7.770E+02     0.000E+00

 10       1.000     0.000     0.000     0.000E+00    -8.000E+00
          0.000     0.990     0.139     3.579E+02     0.000E+00
          0.000    -0.139     0.990     6.229E+01     0.000E+00
```

GLOBAL SURFACE CENTER OF CURVATURE POINTS:
Reference Surface: 5

Surf	X	Y	Z
1	0.0000000000	113.5965650266	808.2815593568
2	0.0000000000	-197.5798825367	-1405.8539139539
3	-	-	-
4	-	-	-
5	-	-	-
6	-	-	-
7	-	-	-
8	-	-	-
9	-	-	-
10	-	-	-

ELEMENT VOLUME DATA:

For centered elements with plane or spherical circular faces, exact
volumes are computed by assuming edges are squared up to the larger
of the front and back radial aperture.

For all other elements, approximate volumes are numerically integrated
to 0.1% accuracy. Zero volume means the volume cannot be accurately computed.

Single elements that are duplicated in the Lens Data Editor
for ray tracing purposes may be listed more than once yielding
incorrect total mass estimates.

```
                              Volume cc    Density g/cc        Mass g
Element surf    1 to 2      660.003702       4.180000    2758.815476
Element surf    2 to 3      773.082789       3.090000    2388.825818
Total Mass:                                              5147.641295


F/# DATA:


F/# calculations consider vignetting factors and ignore surface apertures.


     Wavelength:           0.785000
#             Field       Tan       Sag
1        0.0000 (deg):   12.0004    12.0004
2       -0.1000 (deg):   12.0004    12.0004
3        0.1000 (deg):   12.0003    12.0004


CARDINAL POINTS:


Object space positions are measured with respect to surface 1.
Image space positions are measured with respect to the image surface.
The index in both the object space and image space is considered.


                              Object Space        Image Space
W =  0.785000 (Primary)
Focal Length        :       -2437.999999        2437.999999
Focal Planes        :       -2438.957207          25.671221
Principal Planes    :          -0.957209       -2412.328778
Anti-Principal Planes :     -4876.957206        2463.671220
Nodal Planes        :          -0.957209       -2412.328778
Anti-Nodal Planes   :       -4876.957206        2463.671220
```

Appendix D

Zernike Coefficients of the Lens

Below is the report of the Zernike coefficients of the designed lens at 785 nm.

```
Listing of Zernike Standard Coefficient Data

Note that RMS (to chief) is the RMS of the OPD after subtracting out piston.
The RMS (to centroid) is the RMS after subtracting out both piston and tilt.
The RMS (to centroid) is most physically significant and is generally what
is meant by 'the RMS'. Although OpticStudio uses the term 'centroid' for brevity,
the reference point is not the diffraction intensity centroid, but the reference
point which minimizes the variance of the wavefront.

Using Zernike Standard polynomials.
OPD referenced to chief ray.

Surface                        :      Image
Field                          :      0.0000 (deg)
Wavelength                     :      0.7850 m
Peak to Valley (to chief)      :      0.06638831 waves
Peak to Valley (to centroid)   :      0.06638831 waves

From integration of the rays:
RMS (to chief)                 :      0.01834572 waves
RMS (to centroid)              :      0.01834572 waves
Variance                       :      0.00033657 waves squared
```

```
Strehl Ratio (Est)            :       0.98680082

From integration of the fitted coefficients:
RMS (to chief)                :       0.01829202 waves
RMS (to centroid)             :       0.01829202 waves
Variance                      :       0.00033460 waves squared
Strehl Ratio (Est)            :       0.98687746

RMS fit error                 :       0.00000002 waves
Maximum fit error             :       0.00000010 waves

Z   1      0.04888356 :   1
Z   2      0.00000000 :    4^(1/2) (p) * COS (A)
Z   3      0.00000000 :    4^(1/2) (p) * SIN (A)
Z   4      0.01403258 :    3^(1/2) (2p^2 - 1)
Z   5      0.00000000 :    6^(1/2) (p^2) * SIN (2A)
Z   6      0.00000000 :    6^(1/2) (p^2) * COS (2A)
Z   7      0.00000000 :    8^(1/2) (3p^3 - 2p) * SIN (A)
Z   8      0.00000000 :    8^(1/2) (3p^3 - 2p) * COS (A)
Z   9      0.00000000 :    8^(1/2) (p^3) * SIN (3A)
Z  10      0.00000000 :    8^(1/2) (p^3) * COS (3A)
Z  11     -0.01171764 :    5^(1/2) (6p^4 - 6p^2 + 1)
Z  12      0.00000000 :   10^(1/2) (4p^4 - 3p^2) * COS (2A)
Z  13      0.00000000 :   10^(1/2) (4p^4 - 3p^2) * SIN (2A)
Z  14      0.00000000 :   10^(1/2) (p^4) * COS (4A)
Z  15      0.00000000 :   10^(1/2) (p^4) * SIN (4A)
Z  16      0.00000000 :   12^(1/2) (10p^5 - 12p^3 + 3p) * COS (A)
Z  17      0.00000000 :   12^(1/2) (10p^5 - 12p^3 + 3p) * SIN (A)
Z  18      0.00000000 :   12^(1/2) (5p^5 - 4p^3) * COS (3A)
Z  19      0.00000000 :   12^(1/2) (5p^5 - 4p^3) * SIN (3A)
Z  20      0.00000000 :   12^(1/2) (p^5) * COS (5A)
Z  21      0.00000000 :   12^(1/2) (p^5) * SIN (5A)
Z  22     -0.00061780 :    7^(1/2) (20p^6 - 30p^4 + 12p^2 - 1)
Z  23      0.00000000 :   14^(1/2) (15p^6 - 20p^4 + 6p^2) * SIN (2A)
Z  24      0.00000000 :   14^(1/2) (15p^6 - 20p^4 + 6p^2) * COS (2A)
Z  25      0.00000000 :   14^(1/2) (6p^6 - 5p^4) * SIN (4A)
Z  26      0.00000000 :   14^(1/2) (6p^6 - 5p^4) * COS (4A)
Z  27      0.00000000 :   14^(1/2) (p^6) * SIN (6A)
```

```
Z  28     0.00000000 :    14^(1/2) (p^6) * COS (6A)
Z  29     0.00000000 :    16^(1/2) (35p^7 - 60p^5 + 30p^3 - 4p) * SIN (A)
Z  30     0.00000000 :    16^(1/2) (35p^7 - 60p^5 + 30p^3 - 4p) * COS (A)
Z  31     0.00000000 :    16^(1/2) (21p^7 - 30p^5 + 10p^3) * SIN (3A)
Z  32     0.00000000 :    16^(1/2) (21p^7 - 30p^5 + 10p^3) * COS (3A)
Z  33     0.00000000 :    16^(1/2) (7p^7 - 6p^5) * SIN (5A)
Z  34     0.00000000 :    16^(1/2) (7p^7 - 6p^5) * COS (5A)
Z  35     0.00000000 :    16^(1/2) (p^7) * SIN (7A)
Z  36     0.00000000 :    16^(1/2) (p^7) * COS (7A)
Z  37    -0.00000387 :     9^(1/2) (70p^8 - 140p^6 + 90p^4 - 20p^2 + 1)
```

Appendix E

Publications and Conferences

- Conference:

  1. Kimia Mohammadi, Katanya Kuntz and Thomas Jennewein. Designing A Refractive Telescope For Satellite-Based Quantum Communication. Presented as a talk at the 2021 Photonics North Conference.

- Papers in preparation:

  1. Youn Seok Lee, Kimia Mohammadi, and Thomas Jennewein. Practical wavefront measurement with scanning pentaprism for optical terminals in free-space quantum communication.

  2. Youn Seok Lee, Kimia Mohammadi, Lindsay Babcock, Brendon Higgins, Hugh Podmore,and Thomas Jennewein. Robotized polarization-characterization platform for free-space quantum communications. arXiv:2109.01984